

# REU 2017

*BEIJING*



## Research Experience for Undergraduates

### Section 2

Support for the REU program is provided by the NSF MRSEC program (DMR-1120296) and the REU Site program (DMR-1460428).

## TABLE OF CONTENTS

<b>REU</b>	<b>Faculty Advisor</b>	<b>Page</b>
Etrick, Nicholas	Prof. Margaret Frey	03
Fuentes-Rivera, José	Prof. Tobias Hanrath	12
Hegab, Rachel	Prof. Jonathan Butcher	17
Krumov, Mihail	Prof. Héctor Abruña	27
Lasalde, José	Prof. Alan Zehnder	32
Lopez, Scott	Prof. Tobias Hanrath	43
Ludlow, Brianna Kemper	Prof. Itai Cohen	48
Pacherille, Angela	Prof. Christopher Alabi	52

# Electrospinning and Plasma Treatment of Polyamides for Mosquito-repellant Fabrics

Nicholas R. Etrick<sup>a</sup>, Chunhui Xiang<sup>b</sup>, Margaret W. Frey<sup>c</sup>

<sup>a</sup>Department of Material Science and Engineering, University of Florida, Gainesville, Florida, 32611, United States <sup>b</sup>Department of Apparel, Events, and Hospitality Management, Iowa State University, Ames, Iowa, 50011, United States <sup>c</sup> Department of Human Ecology and Fiber Science and Apparel Design, Cornell University, Ithaca, NY, 14853, United States

**Abstract**—The need for light-weight, high-strength, and easily machineable insect-repellant fabrics is of critical importance to the cessation of viral diseases, such as Zika, malaria, and dengue fever due to climate change. In this study, the viability of electrospinning hierarchically structured nanofiber Nylon-6 fabrics for the purpose of protective garments for workers in the health and environmental safety fields will be investigated and compared to conventional polyamide fabrics, Nylon-6 Tricot and Nylon-66 Knit, using the insecticide Permethrin. Throughout this investigation, the surface coating efficiency will be evaluated to determine the best method of uptake for Permethrin.

**Index Terms**—Permethrin, Nanofibers, Electrospinning, Nylon-6, Polyamide, Insecticide, Zika, Malaria, Protective Garments, Fibers, Fabrics, Plasma, Coating, Mosquito

## I. INTRODUCTION

A striking overlap emerges when regions with extreme climactic conditions in one month are juxtaposed to the geographical distribution of the Zika virus in the subsequent month” [1]. The increasing temperatures across the globe have given rise to the spread of Zika through the *Aedes aegypti* and *Aedes albopictus* mosquitos, since warmer climates give rise to the survival of adult cold-blooded mosquitoes. In fact, higher temperatures give rise to increased feeding rates, breeding, and subsequent replication of viral diseases. Developing countries, beset to poverty and warm, sub-tropical climates, are especially at risk. In fact, researchers estimated that just a 1°C (1.8°F) increase in temperature could lead to an additional 3 million cases of Malaria in children from Ethiopia [2].

Therefore, there is a rapidly developing need for prevention methods in stopping the rise of the number of infectious cases annually. Mosquitoes are commonly believed to be driven to prey by the scent of bacteria on human skin and in sweat. Moreover, insect-repellant sprays remain one of the most common applications of insecticide worldwide. However, the insect repellent efficacy of different repellent products is often misconstrued by manufacturers. The Environmental Working

Group shed some light onto this subject in 2013 and found that various factors claimed from the different insect repellants, such as waterproofing and duration of efficacy, were often far below that of the specified amount, and varying widely even when testing the same active insecticide ingredient and concentration [3]. Therefore, conventional prevention methods for insect repellency are quickly evolving as the need for the prevention and eradication of mosquito-borne diseases are rising exponentially, to prevent fear and the outbreak of a pandemic.

One method for resisting insect are beginning aspects of lightweight insect repellent fabrics that can assist in the prevention in the spread of these infections diseases by the vector mosquito carriers. Currently, there exist numerous commercial products available on the market with the insecticide Permethrin. Permethrin is a broad target synthetic insecticide aimed at inoculating many species of adult insects and larvae. Permethrin is currently the only insecticide allowed by the Environmental Protection agency (EPA) for usage in clothing fabrics due to its low toxicity to humans and negligible effects from leaching onto skin from contact [4]. Various brands, such as L.L. Bean, E.X. Officio, REI, and Insect Shield, offer different variations of Permethrin-treated clothing. However, these articles of clothing are often thick, heavy, expensive, and non-disposable. Therefore, the search for an alternative method of fabricating light-weight, high-strength, disposable, and relatively inexpensive Permethrin-treated fabrics is of utmost importance.

One method of producing lightweight fibers for clothing is known as Electrospinning. Electrospinning is a process in which a charged polymer jet, known as the Taylor Cone, is collected on a grounded collector [5]. Electrospinning uses an applied high voltage to generate an electric field between the tip of the syringe needle and the grounded collector apparatus. A polymeric solution is then pumped through the needle using a syringe pump, allowing a droplet to form at the needle tip. The electrostatic repulsive force applied to the droplet overcomes the surface tension of the solution, while maintaining molecular cohesion, and is able to stream out into two segments: initially a stream and then a whipping cone. Observing the length, thickness, consistency, and movement

of the stream is often useful in predicting the morphology of the nanofibers being formed on the collector plate, where a short and non-uniform stream produces bad fiber alignment and beading [5]. However, these issues can be corrected for by optimizing the parameters of the electrospinning set-up, such as the working distance (distance from the needle tip to the collector plate), the composition of the solute and solvent in the polymer solution, the solution flow rate, collector plate height, and amount of high voltage applied.

A figure of the electrospinning set-up is shown below:

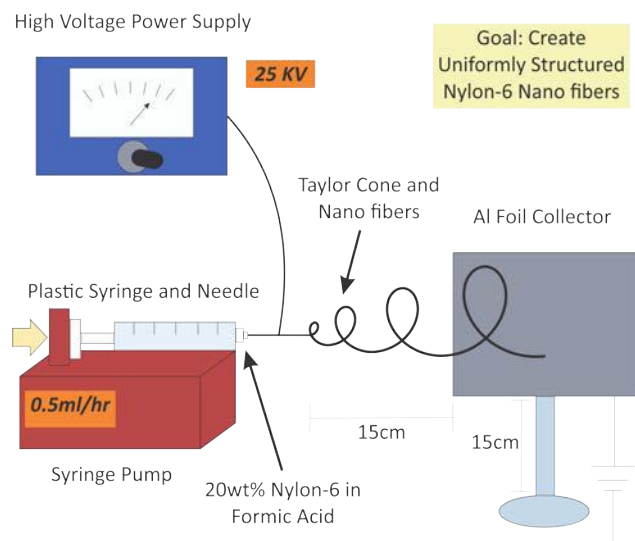


Figure 1: Electrospinning: Set-up

The electrospun fibers that are spun onto the grounded collector have a high surface-to-mass ratio with a large number of pores and a very small pore size. The increased surface area structure of the fibers allows for an increase in allowable absorption area for the incorporation of the Permethrin insecticide, a result necessary for the application. The greater surface area distribution has provided a significant advantage to the electrospun fabrics over typical knit and mesh fabrics that have large pore sizes with less viability for application and incorporation of the insecticide on the surface.

Additionally, using a surface treatment, such as Plasma coating, for the nanofiber fabrics provide an enhancement of desirable properties for textiles, such as increased adhesion of molecules, durability, wettability, bio-compatibility, and adhesion of dyes [6]. Plasma treatment has been shown to have a profound impact over the surface without protruding deeper into the bulk of the fabric material. Plasma is a medium composed of ions, free electrons, photons, neutral atoms, and molecules in the ground and excited states [7]. The Plasma coating process uses an inert gas and accelerates these particles onto the surface of the material where collisions occur causing chemical bonds to break, “activating” the material’s surface. This process introduces a variety of functional groups, depending on the Plasma used, and can act

as sites for polymerization to occur and branch from the surface. Often, the Plasma coating destabilizes the structured bonding on the surface, introducing many different particles that induce coating materials to rapidly bind to the surface and interact with these impingent and delocalized plasma particles.

An area of particular interest in insect-repellent textile fabrication and design is the protection of human beings, animals, and the textile material itself against insect attack [8]. Different coating and impregnation methods have been accessed and tested for applying the insecticide to the material, such as submerging the sample into a solution where the insecticide is the solute, micro-encapsulation, and spraying the insecticide directly onto the surface. Although these techniques have been studied with incorporation in conventional fabrics, the scope of analyzing their effects on electro spun fabrics has yet to be determined. The viability of insect-repellant nano fibers must be evaluated in order to provide an appealing case in replacing conventional knit and mesh fabrics with electrospun nanofibers for more efficient and environmentally safe applications in personal protective equipment (PPE).

## II. MATERIALS AND METHODS

Throughout this investigation, insect-repellant polyamide fabrics were examined and developed using three different coating methods: incorporation into polymer solution during electro spinning, submergence of fabric into an insecticide solution and uniformly coating using a rolling padder, and plasma coating before undergoing submergence into the insecticide solution and rolling through the padder.

### A. Materials

Nylon-6 (MW: 113.6g/mol), formic acid (88%, Macron Fine Chemicals), and Permethrin (CAS #52645-53-1, PESTANAL®), HPLC Grade Methanol ( $\geq 99\%$ , 32.04g/mol) were purchased from Sigma-Aldrich (St. Louis, MO, USA). The Nylon-6 Tricot (Item #: 1410001,  $\sim 73\text{g/m}^2$ ) and Nylon-6,6 (Item #: 1410003  $\text{g/m}^2$ ) were obtained from TestFabrics Inc. (West Pittston, PA, USA).

### B. Electrospinning

Electrospinning solutions without Permethrin contained 20wt% Nylon-6 in 88% formic acid and were placed on a wrist shaker (Burrell Scientific Inc., Pittsburgh, PA, USA) for at least 15 hours prior to electrospinning. Electrospinning solutions with Permethrin included 2.5wt% (by weight of Nylon-6) dissolved in 0.5ml of methanol, stirred for 5 minutes using a Vortex Genie 2 machine (Scientific Industries, NY, USA) A syringe pump (PHS Ultra Syringe Pump, Harvard Apparatus, Holliston, MA, USA) feed rate of 0.5ml/hr, working distance of 15cm, copper wrapped with Al foil collector plate height of 15cm, high voltage, (Gamma High Voltage Research Inc., FL, USA), 22-gauge stainless steel needle, 5ml BD plastic syringe (Becton Dickinson, NJ, USA), target volume of 4ml, and collecting time of 8 hours are parameters used for all samples collected during this single-

needle electrospinning set-up experimentation.

### C. Oxygen Plasma Treatment

The Plasma treated samples consisted of three different polyamide fabrics: N-6 Tricot, N-66 Knit, and N-6 Electrospun. The Plasma treatment method applied was reported by Yip [9] and was used to treat each of the three types of polyamide fabrics. A plasma glow generator was used for dispersion of high energy plasma across the sample surface. Oxygen (O<sub>2</sub>) was chosen as the impinging gas. The discharge power and gas flow rate were 100 W and 50 cm/min respectively, with an exposure time of 10 minutes. Samples were placed in frames designed from Teflon squares (5x10cm on the outside and 4x8cm cut-out on the inside) cut using a laser cutting machine. These frames served to hold the samples in place during plasma coating due to the high energy of the incident plasma beam.

### D. Dip-Coating and Padder Rolling

Insecticide submergence and coating occurred in 55mm Pyrex (Corning Inc., NY, USA) into which the Permethrin was dissolved in a methanol solution in accordance to the ratio 1mg of Permethrin:1ml of methanol solution. For each sample, the following parameters were measured: Fabric weight, 2.5wt% of Permethrin (dissolved in a respective amount of methanol), an aqueous liquor ratio of 1g of fabric:30ml of water, 4wt% Ammonium Sulfate (by wt% of Nylon fabric), and 0.1M Glacial Acetic Acid (NH<sub>4</sub>)<sub>2</sub>SO<sub>4</sub> (Fisher Scientific, NH, USA) until a solution PH of 6. In parallel with the Permethrin-coated samples, blank control treatments without the addition of the 2.5wt% Permethrin insecticide were created using the process mentioned above.

For application of insecticide onto fibers, the required Permethrin was dissolved in the methanol solution using the 1mg:1ml ratio using the Vortex 2 Mixer until no solid Permethrin was visible. Then, all of the other components were added and thoroughly mixed into the solution bottle using the Mixer as well. The fabrics were first soaked in the Permethrin solution for 30 minutes in separate Petri dishes for 30 minutes in the fume hood at room temperature (RT). The fabrics were then taken out of the solution and a uniform rolling was applied using a padder machine (Jeweler Supermarket, USA) until 120wt% of insecticide solution liquid was added to the fabrics in addition to its original weight or given mathematically, 2.2 \* (Weight of Original Fabric). The purpose of padding is to ensure a uniform coating across the entire fiber surface. After rolling through the padder, samples were placed in dry petri dishes in the fume hood at room temperature (RT) for 30 minutes and further for 80°C in a vacuum oven after air-drying. The samples were then packed waterproof and air-tight using aluminum foil and stored in a desiccator under ambient conditions away from UV exposure and protected from the atmosphere.

An image of the padding mechanism used is shown below:



Figure 2: Padder Rolling Machine

### E. Characterization of Fabrics

Each individual Nylon-6 Tricot, Nylon-66 Knit, and Nylon-6 Electrospun fabric was characterized using the characterization methods mentioned below. The Plasma coated, dip coated, single-needle electrospinning incorporated, and control samples were compared for their differences resolved from treatment under each condition.

Each characterization technique will heavily rely on the presence of the cis and trans isomers of chlorine for the determination of Permethrin incorporation into the fibers since the carbon and oxygen bonds are commonalities present throughout both the polyamide and permethrin molecular structures.

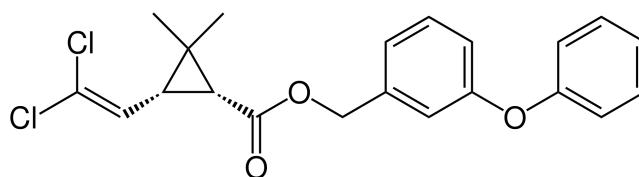


Figure 3: Cis-Permethrin

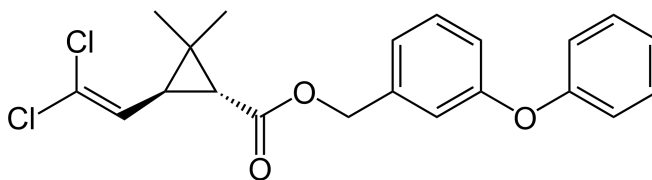


Figure 4: Trans-Permethrin

i. Differential Scanning Calorimetry (DSC)

Polymeric thermograms were obtained for the polyamide fabrics using a TA Q2000 DSC. The operating procedure consisted of a heating sequence at a rate of 10°C/min starting at an equilibrium temperature of -50°C and heating to 300°C before ending the sequence.

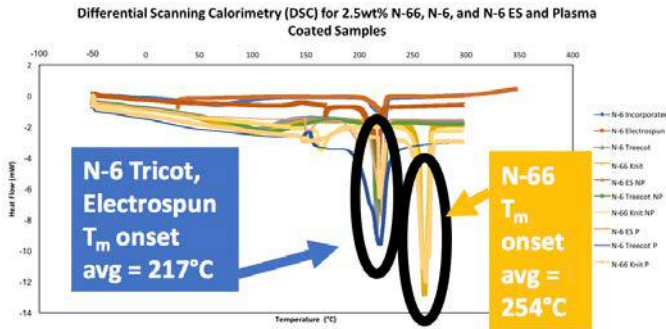


Figure 5: DSC Curves for Plasma, Non-Plasma Treated N-66 Knit, N-6 Tricot, and N-6 Electrospun fabrics

DSC provided an average melting temperature of 217°C in the range of N-6 Tricot and N-6 Electrospun both Plasma and Non-Plasma treated and 254°C for N-66 Tricot Plasma and Non-Plasma treated fabrics. Slight recrystallization was observed for samples that underwent plasma treatment due to double melting peaks.

ii. Thermogravimetric Analysis (TGA)

Thermogravimetric analysis of Plasma and Non-Plasma coated Knit N-66, Tricot N-6, and Electrospun Nylon-6 was performed using a TGA Q500 from TA Instruments. Thermal degradation rates were measured as a function of the steepest slope of polymer degradation that occurred between the points of inflection on the degradation curve. The machine was programed to run from 30° to 600°C at heating rate of 10°C/min with the sample loaded onto a tungsten sample palate.

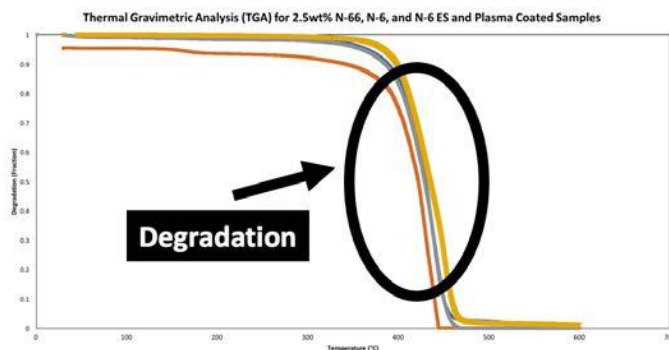


Figure 6: TGA Curves for Plasma, Non-Plasma Treated N-66 Knit, N-6 Tricot, and N-6 Electrospun fabrics

TGA degradation occurred in the highest degree from 400°C to 500°C in all samples. Minimal difference was observed between degradation of plasma and non-plasma treated samples.

iii. Fourier Transform Infrared Spectroscopy (FTIR)

FTIR analysis of Plasma and Non-Plasma coated Knit N-66, Tricot N-6, and Electrospun Nylon-6 was evaluated with a Magna 560, Nicolet Instrument Technologies spectrometer. The percent transmittance was measured as a function of  $\text{cm}^{-1}$  and using the attenuated total reflectance (ATR) mode. The analysis performed was within a range of 4000-600 $\text{cm}^{-1}$  with a resolution of 4 $\text{cm}^{-1}$  and 64 scans for each spectrum. Background scanning was performed three times prior to analysis to provide noise compensation. Additionally, sample stage and probe tip were cleaned with Kim Wipes prior to each run.

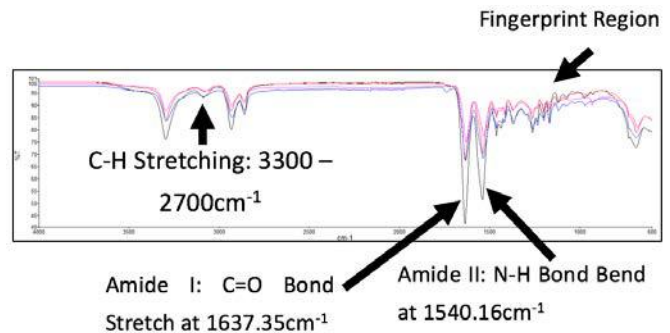


Figure 7: FTIR Curves for Plasma, Non-Plasma Treated N-66 Knit, N-6 Tricot, and N-6 Electrospun fabrics

Bonding characteristic of polyamides, especially Nylon-6 and Nylon-6,6 is evidenced from strong C=O bond stretching at around 1640 $\text{cm}^{-1}$  and N-H bond bending around 1540 $\text{cm}^{-1}$ . These peaks indicate the presence of Nylon fabrics in the sample and a striking similarity between both Nylon-6 and Nylon-6,6. Although the fingerprint regions vary slightly between samples, all curves fit a similar distribution demonstrating how the polyamide characteristics of Nylon-6 and maintained in the electrospun samples.

iv. Field-emission Electron Microscopy (FESEM)

The topographical surface morphology of the Nylon-6,6 Knit and Nylon-6 nanofibers were characterized using the LEO 1550 Keck FESEM. The high-resolution microscopy images provided a clear visibility of the microstructure of the fibers. Fiber samples were sputter coated with gold-palladium for 30s prior to imaging to prevent charging of the sample from the 2kv accelerating voltage electron beam. Both SE2 and InLens detectors were used for probing the sample. The average fiber diameter was calculated for each

sample using the ImageJ software with three different images of each sample and 50 different measurements from each image.

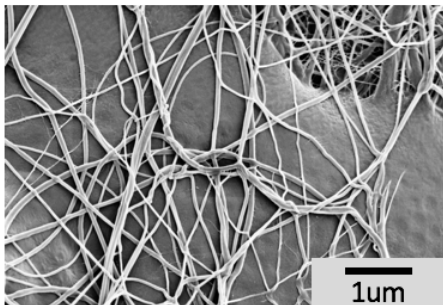


Figure 8: Nylon-6 Electrospun Fibers



Figure 9: Nylon-6,6 Knit Fibers

The average fiber diameter of the electrospun fibers was 0.14μm, whereas the Nylon-6,6 knit was 48μm. In other words, one Nylon-6 electrospun fiber diameter is comparable to 342 Nylon-6,6 fiber diameters. The high porosity and small pore size is evident within the images above and variance in scale bar proportionality. Nylon-6,6 fibers are more linearly distributed and the Nylon-6 nanofibers seem to take on a more randomly intertwined morphology evident from a lack of uniform application on the collector plate during electrospinning.

v. X-Ray Photoelectron Spectroscopy (XPS)

Application of Permethrin to the surface to each of the Polyamide fabrics was tested for the presence of Chlorine using the XPS (Surface Science Instruments, Model SSX100). Al K $\alpha$  x-rays were used as the source for the experiment with a Ni-grating shield present over the samples. Survey, carbon and oxygen, as well as a high-resolution chlorine scans were used throughout experimentation to provide surface-state chemical composition for each sample. The carbon and oxygen scans had a pass energy of 50v, whereas the survey scan was 150v. Each sample was tilted at a 55° take-off-angle (TOA) and precisely aligned with the geometry of the machine. The precise atomic percent (at%) composition of each

element present in the sample was evaluated using a curve-fitting program in CasaXPS (v.2.2.12). Chemical bonding of the N, O, C, and Cl present in the sample was then determined based on the interactions between each of the elements.

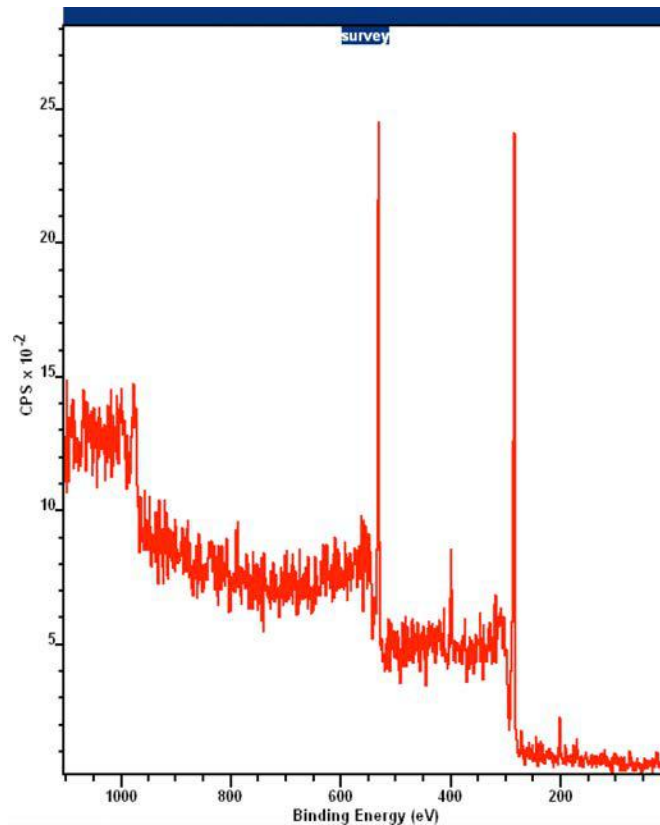


Figure 10: XPS Survey Scan of Plasma N-6 Electrospun

N-66	N-6	ES
4.22	1.96	<u>5.54</u>

Table 1: Atomic Percent of Chlorine on Surface of Sample

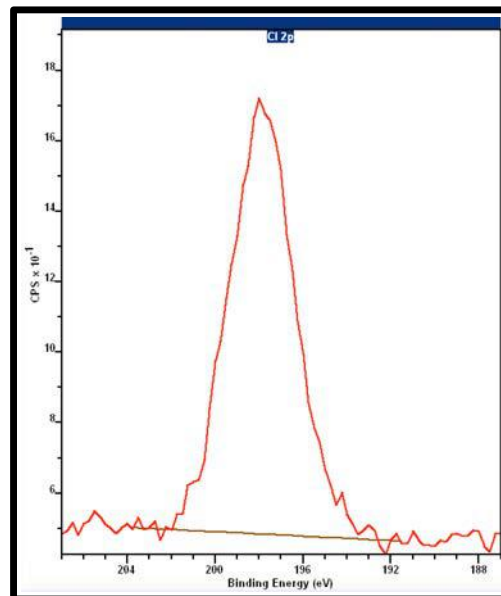


Figure 11: XPS Cl Scan of Plasma N-6 Electrospun

vi. Capillary Flow Porometry

An 1100-AEHXL capillary flow Porometer (Porous Media Inc., Ithaca, NY) was used to inspect the pore sizes of each nylon fabric, as well as the uniformity of the distribution across all pores. A dry-up/wet-up method was selected for analysis with Calwick oil solution having a surface tension of 20.1 dynes/cm (Porous Media Inc., Ithaca, NY) being used as the wetting agent. Initially, the Pressure (Psi) applied to the pores, versus the flow rate (L/min) was obtained. Next, the CAPWIN Porometer software (Ithaca, NY) using the following equation:

$$D = \frac{4\gamma\cos\theta}{p}$$

where D is the diameter of each pore,  $\gamma$  is the surface tension present with Calwick oil solution,  $\theta$  is the contact angle between the oil and the pore surface, and p is the pressure applied.

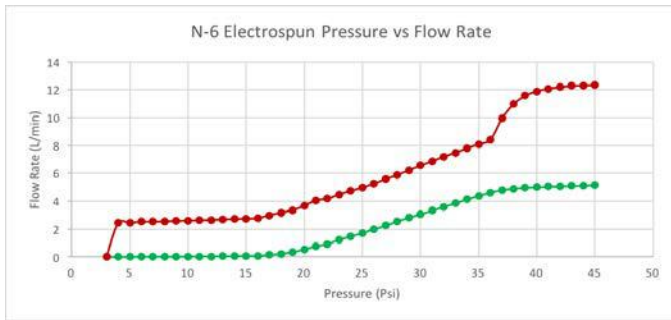


Figure 12: Pressure vs. Flow Rate of N-6 Electrospun

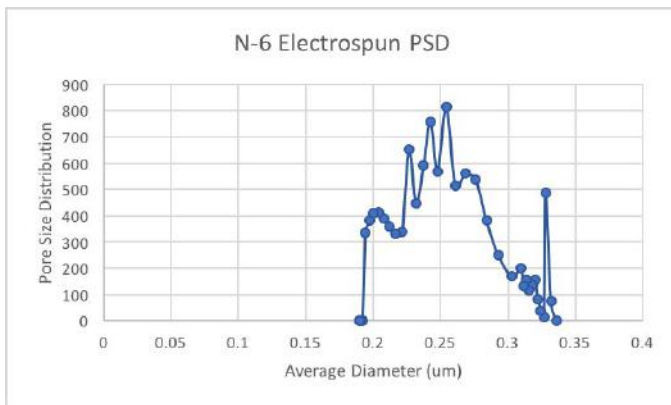


Figure 13: Pore Size Distribution of N-6 Electrospun

F. Tensile Testing

The mechanical properties of the Nylon-6,6 knit, Nylon-6 tricot, and Nylon-6 electrospun fabrics were evaluated using an Instron 5566 (MA, USA) based on ASTM Standard Test Method D638-2014 for Tensile Testing Properties of Plastics. A minimum of five sample sets were collected for each fabric with a constant Dogbone width of 3.18mm, length of 9.53mm, and varying thickness measured using BeadSmith XL-9030 Metric Digital calipers. A 100N load and 10mm/min crosshead pull speed was used during experimentation. Samples were stored in ambient conditions at room temperature in the conditioning room with the machine at least 24 hours prior to testing. BlueHill software was used to calculate the elastic modulus, percent elongation at fracture, and ultimate tensile strength averaged from the five tests for each sample.

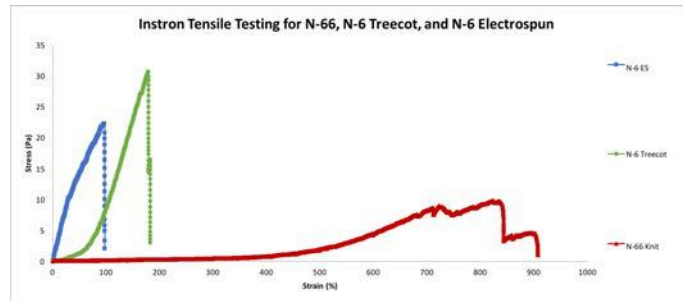


Figure 14: Tensile Tests for Polyamide Fabrics

Sample	Thickness (mm)	Ultimate Tensile Strength (MPa)	Elongation at Failure (%)	Elastic Modulus (MPa)
N-66	0.38	6.12	898.80	1.87
N-6 T	0.15	25.65	252.84	21.03
N-6 ES	0.09	17.40	74.85	32.48

Table 2: Mechanical Properties of Polyamide Fabrics

G. Rheometry

Rheological properties were determined using an AR 2000 Advanced Rheometer (TA Instruments, USA) using an operating temperature of 20°C, an equilibration step duration of two minutes, ramp-up step with a shear rate from 0s<sup>-1</sup> to 90s<sup>-1</sup>, and a ramp-down step with shear rate from 90s<sup>-1</sup> to 0 s<sup>-1</sup>. A 20mm 4° Steel Cone geometry (New Lab # 987409) with a diameter of 20mm, shear rate factor of 14.46, and truncation gap of 108um was used during testing each sample. Twelve 20wt% Nylon-6 in 88% formic acid solutions were tested the morning after sample preparation. Shear rate was plotted against shear stress to determine if flow was Newtonian, shear thinning, or shear thickening. The average viscosity of all twelve measurements was computed and compounded accordingly.

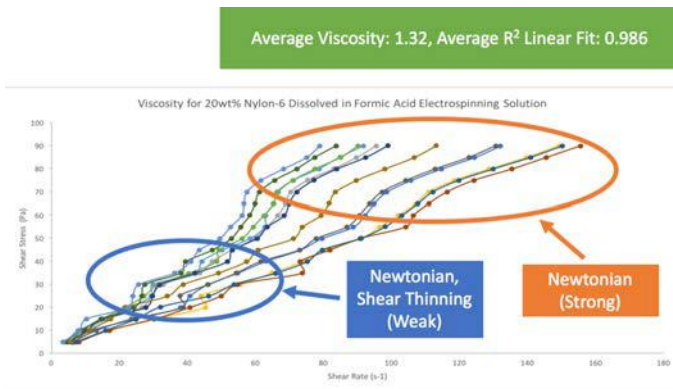


Figure 15: Rheometry of 20wt% Nylon-6 Solutions

*H. Concentration of Permethrin in Fabrics using Gas Chromatography-Mass Spectroscopy (GC-MS)*

GC-MS (Hewlett-Packard GC 6890-Agilent Technologies 5973N MSD) was used to evaluate the content of Permethrin insecticide present in each fabric. The Permethrin fabrics were extracted using a 1g of fabric:30ml of methanol liquor ratio and heated in the oven at 80°C for 30 minutes and placed in amber HPLC vials for analysis. The concentration of each sample was determined after creation of calibration curves for both the cis and trans isomers of Permethrin with a minimum R<sup>2</sup> linear fit value of 0.99.

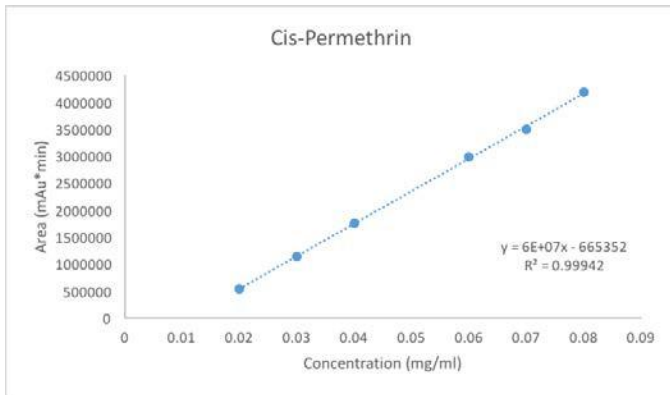


Figure 16: Cis-Permethrin GC-MS Calibration Curve

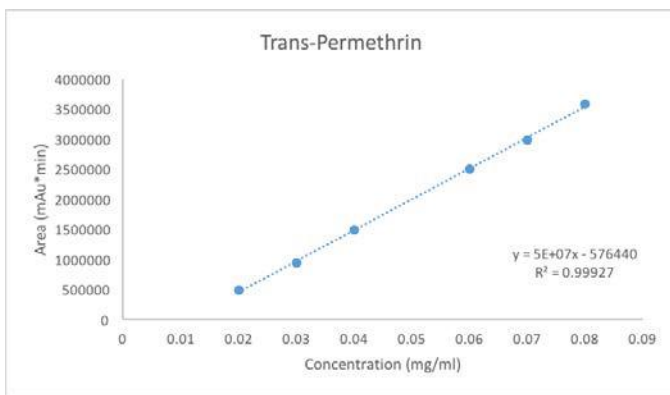


Figure 17: Trans-Permethrin GC-MS Calibration Curve

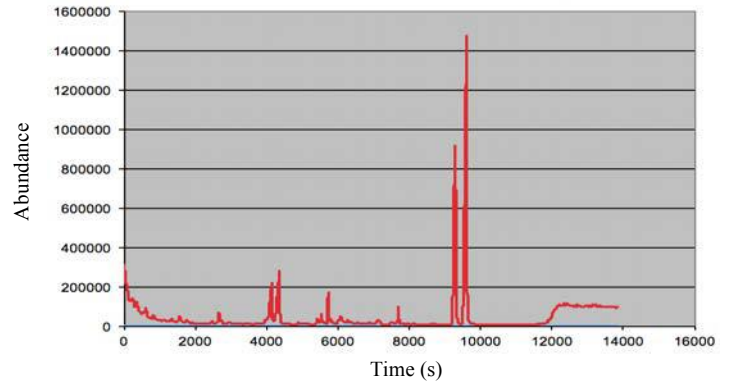


Figure 18: Example GC-MS Curve for Nylon-6 Nanofibers

N-66 Knit Plasma (%o.w.f)	N-6 Tricot Plasma (%o.w.f)	N-6 Plasma Electrospun (%o.w.f)	N-66 Knit Non-Plasma (%o.w.f)	N-6 Tricot Non-Plasma (%o.w.f)	N-6 Non-Plasma Electrospun (%o.w.f)
0.76	0.84	2.36	0.56	2.19	3.36

Table 3: Permethrin Concentrations from GC-MS

*I. UV Degradation*

UV degradation testing was conducted using 1x6cm samples from each testing condition, Nylon-6,6 knit, Nylon-6 tricot, and Nylon-6 electrospun plasma and non-plasma coated. Three 1x6cm strips of each sample was exposed to direct sunlight in a Pyrex petri dish for a duration of four hours. The remaining fiber was dissolved in a 1g:30ml methanol solution and extracted into amber HPLC vials.

N-66 Knit Plasma (%o.w.f)	N-6 Tricot Plasma (%o.w.f)	N-6 Plasma Electrospun (%o.w.f)	N-66 Knit Non-Plasma (%o.w.f)	N-6 Tricot Non-Plasma (%o.w.f)	N-6 Non-Plasma Electrospun (%o.w.f)
0.79	2.16	3.76	0.53	2.54	5.28

Table 4: UV Permethrin Concentrations from GC-MS

*J. Washing Fastness*

The fastness of washing the polyamide fabrics was determined according to DIN EN ISO 105-C10. Five grams of needle soap was used for washing 1g of fabric in 50 ml of soap solution. The textile was washed twice in 5ml of tap water for 10 minutes and twice with 5ml of DIW for 2 minutes. The evaluation of the amount of Permethrin content left after washing treatment was determined using a 1g fabric:30ml methanol extraction with GC-MS.

N-66 Knit Plasma (%o.w.f)	N-6 Tricot Plasma (%o.w.f)	N-6 Plasma Electrospun (%o.w.f)	N-66 Knit Non-Plasma (%o.w.f)	N-6 Tricot Non-Plasma (%o.w.f)	N-6 Non-Plasma Plasma Electrospun (%o.w.f)
0.26	0.85	1.01	0.18	0.31	1.69

Table 5: Washing Permethrin Concentrations from GC-MS

### III. RESULTS AND DISCUSSION

Nylon-6,6 knit, Nylon-6 tricot, and Nylon-6 electrospun fabrics demonstrated a number of similarities and differences based on the differences apparent in their textile fiber structures. All fabrics, regardless of plasma treatment, experienced similar thermal properties with DSC and TGA. The Nylon-6 tricot and Nylon-6 electrospun samples had a  $T_{m\text{onset}}$  around 217°C, whereas the thicker Nylon-6,6 knit structure had a higher melting temperature around 254°C. Additionally, recrystallization was observed for all plasma treated samples and must be further examined for influencing Permethrin uptake. TGA samples all degraded within a range of 400°C – 500°C. However, fabrics will not be exposed to these high temperatures in the proposed application.

Additionally, FTIR evidenced C=O bond stretching at around 1640 $\text{cm}^{-1}$  and N-H bond bending around 1540 $\text{cm}^{-1}$ . These peaks provide a strong indication that polyamides are present in the sample and elicit a confidence in confirming the presence of nanofiber polyamide fabrics as spun from the 20wt% Nylon-6 in 88% formic acid spinning dope.

FESEM compares Nylon-6 nanofibers with an average diameter of 0.14 $\mu\text{m}$  to Nylon-6,6 diameters which are an average of 48 $\mu\text{m}$ , demonstrating how 342 diameters of nanofibers can be fit into a single Nylon-6,6 fiber. These findings are particularly significant because the surface area to weight ratio is crucial for the application of insecticide to the surface of the fabrics. The exponentially larger surface area of nanofiber fabrics provides an advantage to increase the probability of absorption by insecticide solution.

XPS provides atomic-state data on the concentration of chlorine present on the surface of each sample. Notably, the amount of chlorine detected on the surface of the Plasma treated nanofibers was almost triple that detected on Nylon-6 tricot and slightly greater than the Nylon-6,6 knit, which is thicker. Additionally, the difference between non-plasma and plasma treated samples is significant. During survey scanning, the chlorine 2p peak was not visible without enhancing the resolution to an erroneous degree by cancelling out most noise from the sample. However, once plasma treatment was applied to the samples, the Cl 2p peak visibility was enhanced. This result indicates the effect of plasma treatment on the samples assisting attachment of Permethrin molecules to the surface of the polyamide samples.

Capillary flow porometry provided the average pore size and pore size distribution for each polyamide sample. Nylon-6

tricot had the largest average pore size of 143.18 $\mu\text{m}$ , followed by Nylon-6,6 with 27.62 $\mu\text{m}$ , and finally Nylon-6 electrospun at 0.23 $\mu\text{m}$ . The porometry data establishes that the average pore size of the electrospun Nylon-6 is about 620% less than that of Nylon-6 tricot. The significantly small pore size, narrow pore distribution, and high surface area evident from both the FESEM and porometry data further solidify the enhanced ability of nanofibers to withdraw Permethrin from the insecticide solution to coat a larger surface area of fibers.

Mechanical testing data from the Instron tensile samples indicate that N-66 Knit has a high strain rate, especially due to its knit textile feature which providing loading onto different fibers, enabling a high stretch ability. Nylon-6 nanofibers has about 2/3<sup>rd</sup> the strength of Nylon-6 tricot fibers, with about 2/3<sup>rd</sup> the weight and thickness. Likewise, although the nanofibers have about half of the strain of Nylon-6 tricot fibers, the processing of electrospun fibers was not done to the precise uniformity of manufacturing tricot fibers. Therefore, these properties point to the indication that nanofibers are comparable in strength to Nylon-6 tricot fibers and should be studied with reinforcement mechanisms in future cases.

Rheometry provided the indication that the 20wt% polymeric solution was a good fit for Newtonian behavior. The  $R^2$  linear fit was 0.986, with a uniformly high linear correlation at high shear and strain rates. However, the viscosity of the solution is relatively low and, although a linear fit is to be expected, variability from atmospheric and processing conditions could alter the polymers properties.

Finally, GC-MS data for concentration, UV, and washing was compared against one another. A trend commonly established across all data sets was that Nylon-6 nanofiber fabrics contained the highest percentage of Permethrin per weight of fabric for all conditions tested. Plasma coating did increase incorporation for preliminary samples, however, UV testing provided inconclusive results. Incorporated electrospinning of Permethrin into the solution nanofibers produced a high concentration of Permethrin relative to other fabrics, potentially due to the lack of uniformity and dispersion throughout the polymer solution. The idea is that Permethrin is not evenly coated across the surface. The issues posed by uneven coatings must be addressed for adequate mosquito efficacy trials. However, GC-MS results for washing fastness testing were much more conclusive. On average, the nanofiber plasma treated fabrics only lost 39% of Permethrin, whereas the N-6 tricot lost 63% and the N-66 knit lost 76% of Permethrin to washing using the procedure outlined in DIN EN ISO 105-C10. Evidently, the smaller pore sizes of the nanofibers provide an advantage in this regard since Permethrin coating can penetrate deep between small pores and resist loss from washing using soap and water. In this regard, nanofibers provide a high absorbency of incident solution, if submerged for a relatively long duration of time, and resist pushing the solution out from small pores.

#### IV. CONCLUSION

Nanofiber fabrics provide numerous advantages over conventional fabrics, such as lightweight, high porosity, small pore size, high specific strength, and ease of manufacturability. Nylon-6 electrospun fibers provide an intuitive solution to a gamut of problems with conventional fabrics that can be alleviated from the benefits mentioned above. The ability to coat the nanofibers with insecticide solutions was clearly evident throughout the paper, providing superior surface adhesion properties to that of conventional Nylon-6 tricot and Nylon-6 knit fabrics. Further consideration into the optimization of electrospinning parameters, plasma treatment, and scaling up manufacturability of nanofibers is necessary to ensure the delivery of insect-repellant nanofibers fabrics into the industry in the near future.

#### V. FUTURE STUDIES

Insect efficacy testing will be an essential next step in the process to compare the ability of the nanofiber fabrics to repel mosquitoes in a spatial repellency tunnel compared to traditional Nylon-6,6 knit and Nylon-6 tricot fabrics. Also, different polymer solutions for electrospinning should be used, notably cotton cellulose and polyester, as these polymers are commonly available in clothing used in industry. Large-scale manufacturing, flame retardancy, and comfort testing are future studies essential to the implementation into the commercial stratosphere. Finally, it is necessary to understand the effect of manipulating the fiber structures to enhance desirable properties, such as through the use of composite materials or additive strengthening mechanisms.

#### VI. AUTHOR INFORMATION

##### Corresponding Authors

- N. Etrick, Email: [etrick.nicholas@gmail.com](mailto:etrick.nicholas@gmail.com)
- C. Xiang, Email: [chxiang@iastate.edu](mailto:chxiang@iastate.edu)
- M. W. Frey, Email: [margaret.frey@cornell.edu](mailto:margaret.frey@cornell.edu)

#### VII. ACKNOWLEDGEMENTS

I would like to acknowledge to following individuals for providing a valuable contribution to the success of this summer research experience at Cornell University: Dr. Margaret Frey, Dr. Chunhui Xiang, Xia (Sam) Zeng, Debbie Nyakaru, Dr. Darren Dale, Dr. Mick Thomas, Rebecca Broome, Dr. Juan Hinestroza Minji Kim, Jisoo Kang, Alex Martell, Dr. Min Xiao, Catherine Reyes, Randi Rainbow.

I would also like to thank the Cornell Center for Materials Research Facilities (CCMR) for providing me with the appropriate facilities to perform necessary characterization techniques, the NSF MRSEC Program ((DMR-1120296) for providing funding to this project, and the Cornell Department of Human Ecology and Fiber Science and Apparel design for hosting me in the laboratories throughout the duration of my stay in Ithaca, NY.

#### REFERENCES

- [1] Butler, K. (2017). *The truth about bug spray*. [online] Mother Jones. Available at: <http://www.motherjones.com/environment/2014/05/truth-about-insect-repellent-deet/> [Accessed 9 Aug. 2017].
- [2] Chen, S., Chen, S., Jiang, S., Xiong, M., Luo, J., Tang, J. and Ge, Z. (2011). Environmentally Friendly Antibacterial Cotton Textiles Finished with Siloxane Sulfopropylbetaine. *ACS Applied Materials & Interfaces*, 3(4), pp.1154-1162.
- [3] Consumer Reports. (2017). *Can Permethrin Treated Clothing Help You Avoid Mosquito Bites?*. [online] Available at: <https://www.consumerreports.org/insect-repellents/permethrin-treated-clothing-mosquito-bites/> [Accessed 9 Aug. 2017].
- [4] Leach, M., Feng, Z., Tuck, S. and Corey, J. (2017). *Electrospinning Fundamentals: Optimizing Solution and Apparatus Parameters*.
- [5] Pappas, D., Bujanda, A., Demaree, J., Hirvonen, J., Kosik, W., Jensen, R. and McKnight, S. (2006). Surface modification of polyamide fibers and films using atmospheric plasmas. *Surface and Coatings Technology*, 201(7), pp.4384-4388.
- [6] Paz, S. and Semenza, J. (2017). *El Niño and climate change—contributing factors in the dispersal of Zika virus in the Americas?*.
- [7] Singer, M. (2016). *Anthropology of infectious disease*. London: Routledge.
- [8] Faulde, M.K., W.M. Uedelhoven, and R.G. Robbins, *Contact Toxicity and Residual Activity of Different Permethrin-Based Fabric Impregnation Methods for Aedes aegypti (Diptera: Culicidae), Ixodes ricinus (Acari: Ixodidae), and Lepisma saccharina (Thysanura: Lepismatidae)*. *Journal of Medical Entomology*, 2003. **40**(6): p. 935-941.
- [9] Yip, J., et al., *Low temperature plasma-treated nylon fabrics*. *Journal of Materials Processing Technology*, 2002. **123**(1): p. 5-12.

# Controlling Product Selectivity for Electrochemical Reduction of CO<sub>2</sub> on Au by Pulsing Potentials

José J. Fuentes-Rivera, \*\* Kevin Kimura, \* and Tobias Hanrath \*

\* Department of Chemical Engineering, Cornell University

\*\* Department of Chemistry, University of Puerto Rico-Río Piedras Campus

## ABSTRACT:

The electrochemical reduction reaction of CO<sub>2</sub> has been widely studied because it has significant applications regarding the environment by reusing the CO<sub>2</sub> being wasted by industries. Nonetheless, there is still a lack of a convenient and effective procedure for making this process viable, perhaps because of the not yet well understood mechanism. Also, this reaction usually has low efficiencies due to its competition with the hydrogen evolution reaction. For this reason, novel ways of raising the efficiency of the reaction and controlling the selectivity of products are needed. In this work, we present a relatively simple and convenient way of having control over the selectivity of the CO<sub>2</sub> reduction reaction by using pulses and alternating between two potentials. The ratio % of CO and H<sub>2</sub> were measured and used to compare the results between not pulsing and the different anodic potentials used while sticking to the same cathodic potential. The best results were observed when using an anodic potential of -200 mV and cathodic potential of -1650 mV vs. Ag/Ag/Cl, having a ~70 % CO and ~30% H<sub>2</sub> ratio percentages.

## I. INTRODUCTION

It is widely known that the use of fossil fuels has been contributing to the global warming because tons of carbon dioxide (CO<sub>2</sub>) are released into the atmosphere and as of July

2017, the CO<sub>2</sub> levels in the atmosphere has reached over 407 ppm.<sup>1</sup> Also, it is known that CO<sub>2</sub> is a greenhouse gas, acting as a temperature balancer and keeping the heat inside the stratosphere by absorbing and emitting radiation from the Sun, especially in the infrared range of the electromagnetic spectra.<sup>2</sup> When the CO<sub>2</sub> levels are too high, more radiation is absorbed and the balance of heat is perturbed, often resulting in a raise of temperature that causes the global warming. Hence, a lot of efforts are being put into alternatives ways of lowering the amount of CO<sub>2</sub> that is being thrown to the atmosphere. An alternative way of doing this, is the conversion of carbon dioxide to methane (CH<sub>4</sub>), carbon monoxide (CO), methanol (CH<sub>3</sub>OH), ethanol (CH<sub>3</sub>CH<sub>2</sub>OH), among other products, using electrochemical a reduction reaction. This idea has been widely studied because the resulting products can be reused as a fuel or as synthetic precursors in the polymer industry. Also, some attractive reasons to study this type of technique are that the source of electricity can be provided at low cost by making use of different renewable energies and the reaction can be done under normal conditions in water. However, this process usually has low yields because results in a mixture of products, making it not as efficient as desired. Another issue with the CO<sub>2</sub> reduction reaction (CO<sub>2</sub>RR) is that the common potentials used to perform them also compete with the hydrogen evolution reaction (HER), decreasing the general efficiency of the

process by producing H<sub>2</sub>. Hence, the development of new technologies and techniques to make the CO<sub>2</sub>RR more cost-effective is needed. It is known that different facets of a metal catalyst can in fact enhance the selectivity of products in CO<sub>2</sub>RR. Hence, some approaches include using different facets of several metal catalysts, modified nanoparticles, nanorods, among other approaches to enhance efficiency and selectivity of CO<sub>2</sub>RR.<sup>3,4</sup> Yet, none of them have had a significant impact in the field, perhaps because of lack of available technology to engineer a whole process of mass production. In this work, a simple technique of pulsing potentials on a gold (Au) surface as catalyst in a water solution is used for making the CO<sub>2</sub>RR more selective towards CO by suppression of HER.

## II. EXPERIMENTAL SECTION

**Materials.** A three-electrode system was used for all the experiments done, with a silver/silver chloride in a potassium chloride solution as the reference electrode (Ag/AgCl KCl 3.5 M), a Platinum (Pt) coil as the counter electrode, and a Au *Pine Research* rotating disk electrode (RDE). Just to clarify, the Au RDE was used as a regular electrode by attaching it to a rubber stopper with a Ti wire to make the connection with the potentiostat, and not as it is usually used to perform RDE experiments. A biologic SP300 potentiostat was used with EC-Lab software to perform the electrochemical measurements. Also, the compensation feature of the software was used at 85% of the value of  $R_u$  and the last 15% was post-corrected to have a better and accurate potentials when changing the potentials to the reversible hydrogen electrode scale (RHE). From here on, all the potentials reported in this work will be vs. Ag/AgCl, unless states otherwise. A 0.1 M solution of potassium bicarbonate (KHCO<sub>3</sub>) was used as a medium

with pH = 6.8 because it has been previously reported that KHCO<sub>3</sub> plays an important role in the CO<sub>2</sub>RR by being at equilibrium with the CO<sub>2</sub> dissolved in water, helping enhance the effective concentration of CO<sub>2</sub> at the electrode's surface.<sup>5</sup> The electrochemical cell used had two compartments divided by an anionic exchange membrane to separate the Pt counter electrode from the other two electrodes. All the solutions were saturated with CO<sub>2</sub> by bubbling for at least 15 min prior to the experiment and CO<sub>2</sub> was also being supplied into the solution during the

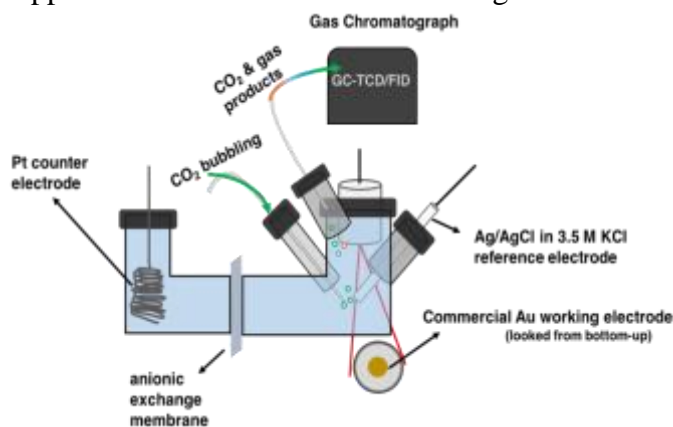


**Figure 1:** Experimental set-up scheme. The green circles represent CO<sub>2</sub> bubbles introduced in the system, the blue and orange circles represent H<sub>2</sub> and CO, respectively, being formed near the Au electrode area.

experiment at a flow rate of ~10 psi. The electrochemistry was performed during 2 h and the gas products were analyzed each half an hour using gas chromatography (GC, SRI Instruments Multiple Gas Analyzer #5) coupled with a thermal conductivity detector (TCD) and a flame ionization detector (FID). A scheme of the experimental set-up can be found in **Figure 1**.

## III. RESULTS AND DISCUSSION

The main goal of this work was to compare the product ratio between H<sub>2</sub> and CO of applying a constant reduction potential vs

applying pulses of potentials while alternating between a reduction potential ( $V_c$ ) and an oxidation potential ( $V_a$ ). Moreover, the effect of the period in which these two potentials were applied was studied along with the effect of having a different  $V_a$ . To ensure that the system has enough driving force for the reaction to take place, a  $V_c$  of -1650 mV ( $\sim -1.0$  V vs RHE) was chosen and was kept constant through all the experiments.

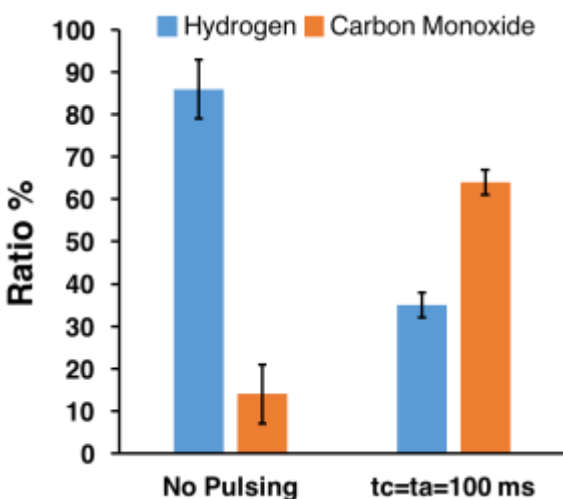


**Figure 2:** Comparison of ratio % of  $H_2$  and CO when using constant potential and using pulses of potentials.  $V_c = -1650$  mV &  $V_a = 0$  mV with symmetric pulses of 100 ms.

The time periods chosen for both the cathodic ( $t_c$ ) and anodic ( $t_a$ ) pulse were 100 ms (**Figure 2**). When using a  $V_a = 0$  mV and comparing the ratio of  $H_2$  and CO with a constant potential, an increase of CO can be observed and the  $H_2$  decreases. This is an interesting result to look at, because somehow, the pulsing is causing the system to be more selective towards the formation of CO at the same time is suppressing the HER. A couple hypotheses can arrive from this phenomenon; the abrupt exchange between the potentials used is somehow causing deformations of the metal facets creating selective interactions between  $CO_2$  and the Au surface or the oscillation between one potential (-1650 mV) and another potential slightly more positive

(0 mV) is inducing an electrostatic repelling effect on  $H^+$ , allowing the CO formed to adsorb at the surface and occupy most of the active sites (**Figure 3**).

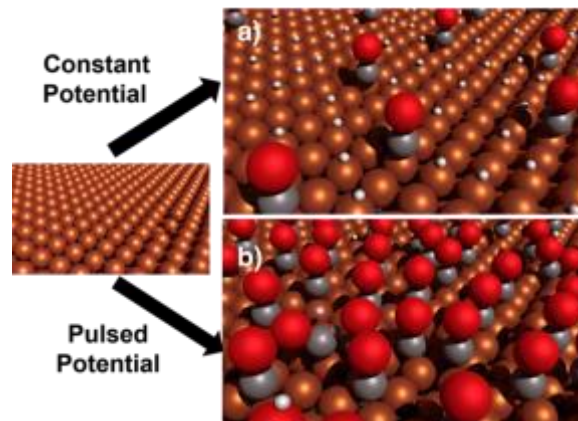


**Figure 3:** 3D scheme of the proposed explanation to the pulsing effect. a)  $H^+$  being adsorbed on the electrode surface during constant potential due to attraction towards the negatively charged metal surface, occupying most active sites. b)  $H^+$  being repelled at the anodic potential by electrostatic interactions, causing the adsorption of CO molecules on the metal surface.

The former requires a much more complex experimental design with spectroscopic analyses, therefore is out of the scope of this discussion. As a first approach to address the latter, the same experimental design was used but the period of  $t_c$  and  $t_a$  was changed to  $t_c = 100$  ms,  $t_a = 50$  ms and the inverted periods were also tested (**Figure 4**). The results

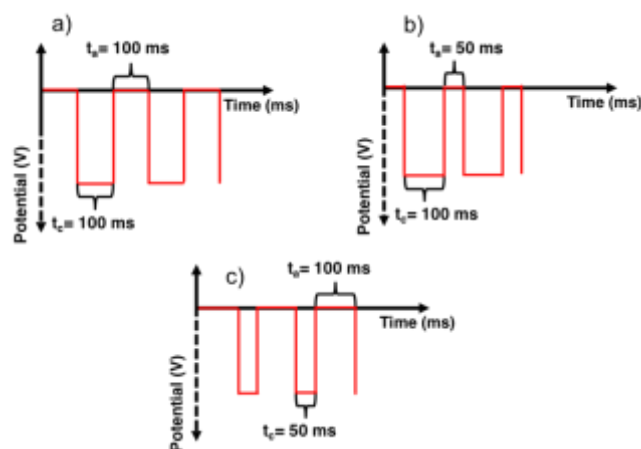


**Figure 4:** Pulsing potentials scheme. a) symmetric pulsing with  $t_c = t_a = 100$  ms. b) asymmetric pulsing with  $t_c = 100$  ms and  $t_a = 50$  ms. c) asymmetric pulsing with  $t_c = 50$  ms and  $t_a = 100$  ms.

showed a slightly improve in CO % in comparison with the symmetric pulse when the  $t_c = 100$  ms and  $t_a = 50$  ms parameters were used. However, the difference between both conditions is within the error of one another, implying that no significant changes were encountered. On the other hand, when using the  $t_c = 50$  ms and  $t_a = 100$  ms parameters, the CO% was lowered which means it did not helped to significantly increase selectivity (**Figure 5**).

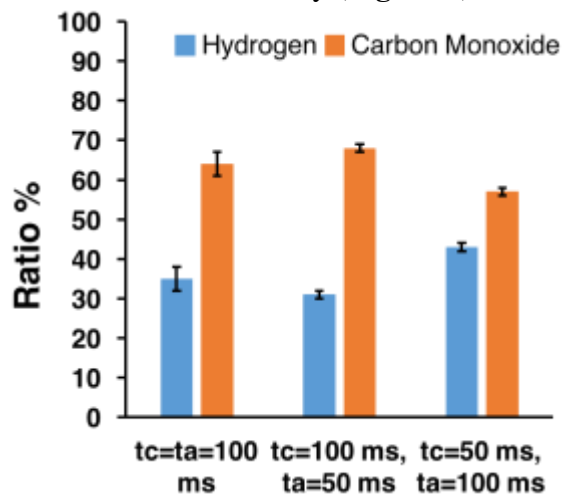


**Figure 5:** Asymmetric pulsing experiments results varying the period between the cathodic and the anodic pulse in comparison with the symmetric pulse with  $V_a = 0$  mV.

As a second approach to understand the phenomenon, the same pulsing experiments were done but the  $V_a$  was changed to an even more positive potential, +500 mV, but not positive enough to provoke the oxidation of the Au electrode. Presumably, if the repelling effect is taking place and  $H^+$  are being in fact repelled from the Au surface at the anodic pulse, an improve of CO yields is expected to be observed by changing from  $V_a = 0$  mV to  $V_a = +500$  mV because the electrostatic shock would be stronger. Surprisingly, the results suggested that by using a more positive  $V_a$ , the CO % is in fact decreased,

rather than enhanced (**Figure 6**). This result was quite unexpected because so far, one of the most coherent hypothesis is the repelling effect of  $H^+$  within the anodic pulse period.

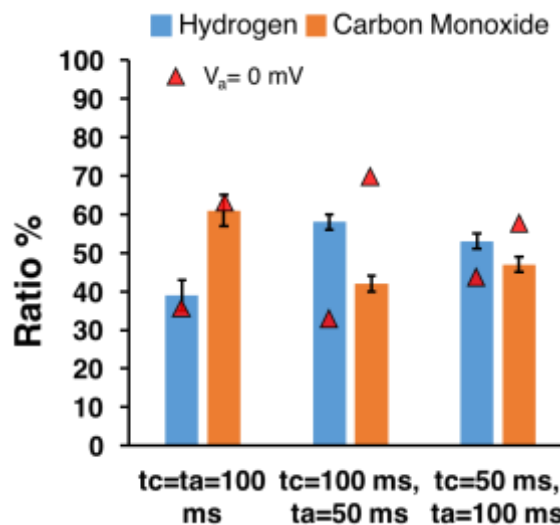


**Figure 6:** Pulsing experiments with  $V_a = 500$  mV in comparison with the previous pulsing experiments having  $V_a = 0$  mV

Jiao and Xu *et.al.*<sup>5</sup> used attenuated total reflectance-surface enhanced infrared absorption spectroscopy (ATR-SEIRAS) under similar conditions to study the species present by scanning from -0.6 V to +1.0 V vs reversible hydrogen electrode (RHE) at 10 mV/s and reported a CO adsorbed ( $CO_{ads}$ ) peak from 2050-2100  $cm^{-1}$  that reached a maximum intensity at  $\sim 0.4$  V vs RHE. This raises another hypothesis to address; the enhancement of the  $CO_2RR$  when using pulses is due to the displacement of  $H^+$  atoms by CO being attracted towards the Au surface and is getting adsorbed until the change in potential is taken place. Another set of pulsing experiments was performed, changing the  $V_a$  to 0.4 V vs RHE. However, a conversion of potentials from RHE to Ag/AgCl in KCl 3.5 M must be done first. To do so, eq. 1 was used and the resulting V vs Ag/AgCl was -200 mV.

$$V \text{ vs. RHE} = V \text{ vs. Ag/AgCl} + 0.197 + 0.059 * (pH) \quad (eq. 1)$$

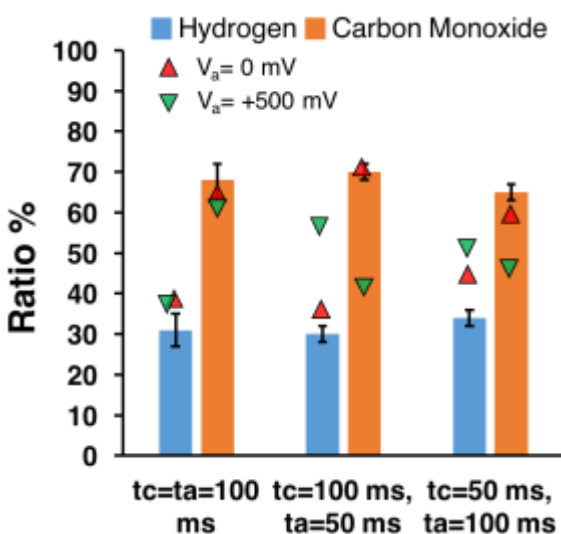


**Figure 7:** Pulsing experiments with  $V_a = -200$  mV in comparison with the previous pulsing experiments having  $V_a = 0$  mV and  $V_a = +500$  mV

As a matter of fact, by using  $-200$  mV as the anodic potential the CO% turned out to be the highest ratio we have encountered so far. This result agrees with the literature and suggests that the CO formed in the cathodic pulse is being adsorbed at the surface in the anodic pulse, displacing the protons from the active sites of the electrode and diminishing the yields of HER implying that the last presented hypothesis is more likely to be truth.

#### IV. CONCLUSIONS

In summary, we have presented a simple, effective, and convenient way of enhancing the selectivity of CO<sub>2</sub>RR by applying pulses and alternating between two potentials. In general, it was observed that changing the ratio of the  $t_c$  and  $t_a$  by same, double, or half when using 100 ms and 50 ms has little or no effect in the selectivity towards CO. Moreover, it was demonstrated that the anodic potential chosen plays a key factor on enhancing the production of CO and suppressing the HER. However, further studies must be done with other pulses

periods to see if the yields can be enhanced. In addition, fundamental electrochemical studies must be done to characterize the pulses and have a better idea of what is happening at the Au electrode surface. Also, additional spectroscopic must be performed in order to have a better understanding of this reaction. Ultimately, this relatively simple experimental setup can provide important fundamental insights into the reaction kinetics and coupled sub-processes involving surface reactions and mass transport to and from the electrode.

#### V. ACKNOWLEDGEMENTS

This work was supported in part by the Cornell Center for Materials Research with funding from the Research Experience for Undergraduates program (DMR-1460428 and DMR-1120296).

#### VI REFERENCES

- (1) Earth Systems Research Laboratory, Trends in Atmospheric Carbon Dioxide. <http://www.esrl.noaa.gov/gmd/ccgg/trends/index.html>, accessed August 2017.
- (2) Solomon, S. Climate Change 2007: contribution of Working Group I to the Fourth Assessment Report of the Intergovernmental Panel on Climate Change; Cambridge University Press: Cambridge, 2007.
- (3) Liu, M.; Pang, Y.; Zhang, B.; Luna, P. D.; Voznyy, O.; Xu, J.; Zheng, X.; Dinh, C. T.; Fan, F.; Cao, C.; Arquer, F. P. G. D.; Saefi, T. S.; Mepham, A.; Klinkova, A.; Kumacheva, E.; Filletter, T.; Sinton, D.; Kelley, S. O.; Sargent, E. H. *Nature* 2016, 537 (7620), 382–386.
- (4) Zhu, W.; Michalsky, R.; Metin, Ö.; Lv, H.; Guo, S.; Wright, C. J.; Sun, X.; Peterson, A. A.; Sun, S. *Journal of the American Chemical Society* 2013, 135 (45), 16833–16836.
- (5) Dunwell, M.; Lu, Q.; Heyes, J.; Rose, J.; Chen, J.; Yan, Y.; Jiao, F.; Xu, B. *J. Am. Chem. Soc.*, 2017, 139 (10), pp 3774–3783

# Engineering a bioreactor system to understand the effects of hemodynamic forces on developing atrioventricular (AV) valves

*Hegab, R., Bassen, D., Butcher, J.  
August 2017 CCMR REU Program*

## **Abstract**

Gaining a greater comprehension of the developmental biology behind valve morphogenesis is vital for the engineering a suitable valve replacement that can grow along with pediatric patients. Initial studies have shown hemodynamic forces drive the early stages of valvulogenesis especially during epithelial-to-mesenchymal transformation (EMT). However, not much has been uncovered of the role of hemodynamic forces in shaping the symmetric cushion into well-defined leaflet of a mature valve during the middle stages of valvulogenesis. Therefore, in order to better comprehend the morphogenesis of the atrioventricular valve, we need to further investigate the role of hemodynamic forces in the middle stages of valve development. In this study, we focused on developing a bioreactor system that recreates the dynamic environment of the early stages of the development of atrioventricular valve. Our goal was to fabricate a system that produced a laminar flow through canal in which live tissue (specifically atrioventricular cushions of an embryonic chick) could remain viable over a long period of time. In this study, we designed and fabricated a bioreactor system within which HH25 stage chick AV tissue were seeded and exposed to oscillatory shear stresses. The flow profile within the system was characterized experimentally and calculated to confirm it accurately mimicked physiologically shear stress values. Moreover, the ability of AV tissue to remain adhered and viable in the system over long periods of time under oscillatory shear conditions was confirmed. In essence, with our fabricated bioreactor system with further optimization will now allow us to run long term studies to further reveal of how hemodynamic forces affect the developing atrioventricular valves.

## **Keywords**

Valvulogenesis      Bioreactor      Hemodynamics      Atrioventricular Valves

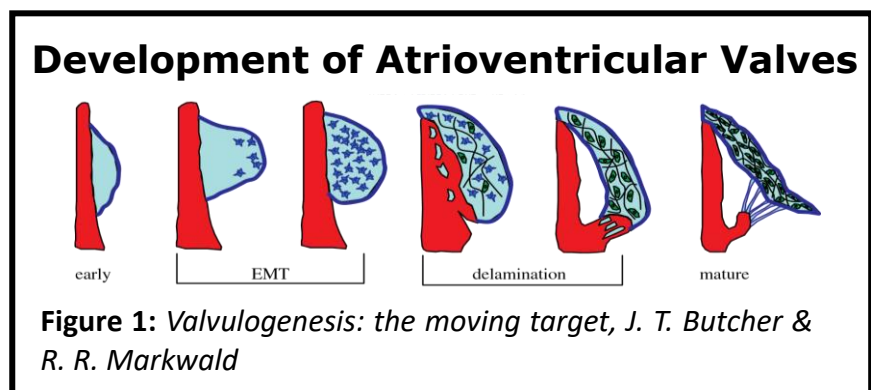
## Introduction

Affecting approximately 1% of all Americans, heart defects attained during embryonic development often are debilitating and require invasive surgery and vigorous drug treatment. Whether the defect is found early on or later in life, most heart valve defects require valve replacement or multiple surgeries especially for pediatric cases. While the common treatment of mechanical or biological prosthetic is satisfactory fix for elderly patients, the current valve replacements available are not an ideal fix for pediatric patients [1]. In order for engineers to be able to develop a satisfactory valve replacement for pediatric patients, the inner workings of the process of embryonic heart development need to be unveiled.

The development of the human heart, a complex process, involves numerous and varying genetic networks, signaling mechanisms, types of cells, and morphogenetic events. Researchers have been able to link specific genetic pathways and cell types to

each stage of embryonic heart development. In fact, explicitly, much has been discovered of the inner workings of a cellular process called epithelial-to-mesenchymal transformation (EMT) which is a key event in the formation of the heart valves (**Figure 1**). During EMT, endocardial cells detach from the epithelium and differentiate into mesenchymal cells, which will then migrate into cardiac jelly and form the cushions of the atrioventricular valves [2].

Specifically, researchers have uncovered a link between hemodynamic forces and endothelial cell development in the embryonic heart. Both Mahler et. al and Yalcin et al conclude that the low wall shear stress may help promote regression of cardiac jelly and the formation of myocardial trabeculations; whereas, higher wall shear stress may promote cardiac jelly expansion and EMT. Not only does the amount of force affect cellular response, but the direction of the flow affects the direction of cell adhesion [3,4]. Overall, the mechanical environment created by different regions of the heart differ and thus, the differing mechanical stimuli leads to different types of pathology in the different regions. Furthermore, Tan et al demonstrates that these flow-generated forces are also capable of driving valve morphogenesis and fibrous ECM expression during development [5]. In other words, hemodynamic forces play a key role in shaping the blob of cell formed in EMT into the formation of well-defined leaflet of a mature heart valve. Thus, in order to better comprehend the morphogenesis of the atrioventricular



valve, we need to further investigate the role of hemodynamic forces in the middle stages of valve development.

In order to further uncover the effects of mechanical stimuli on valve development, researchers have begun developing microfluidic platforms or bioreactors to mimic the 3D vascular microenvironment. Particularly, these bioreactor systems recreate the dynamic atrioventricular canal environment in order to allow the ability to study the effects of mechanical forces of fluid flow on variety aspects of heart development including EMT. By understanding the role of hemodynamics on all stages of valve formation, we will further be able to understand the reemergence of embryonic phenotypes of valvular endothelial cells (possibly being a significant mechanism of valvular disease initiation/progression) [3].

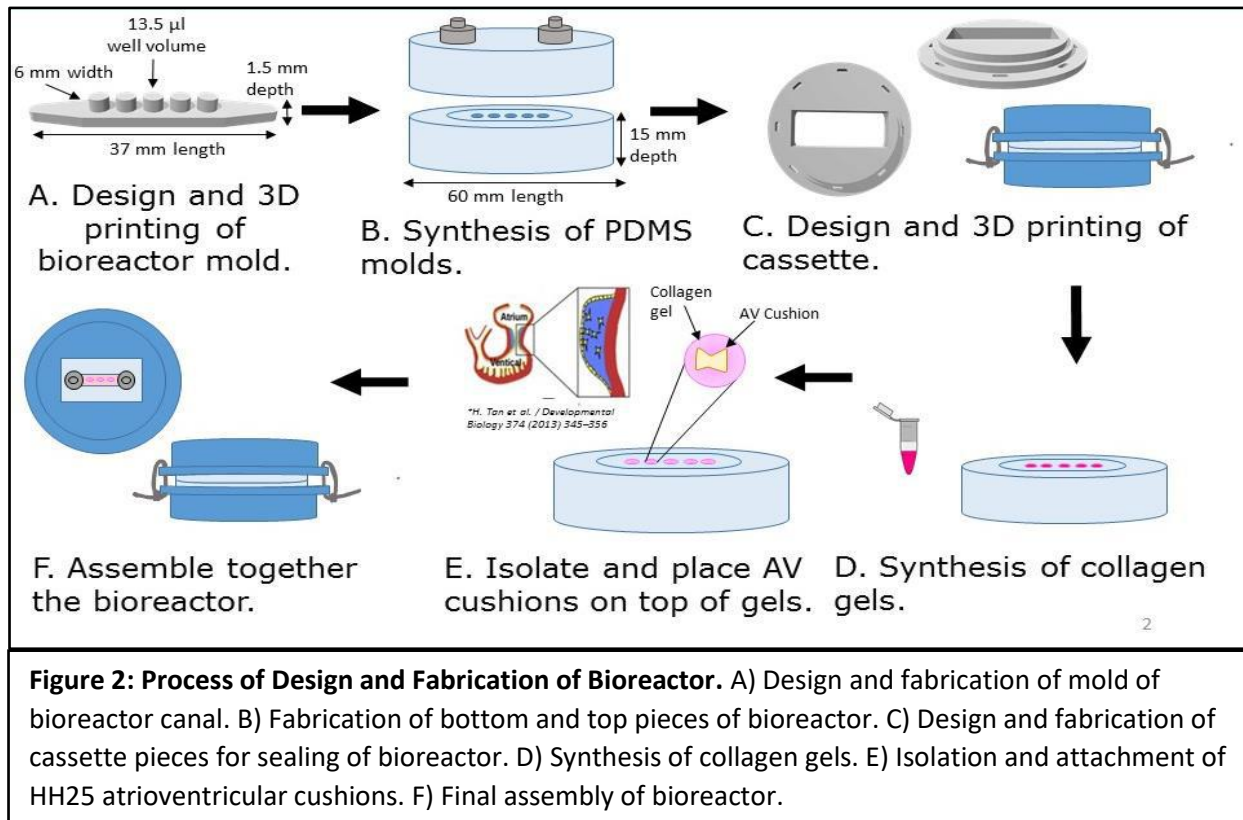
## Objectives

To further comprehend the relationship between hemodynamic forces and stages of valve development between EMT and maturity, in this study, we focused on developing a bioreactor system that recreates the dynamic environment of the early stages of the development of atrioventricular valve. Our goal was to fabricate a system that produced a laminar flow through canal in which live tissue (specifically atrioventricular cushions of an embryonic chick) could remain viable over a long period of time. Ultimately, in meeting these specifications, our bioreactor system will allow the future ability to perform extended studies on the effects of hemodynamic forces on developing atrioventricular valves.

## Methods

### Design and Fabrication of Bioreactor

The bioreactor consists of one canal which is 37 mm long, 6 mm wide, and 3 mm deep and has 5 wells with the volume of 13.5 ul. In order to form this canal, a mold was designed on SolidWorks (**Figure 2A**), 3D printed with PLA filament, and casted in 60 x 15 mm petri dish filled with 10:1 Polydimethylsiloxane (PDMS). The canal mold casted PDMS gel was then cured in 60°C oven over 4 hours forming the bottom piece of the bioreactor (**Figure 2B**). For the top piece of the bioreactor, holes were drilled into the petri dish to align with the ends of the canal. Then, the male luers were placed in the holes and 10:1 PDMS was casted in the dish and cured for four hours in 60 °C oven (**Figure 2B**).



In order to hold the two pieces of PDMS gel together and to seal the canal, the two pieces were sandwiched together in a 3D printed circular cassette (**Figure 2C**) which later will be clasped together using zip ties. Before clasping together the cassette, the 5 wells of the canal were filled with collagen gels of concentration 2.0 mg/ml (**Figure 2D**). Three dimensional collagen gels at a concentration of 2.0 mg/mL collagen were made by combining ice-cold 3X Dulbecco's Modified Eagle's Medium (DMEM), 1% Chick Serum (CS, Life Technologies), sterile 18 MΩ water, 0.1 M NaOH, and rat tail collagen I. After curing the collagen gels for 17 minutes at 37 °C and 5% CO<sub>2</sub>, isolated HH25 atrioventricular cushions were placed on top of each well and cured for another 30 minutes in the incubator (**Figure 2E**). Then, top piece PDMS was placed over the bottom piece PDMS aligning the luers with the ends of the canal. The two pieces were sandwiched and clasped together in the zip tied 3D printed cassette (**Figure 2F**). All parts are autoclavable except for the two pieces of the cassette and 6 inch zip ties which were soaked in 70% ethanol for 15 minutes for sterilization.

## Bioreactor Characterization

### Laminar Flow Characterization Experiment

The bioreactor was designed to provide physiologically relevant levels of steady or oscillatory shear stress over the surface of AV cushions. Assuming fully developed,

incompressible, laminar flow in the canal of the bioreactor, shear stress is a function of the channel geometry, flow rate, and fluid viscosity according to Equation (1):

$$\tau_w = 6Q\mu/h^2w \quad (1)$$

Where  $\tau_w$  is the shear stress at the top and bottom surfaces of the chambers,  $\mu$  is the fluid viscosity,  $Q$  is the volumetric flow rate,  $h$  is the height of the chamber, and  $w$  is the width of the chamber. Viscosity was assumed to be  $3.3 \times 10^{-2}$  dyne\*s/cm<sup>2</sup> and density to be  $1.1 \times 10^3$  kg/m<sup>3</sup> [3].

In order to verify that laminar flow through our bioreactor canal, we conducted a flow characterization study. Additionally, the purpose of this study was to measure the linear velocity over the samples and to also confirm that the collagen gels were flush with the bottom of the channel. In this study, we diluted Polysciences Fluoresbrite® YG Microspheres 10.0 $\mu$ m to a concentration of 10,000 particles/ml of which we pumped through our bioreactor with an Aladdin-6000 syringe pump at 5 ml/min, 10 ml/min, and 15 ml/min to produce 1.22 dyne/cm<sup>2</sup>, 2.44 dyne/cm<sup>2</sup>, and 3.67 dyne/cm<sup>2</sup> respectively. In order to measure the velocity of the microspheres flowing at the varying flow rates through the bioreactor, we captured the microspheres flowing through under Zeiss stereomicroscope with Infinity camera. Then, using Fiji, we analyzed the velocity of the microspheres in order to calculate the actual volumetric flow rates of the canal.

## Tissue Adhesion and Viability

In order to allow future long term studies on how hemodynamic forces affect AV tissue development to be conducted using our bioreactor, we needed to have fabricated a bioreactor in which AV tissue remains attached and viable under oscillatory flow over periods of several hours. To confirm that our bioreactor held this criteria, we ran long term oscillatory flow experiments.

### Atrioventricular Cushion (AVC) Oscillatory Shear Experiment

For this experiment, after the 3D collagen constructs had been added to the wells of the bioreactor canal and incubated for 17 minutes at 37°C and 5% CO<sub>2</sub>, isolated HH25 isolated AV cushions were placed on top of the three middle collagen filled wells. Then the bioreactor was fully assembled and connected to the Aladdin-6000 syringe pump full of M 1X199 media with 1%

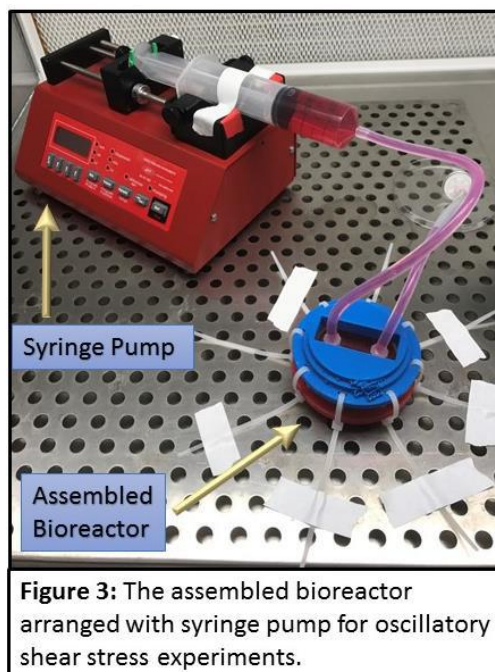


**Figure 3:** The assembled bioreactor arranged with syringe pump for oscillatory shear stress experiments.

chick serum and 0.1% insulin (ITS) using \_\_ tubing (set up seen in **Figure 3**). Placed in the incubator at 37°C and 5% CO<sub>2</sub>, for 6 hours, the syringe pump ran oscillatory flow of 8.2 ml/min at 1 Hz (producing 2 dyne/cm<sup>2</sup>) through the bioreactor canal over the adhered AV tissue.

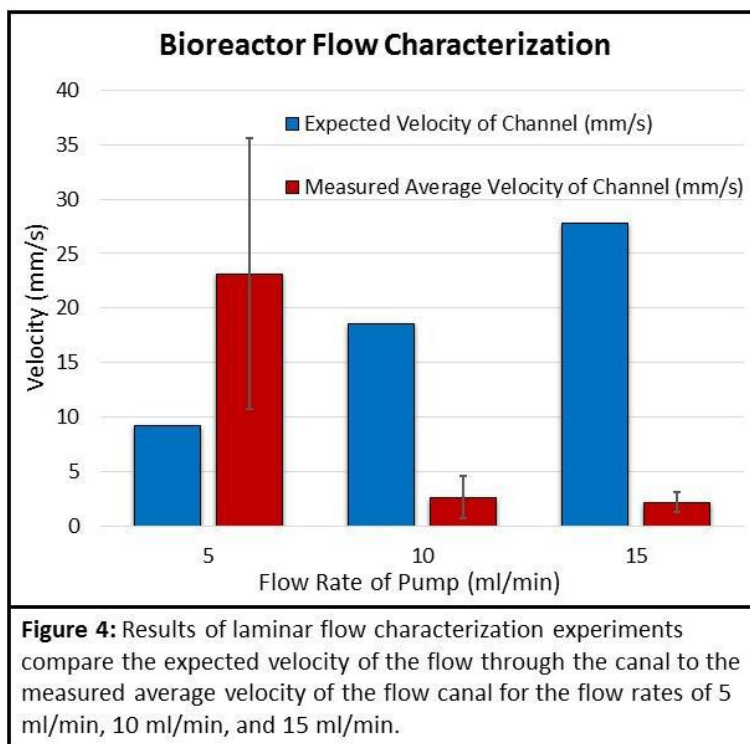
After 6 hour oscillatory flow, the bioreactor was disassemble and the tissue was stained with EDA (dead) and green calcein (live) for a live/dead assay. Using a Zeiss microscope, fluorescent images were taken of the stained tissue in order to confirm its viability. After live/dead assay imaging, the tissue was then fixed in 4% paraformaldehyde (PFA) for 30 minutes and then stained with DAPI (nucleus stain) and phalloidin (cytoskeleton stain) for confocal imaging.

## Results and Discussion

### Laminar Flow Characterization Experiment

To calculate the measured average velocities corresponding to these volumetric flow rates, videos taken of the fluorescent microspheres flowing at each flow rate through the canal. For each flow rate video, the distance of every visible fluorescent microsphere was measured in Fiji and divided by the number of frames times total time of frame in order to calculate velocity. The velocities for one flow rate were then averaged together to produce the measured average velocity.

By manipulating equation 1 and using known geometries of the bioreactor canal and volumetric flow rates of the pump, the expected velocities corresponding to the flow rates 5 ml/min, 10 ml/min, and 15 ml/min ran in the laminar flow experiments were 9.26 mm/s, 18.52 mm/s, and 27.78 mm/s respectively. In comparison, the measured average velocities for the corresponding flowrates 5 ml/min, 10 ml/min, and 15 ml/min were  $23.17 \pm 12.37$  mm/s,  $2.64 \pm 1.93$  mm/s, and  $2.20 \pm 0.89$  mm/s respectively. As seen in **Figure 4**, the only flow rate in which the error bars of the measured average velocity come



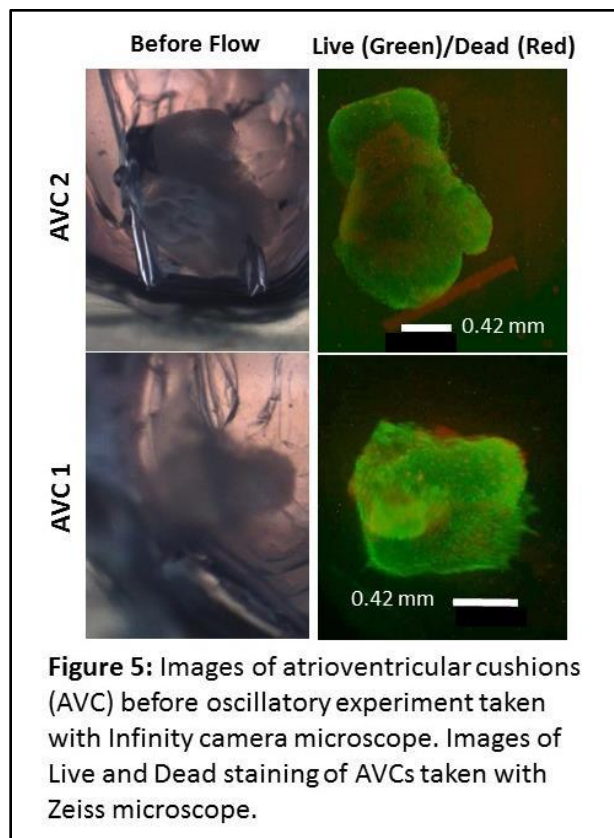
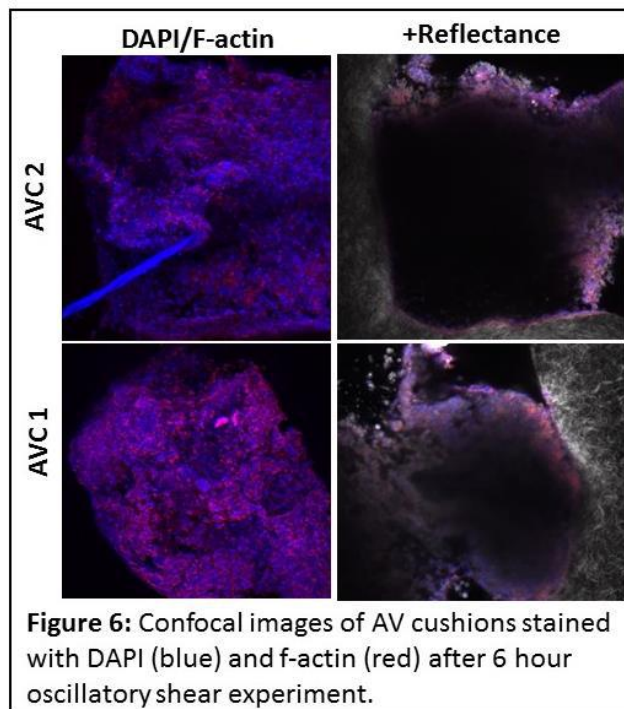
within the range of the expected velocity was 5 ml/min. In contrast, the expected velocities of the flow rates of 10 ml/min and 15 ml/min were more than 10 times faster than the measured average velocities.

The large discrepancy between the expected velocities and the measured average velocities for the flow rates 10 ml/min and 15 ml/min could be due to the insufficient sensitivity of the camera leading to an exposure time too long to capture motion at those rates. Thus, since the measured average velocities were based upon the velocities of the moving microspheres clear enough to track in Fiji, the measured average velocities lack the faster moving microspheres resulting in their values to be lower. In the future, this experiment could be optimized by utilizing camera with a better ability to capture higher quality video of the faster moving microspheres. In conclusion, based upon the measured average velocity in comparison to the expected velocity for 5 ml/min flow rate, the flow through our bioreactor canal obtains a laminar profile.

## Tissue Adhesion and Viability Studies

### AVC Oscillatory Shear Experiment

After being subjected to oscillatory shear conditions for 6 hours within the bioreactor, the AV cushions were still adhered to the collagen 3D constructs.

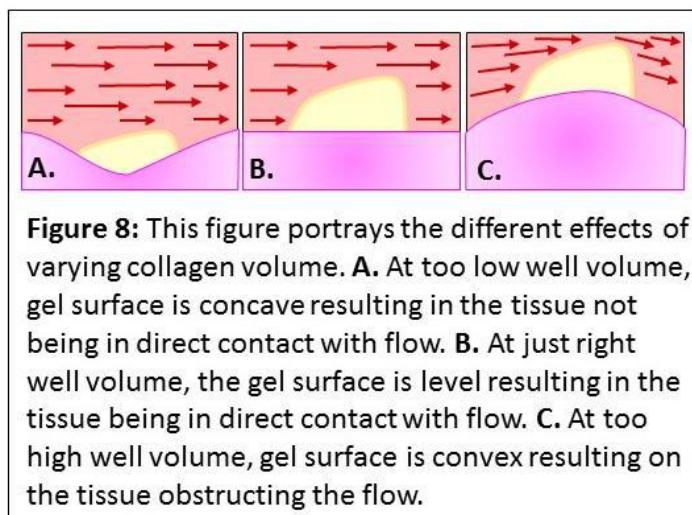
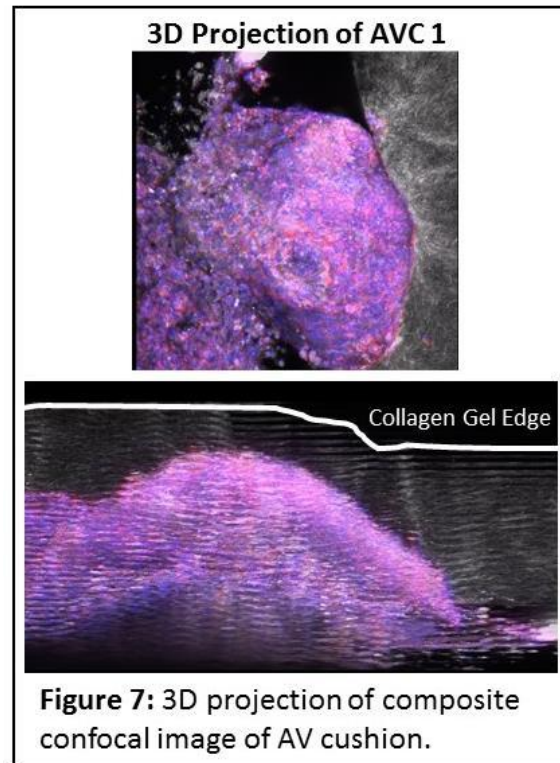


More importantly, after the 6 hours, the majority of the AV tissue was viable as seen in the live/dead stains in **Figure 5**. Furthermore, the AV cushions retained their shape throughout the experiment. In fact, the confocal images in **Figures 6** and **7** reveal how AV tissue integrated with the

collagen gel in order to remain adhered during oscillatory shear conditions. Moreover, the 3D projections in **Figure 7** demonstrate that despite the concavity of the collagen gel surface, the AV tissue still sits above the gel. The tissue sitting above the gel confirms that the AV tissue was able to adhere without sinking into the gel. However, the concavity of the tissue interface to the gel portrays that the shear stress values will be less and the flow will not be in direct contact. Thus, we will need to further optimize the collagen gel and tissue adhesion protocol.

We did begin further optimizing the collagen gel and tissue adhesion protocol. Ideally, we want to optimize the protocol to where it produces a collagen gel cured fully except for a thin layer across the surface so that the tissue can be glued with the remaining uncured gel. Specifically, we looked at how varying the curing times (15, 17 and 20 minutes) of the collagen (amount of time spent in the incubator after being distributed to the PDMS wells) affected tissue adhesion. When collagen was allowed to cure for 15 minutes, gels were not cured and tissue sank into the gel. At 20 minutes, the gel was too cured and the tissue curled up. Finally, at 17 minutes, the gel was cured just enough that there was a coat left uncured to allow tissue adhesion. However, the volume of collagen in the well was insufficient causing the tissue to sit lower in the gel (seen in **Figure 7** and **Figure 8a**). Thus, there is a further need to optimize the step of how much volume of collagen is pipetted to each well.

Ideally, in order for the tissue to be in direct contact with the flow, we want the surface of the gel to be level and parallel to the bottom of the canal (**Figure 8b**). Yet, when wells' volume of collagen is too low, the gel concaves and tissue sinks into the gel without being in contact with flow (**Figure 8a**). When the wells' volume overflows, the cured gel concaves up obstructing the flow and exposing too much of the tissue (**Figure 8c**). Essentially, in order



have an optimal system in which the seeded AV tissue actually is subjected to shear stresses calculated from the known laminar flow rates, we need a system in which the AV tissue adheres to gel surface level with the bottom of the canal; thus, in direct contact with the flow. Despite the need for future optimizations, overall, the results from the oscillatory shear experiment verified that the bioreactor designed would allow AV tissue to remain adhered and viable during long term experiments.

## **Conclusion**

We have designed and fabricated a bioreactor system in which developing atrioventricular valves can be seeded and exposed to oscillatory shear stresses. The flow profile within the system was characterized experimentally and calculated to confirm it accurately mimicked physiologically shear stress values. Moreover, the ability of AV tissue to remain adhered and viable in the system over long periods of time under oscillatory shear conditions was confirmed. After further optimization, our fabricated bioreactor system will now allow us to run long term studies to further reveal of how hemodynamic forces affect the developing atrioventricular valves. By further understanding the relationship between the developing AV tissue and hemodynamic forces, we will be able to further expand comprehension of the developmental biology of the heart. Although much of the developmental biology of the heart has been discovered, the picture is not complete. There is still a great need to further unravel the complex story of the development of the embryonic heart in the context of mechanical forces. By further unveiling and comprehending the inner workings of the developing heart, we can obtain an improved prospective in innovating heart valve replacements and regeneration.

## **Acknowledgements**

This work was supported by the Cornell Center for Materials Research with funding from the Research Experience for Undergraduates program (DMR-1460428 and DMR-1120296).

## Citations

1. Butcher JT, Markwald RR. Valvulogenesis: the moving target. *Philosophical Transactions of the Royal Society B: Biological Sciences*. 2007;362(1484):1489-1503. doi:10.1098/rstb.2007.2130.
2. Lin C-J, Lin C-Y, Chen C-H, Zhou B, Chang C-P. Partitioning the heart: mechanisms of cardiac septation and valve development. *Development (Cambridge, England)*. 2012;139(18):3277-3299. doi:10.1242/dev.063495.
3. Mahler GJ, Frenzl CM, Cao Q, Butcher JT. Effects of shear stress pattern and magnitude on mesenchymal transformation and invasion of aortic valve endothelial cells. *Biotechnology and bioengineering*. 2014;111(11):2326-2337. doi:10.1002/bit.25291.
4. Yalcin HC, Shekhar A, McQuinn TC, Butcher JT. Hemodynamic Patterning of the Avian Atrioventricular Valve. *Developmental Dynamics*. 2011;240(1):23-35. doi:10.1002/dvdy.22512.
5. Hong Tan, Stefanie Biechler, Lorain Junor, Michael J. Yost, Delphine Dean, Jinqing Li, Jay D. Potts, Richard L. Goodwin, Fluid flow forces and rhoA regulate fibrous development of the atrioventricular valves, *Developmental Biology*, Volume 374, Issue 2, 2013, Pages 345-356, ISSN 0012-1606, <http://dx.doi.org/10.1016/j.ydbio.2012.11.023>.

# Electrochemical imaging of charge trapped thin film polymer cathodes

Mihail R. Krumov, Luxi Shen and Héctor D. Abruña\*

Department of Chemistry and Chemical Biology, Baker Laboratory, Cornell University, Ithaca NY 14853-1301

---

**ABSTRACT:** Charge trapping of redox functionalized conducting polymers (CPs) has a deleterious effect on the practical capacity of these battery electrodes. Despite this, the mechanism of charge trapping is still not well understood. Based on previous work, we theorize insulating domains exist within the polymer, and that these domains lead to charge trapping. Using Scanning Electrochemical Microscopy (SECM) we discover small, disperse insulating regions on both TMPD functionalized and unfunctionalized polypyrrole films. Our results suggest that these insulating regions likely are not the cause of charge trapping.

---

## INTRODUCTION

Advances in electrical energy storage (EES) systems are needed to accommodate the shift towards renewable energy sources<sup>1</sup>, and increasingly power hungry technologies<sup>2</sup>. Polymer based electrodes are an emerging battery technology that addresses many of the key drawbacks of metallic based battery systems such as slow charge/discharge rates, fixed operating voltage, and limited Li/transition metal availability.<sup>3, 4</sup> Hybrid organic electrodes utilize a conducting polymer (CP) backbone to electronically link strategically chosen redox active pendants (RAPs) to the current collector. This strategy allows multiple electrons to be stored per monomeric formula unit, and to achieve fast electron transfer kinetics associated with simple redox processes. Together, these traits translate into high capacities and fast cycling rates for polymer based batteries.

RAPs capable of exchanging two (or more) electrons are desired because this doubles the theoretical capacity of the electrode. Unfortunately, many CPs functionalized with such RAPs exhibit strongly diminished capacity after the first discharge cycle, due to a phenomenon called charge trapping.<sup>4</sup> Although this process is critical to the success of polymer based EES devices, the mechanism of charge trapping is still not well

understood. Similar charge trapping effects have been previously observed in polymer bilayer films where electronic access to the outer film depends on the charge state of the inner film.<sup>5</sup> We theorize that in hybrid organic electrodes lateral inhomogeneities, specifically insulating domains, exist instead, but have a similar effect on charge transport within the polymer as does the bilayer scheme, thus leading to charge trapping in RAP functionalized CPs.

In this study, we use a toolbox of electroanalytical techniques centered around Scanning Electrochemical Microscopy (SECM) to investigate the mechanism of charge trapping in *N,N,N',N'*-tetramethylphenylenediamine (TMPD) functionalized polypyrrole (PPy) thin films. SECM relies on a small probe electrode to electrochemically interrogate a substrate surface. Compared to other electrochemical techniques, it has the advantage of operating under steady state, providing spatially localized information, and is selective towards surface processes<sup>6</sup>. Among other things, SECM has the ability to image electrochemical reactivity of a surface<sup>7</sup>, and to measure the relevant kinetic parameters<sup>8</sup>. Thus, SECM provides the pertinent qualitative and quantitative information needed to understand the mechanism of charge trapping.

## RESULTS AND DISCUSSION

A cyclic voltammogram of PPy-TMPD (Figure 1, black curve) illustrates charge trapping. Beginning at  $-0.6$  V vs  $\text{Ag}/\text{Ag}^+$ , the potential of the electrode is scanned in the positive direction. At ca.  $-0.25$  V and  $+0.30$  V, oxidation peaks appear corresponding to the first and second oxidation of the TMPD pendant. On the reverse scan, the film is reduced from the +2 to the +1 charge state as indicated by the reduction peak at ca.  $+0.3$  V. However, as the electrode potential returns to  $-0.6$  V, the reduction peak at  $-0.25$  V is much smaller than the corresponding oxidation, indicating much of the film remains in the +1 charge state. By the third cycle (Figure 1, red curve), the oxidation peak at  $-0.25$  V is nearly absent because the polymer is already trapped in the first oxidation state.

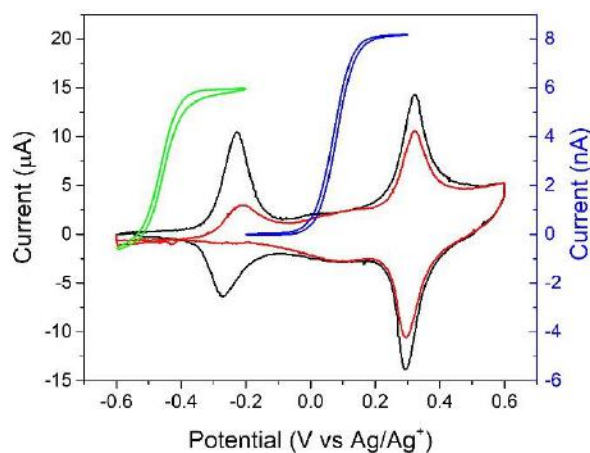


**Figure 1.** CV of PPy-TMPD for the first cycle (black curve) and third cycle (red curve), recorded in  $0.1$  M TBAP/MeCN at  $20$  mV/s. Steady state CVs of ferrocene (blue curve) and decamethyl ferrocene (green curve) recorded in a  $1$  mM solution of the respective compound are overlaid to show their relative oxidizing power.

The potential at which this redox process occurs is an important consideration in mediator selection for electrochemical imaging. In a SECM experiment, communication between the probe and the substrate is achieved via a redox mediator. Thus, the mediator formal potential can dictate the type of interaction that is observed with the

substrate. For our experiments, we selected ferrocene (Fc) and decamethylferrocene (dFc) as mediators because of their ability (or inability) to oxidize the film. Figure 1 illustrates the relative oxidizing power of Fc (blue curve) and dFc (green curve). As can be seen from the halfwave potential of these CVs, the formal potential of Fc is ca.  $0.3$  V positive of the film's first oxidation potential, whereas the dFc formal potential is ca.  $0.2$  V negative of the film's first oxidation potential. Therefore, given fast electron transfer kinetics, the Fc/Fc<sup>+</sup> couple can oxidize the film, whereas dFc cannot.

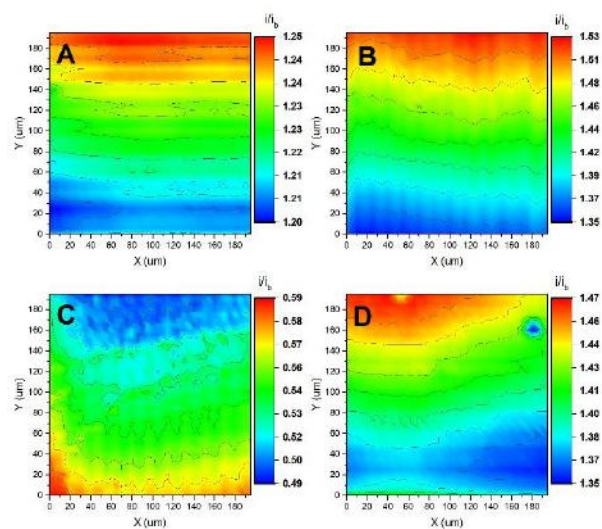


**Figure 2.** Electrochemical imaging (A) of bare GC using Fc (B) of bare GC using dFc (C) of PPy-TMPD film electropolymerized on GC using dFc (D) and of same film using Fc. All images are taken at the same physical location on the surface in a  $1$  mM solution of the respective mediator and  $0.1$  M TBAP in acetonitrile. Current is normalized by the bulk steady state current.

PPy-TMPD films are typically electropolymerized onto a glassy carbon (GC) electrode. We therefore first perform an SECM imaging experiment on bare GC to obtain a background for current signals due to morphological influences. Images of GC taken using Fc and dFc as mediators are shown in Figures 2A and 2B respectively. The current signal,  $i$ , is normalized by the bulk steady state current,  $i_b$ ,

measured far from the substrate surface. Figures 2A and 2B show  $i/i_b$  is greater than 1 everywhere on GC. This indicates the substrate is regenerating Fc after it has been oxidized by the probe, creating a positive feedback loop that increases the flux of Fc. Positive feedback is the expected response at a conducting surface such as GC. Further, the response is expected to be independent of the mediator redox potential, as Figures 2A and 2B also show. The current in these images increases in the Y direction, indicating some substrate tilt exists.

The PPy-TMPD film was subsequently electropolymerized on the GC electrode in the SECM cell, and images of the same physical location on GC were taken. These can be seen in Figure 2C and 2D, taken using dFc and Fc as mediators respectively. Figure 2C shows that the current close the PPy-TMPD surface is lower than the bulk current when using dFc. This indicates PPy-TMPD is relatively insulating. The mediator that is oxidized by the probe is not regenerated by the surface because the PPy-TMPD film is not conducting enough to facilitate nonlocal electron transfer to solution species. The current decreases close to the surface in this case because the surface hinders diffusion of mediator to the probe. Imaging the same location using Fc however, produces a positive feedback signal. Presumably, the  $Fc^+$  that diffuses from the probe to the film surface is able to oxidize the PPy-TMPD (Reaction 1) since it has a positive formal potential relative to that of the film. This process regenerates Fc and produces a positive feedback signal because the close vicinity of the probe to the surface decreases the diffusion time of the mediator.



Figure 2D also shows a localized insulating region on the film surface at ca.  $X = 180 \mu\text{m}$ ,  $Y = 170 \mu\text{m}$ . Further imaging reveals multiple such regions exist on the polymer surface, however the size and number density of these insulating regions seems too small to affect bulk charge transport within the

film that can lead to charge tapping to the extreme extent that is observed.

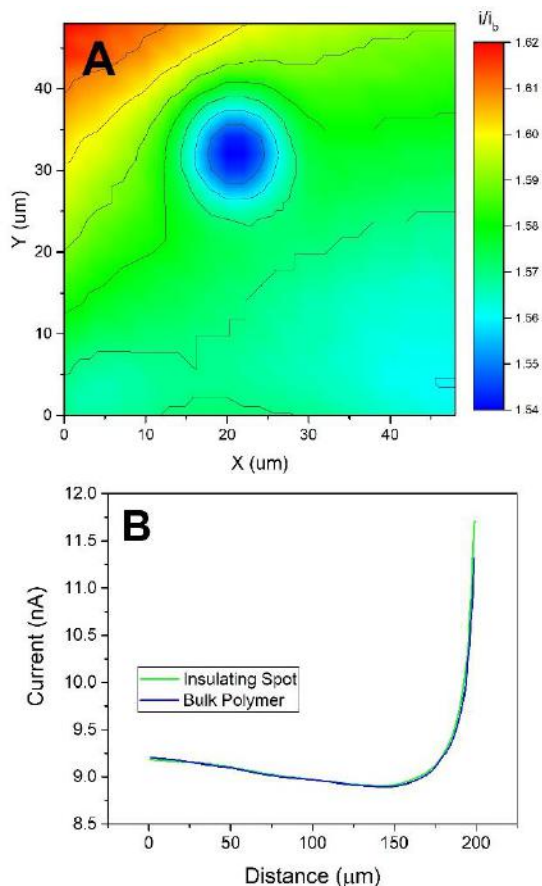


**Figure 3.** (A) High resolution image of an insulating region on PPy-TMPD taken using Fc. (B) Probe approach curves to the insulating region and bulk polymer used to measure electron transfer kinetics.

A higher resolution image of one of these spots is shown in Figure 3A. To further assess the effect of these insulating regions on charge transport within the film, probe approach curves (Figure 3B) were done on the insulating region, and compared to those performed at the bulk polymer. The shape of an approach curve depends on the kinetics of electron transfer between the mediator and substrate. The fact that the approach curves in Figure 3B overlap, indicates that the rate constant for Reaction 1 is nearly identical at these two locations. Since electron transfer kinetics between the mediator and polymer are minimally affected by the insulating regions, the insulating regions

likely have a minimal effect on charge transport within the polymer film as well. Therefore, they are most probably not the cause of charge trapping.

As a control experiment, we synthesized a PPy film without the TMPD pendant. The absence of the RAP means that this film cannot experience charge trapping. In imaging this film using Fc, similar insulating regions were observed as was seen before on the PPy-TMPD film (Figure 4A). Clearly, the conducting polymer backbone is responsible for the origin of these features. Upon cycling the PPy, the insulating region shown in Figure 4A disappeared (Figure 4B). This shows the insulating regions are dynamic in that they respond to electrochemical perturbations such as cycling the film. Therefore, they are not the result of permanent morphological film structure, but are rather dynamic electrochemical features. This again suggest the insulating regions observed are not responsible for charge trapping since cycling the film between -0.6 V and +0.6 V does not restore trapped charge, whereas it does appear to restore the conductivity of the polymer.

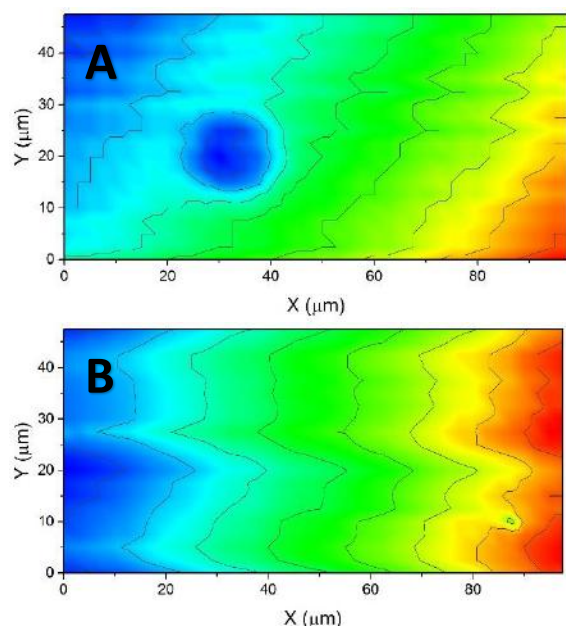


**Figure 4.** Imaging of a PPy film with no TMPD pendants (A) before and (B) after cycling the film between -0.6 V and +0.6 V vs Ag/Ag<sup>+</sup>.

## CONCLUSIONS

Small, localized insulating regions were discovered on the surface of both TMPD functionalized polypyrrole, and unfunctionalized polypyrrole. These insulating regions can change (appear/disappear) as the result of electrochemical perturbations such as cycling or mediator potential, indicating that they are dynamic electrochemical features and not morphological or structural features of the polymer. Unfunctionalized polypyrrole electrodes cannot exhibit charge trapping and thus serve as a control. The existence of insulating regions on these polymer films suggests that the observed insulating regions likely are not related to the phenomenon of charge trapping. Furtherer, these regions are too small and disperse to affect bulk charge transport within the polymer. Together, this suggests that insulating domains are not responsible for charge trapping in the polymer as was hypothesized. New theories and further experiments are needed to elucidate the mechanism of charge trapping on RAP functionalized CPs.

## REFERENCES

1. Dunn, B.; Kamath, H.; Tarascon, J.-M., Electrical energy storage for the grid: a battery of choices. *Science* **2011**, *334* (6058), 928-935.
2. Tang, Y. X.; Zhang, Y. Y.; Li, W. L.; Ma, B.; Chen, X. D., Rational material design for ultrafast rechargeable lithium-ion batteries. *Chemical Society Reviews* **2015**, *44* (17), 5926-5940.
3. Mulzer, C. R.; Shen, L.; Bisbey, R. P.; McKone, J. R.; Zhang, N.; Abruña, H. D.; Dichtel, W. R., Superior charge storage and power density of a conducting polymer-modified covalent organic framework. *ACS central science* **2016**, *2* (9), 667-673.
4. Shen, L.; Mizutani, M.; Rodríguez-Calero, G. G.; Hernández-Burgos, K.; Truong, T.-T.; Coates, G. W.; Abruña, H. D., Hybrid Organic Electrodes: The Rational Design and Synthesis of High-Energy Redox-Active Pendant Functionalized Polypyrroles for Electrochemical Energy Storage. *Journal of The Electrochemical Society* **2017**, *164* (9), A1946-A1951.
5. Abruña, H. D.; Denisevich, P.; Umana, M.; Meyer, T. J.; Murray, R. W., Rectifying interfaces using

two-layer films of electrochemically polymerized vinylpyridine and vinylbipyridine complexes of ruthenium and iron on electrodes. *Journal of the American Chemical Society* **1981**, *103* (1), 1-5.

6. Simpson, B. H.; Rodríguez-López, J., Redox Titrations via Surface Interrogation Scanning Electrochemical Microscopy at an Extended Semiconducting Surface for the Quantification of Photogenerated Adsorbed Intermediates. *Electrochimica Acta* **2015**, *179*, 74-83.

7. Fernández, J. L.; Walsh, D. A.; Bard, A. J., Thermodynamic Guidelines for the Design of Bimetallic Catalysts for Oxygen Electroreduction and Rapid Screening by Scanning Electrochemical Microscopy. M-Co (M: Pd, Ag, Au). *Journal of the American Chemical Society* **2005**, *127* (1), 357-365.

8. Ritzert, N. L.; Rodríguez-López, J.; Tan, C.; Abruña, H. D., Kinetics of Interfacial Electron Transfer at Single-Layer Graphene Electrodes in Aqueous and Nonaqueous Solutions. *Langmuir* **2013**, *29* (5), 1683-1694.

# Implementation of Speckle Patterns in Hydrogels for Quality Digital Image Correlation Measurements

José Lasalde, Mincong Liu, Alan Zehnder

**A challenge for the measurement of deformation fields via Digital Image Correlation (DIC) is the application of speckle patterns on the surface of the material under study that will yield precise and accurate measurements. Moreover, the implementation of suitable speckle patterns in hydrogels can be challenging due to the physical properties of these materials. There are currently limited techniques to determine the quality of a speckle pattern for DIC. We present a variety of speckle patterns applied utilizing the same ink to the surface of hydrogels via airbrushing. Large deformation experiments on hydrogels were examined via DIC at different interrogation cell sizes. Evaluations of the quality of the patterns were made by comparing the strain determined from DIC to the applied strain and by assessing the standard deviation of the strain.**

Digital Image Correlation (DIC) is an optical strain measuring technique. This analysis can qualitatively and quantitatively determine displacement fields at the surface of an object based on the comparison between a reference image taken before deformation, and several pictures taken during the distortion of the object. The accuracy of DIC measurements relies on the proper selection of a subset, or interrogation cell. Selecting the subset size will determine the size of the pattern in the image the software will correlate. The software will then segment the image in several subsets of the selected size and correlate each subset of the reference image with the subsets of the deformed images. Larger subset selection will allow high strain accuracy. However, smaller interrogation cells maximize spatial resolution of the data.<sup>1-2</sup> Equally important for Digital Image Correlation measurements, to obtain accurate results, speckle patterns of the right speckle sizes and distributions need to be applied to the surface of the material.<sup>3</sup> Furthermore, for large deformation experiments, the selection of an appropriate type of speckle pattern is imperative for precise measurements.<sup>4</sup>

Several pattern assessment criteria have been proposed and studied with the intention of finding a quantitative calculation to determine the most adequate patterns for DIC, but almost none have worked. Measurements such as the Shannon Entropy<sup>5</sup> and the Mean Intensity Gradient<sup>6</sup> are examples of assessment criteria that provide a mean value for the whole pattern, disregarding variation between subsets in the pattern, and failing to determine its appropriateness for DIC tests. Morphological approaches to determine the quality of patterns have also been suggested. These work by measuring a mean distribution of speckle sizes in a pattern. The resulting diagram reveals a cumulative distribution of speckle sizes in a pattern.<sup>7-8</sup> On this paper, error analysis of DIC measurements were used to compare with the assessment criteria mentioned previously to conclude which measurements can determine a proper pattern for Digital Image Correlation.

The error analyses include comparison of the mean strain from DIC to the known, applied strain and analysis of the standard deviation of the strain from DIC. The standard deviation is computed as <sup>5</sup>

$$SD_{\epsilon} = \sqrt{\frac{n \sum (\epsilon_{DIC} - \epsilon_{imposed})^2 - (\sum (\epsilon_{DIC} - \epsilon_{imposed}))^2}{n(n-1)}}$$

where  $\epsilon_{DIC}$  is the measured strain of the software and  $\epsilon_{imposed}$  is the imposed strain.

The main goal of this paper is to provide guidance on applying an adequate speckle pattern for DIC analysis of hydrogels. Hydrogels, due to their high-water content and biocompatibility, are biomaterials for applications such as artificial cartilage, vessels and prosthetic joints.<sup>9</sup> Because of this, it is crucial to understand the mechanical behavior of the material. Performing Digital Image Correlation tests on hydrogels will help us comprehend their mechanical performance. A critical problem of performing DIC in hydrogels is that it is highly complicated to implement a quality speckle pattern to the material due to their high content of water. We decided to experiment different speckle patterns through airbrushing. In the literature, it has been suggested that airbrushed patterns produce finer speckle patterns and result in more accurate DIC measurements compared to sprayed patterns or powders.<sup>5</sup>

On this paper, we suggest that speckle patterns in hydrogels airbrushed at higher air pressures have the tendency to be more accurate at any interrogation cell size. Morphological assessments will be able to determine the difference between particle distributions but will not tell you the accuracy of a pattern for Digital Image Correlation. Additionally, neither the Shannon Entropy nor the Mean Intensity Gradient will determine the best pattern for DIC. The error analysis performed demonstrated the suggestion previously mentioned.

## Methodology

**Airbrush** In these experiments, the airbrush used to apply the speckle pattern was an Iwata High Performance HP-C 50th Anniversary Airbrush equipped with a 0.3 mm nozzle cap and 0.3 mm fluid nozzle.

**Ink** The airbrush ink analyzed on this paper was Kohinor Acetate Black Ink, Item #L68600. Another ink tried was the CREATEX Opaque Black ink and. This ink did not give satisfactory results due to sparseness of the pattern after implementation.

**Experiments** The pressure supplied to the airbrush and the rate of ink flow both play a role in the speckle size and density. Pressure is set by a regulator coming from the lab air supply. Ink flow rate is set by how far the airbrush needle is pulled back during spraying. A low flow rates approximately 4 passes of the spray were used to increase the speckle pattern density to an acceptable level. The first experiment used morphological assessments the quantify the differences of particle distributions at different air pressures (PSI) at high ink flux. Different patterns were airbrushed by changing the air pressure from 40 to 80 PSI at every 10 PSI. Images taken of the hydrogels were taken and converted to a black and white image utilizing ImageJ's threshold tool. An example of the steps of converting the image into a black and white image using ImageJ can be found in the Supplementary Figure 5. Every Cumulative Percentage test was done using a fraction of the image cropped, measuring 1200 x 1200 pixels. Examples of the images are found in Supplementary Figure 1.

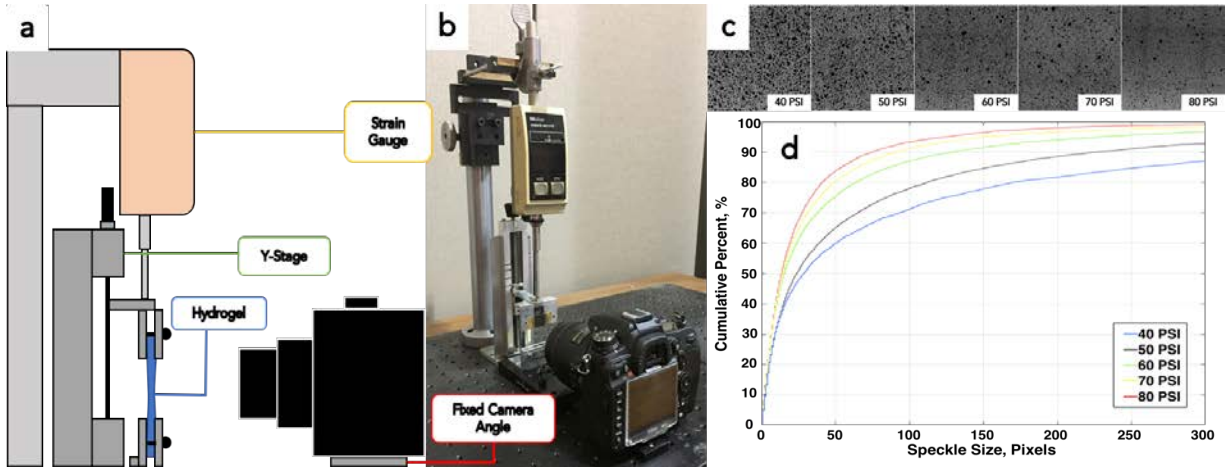


**Figure 1.** (a) Sketch of DIC Setup. (b) Image of real DIC Setup. (c) Speckle Patterns in hydrogel at different PSI at high ink volume. (d) Cumulative Distribution of Speckle Patterns at Different PSI.

We then experimented on airbrushing the hydrogels at different ink volume. Through morphological assessment tests we observed the difference of the airbrushed ink at a high flow vs. a low volume of ink.

DIC experiments were performed in a custom setup (Fig.1a, b). The setup consisted of a fixed camera parallel to the angle of the sample. A y-axis translation device was used to stretch the sample manually to the desired displacement. Utilizing a displacement gauge, we calculated the known strain values at different deformation stages to compare them to the measured strains of the DIC tests. The theoretical strains obtained from the displacement were calculated from the following equation:

$$\varepsilon_{yy} = \frac{1}{2}(\lambda^2 - 1)$$

where  $\lambda$  is the stretch, defined by  $\lambda = L/L_0$ , where  $L_0$  is the initial height of the sample and  $L$  is the current, or stretched height of the sample.

Three speckle patterns of each PSI were implemented. The dimensions of the samples tested were approximately 30.0 mm long by 15.0 mm wide. We then performed error analysis by computing the average strain over a region of interest and comparing that to the known strain and by calculating the standard deviation using the formula previously mentioned. The initial sample length was 20.0 mm. Pictures were taken at strains ranging from 5% to 50% at 5% intervals (1.0 mm-10.0 mm) (Supplementary Fig. 2). Every image was cropped (Approx. 2500 x 3200 pixels) and turned into 8-bit grayscale images. The DIC software used on these experiments was Ncorr's Open Source 2D DIC Matlab Software. The camera used to take the images was a Nikon D7000 with a AF-S Micro NIKKOR 40mm 1:2.8G lens. The initial images measured approximately 3500 x 3200 pixels. The physical size of the pixel was .0083295 pixels/mm.

Shannon Entropy and Mean Intensity Gradient calculations were performed on 8-bit grayscale cropped images of the patterns measuring 1200 x 1200 pixels.

	PSI	Shannon Entropy	Mean Intensity Gradient
Kohinoor Ink	40	7.01	16.95
	50	6.89	16.40
	60	6.93	19.17
	70	6.63	16.58
	80	7.00	18.48

**Table 1.** (a) Average Shannon Entropy and Mean Intensity Gradient of Speckle Patterns.

The Shannon Entropy of the patterns was calculated using the following equation:

$$E = \sum_{j=1}^N p(x_j) \log(p(x_j))$$

where N is the gray level value, i.e. 0 to 255 for an 8-bit gray level image, and  $p(x_j)$  is the count of pixels at the given gray level.

Additionally, the Mean Intensity Gradient of the patterns was calculated from the following equation:

$$\delta_f = \frac{\sum_{i=1}^m \sum_{j=1}^n |\nabla f(x_i, y_j)|}{mn}$$

where  $f(x_i, y_j)$  is the greyscale intensity at location  $(x_i, y_j)$  for an image of  $m \times n$  pixels.

DIC experiments were performed utilizing two different regions of interest (ROI), to compare which would help us obtain the most accurate results. The region of interest (ROI) determines the area of the sample you want to analyze. One of the ROIs measured approximately 10.0 by 10.0mm and the second ROI measured approximately 6.0 by 12.0mm.

Lastly, we did Digital Image Correlation tests at different interrogation cell sizes. The selected subset radii for the experiments were 10, 40, 120 pixels. Error analysis tests were calculated for all interrogation cells at the different PSI rates.

## Results

**PSI Rates** Morphological assessments of the airbrushed patterns at different PSI at high ink flow demonstrated that at lower air pressures, patterns have bigger particle sizes. As shown in Fig. 1d, lower pressure shift the distribution toward larger particles. As the air pressure increases, the speckle patterns become finer, shifting the distribution toward small particles. For example: 60% of the speckles in the pattern at 40 PSI ranged in spackle areas from 0 to 50 pixels, whereas those same speckle sizes were found in approximately 85% of the speckle pattern at 80 PSI. With images of the patterns at different PSI (Fig.1c) we can visually observe smaller particle sizes as PSI is increased.

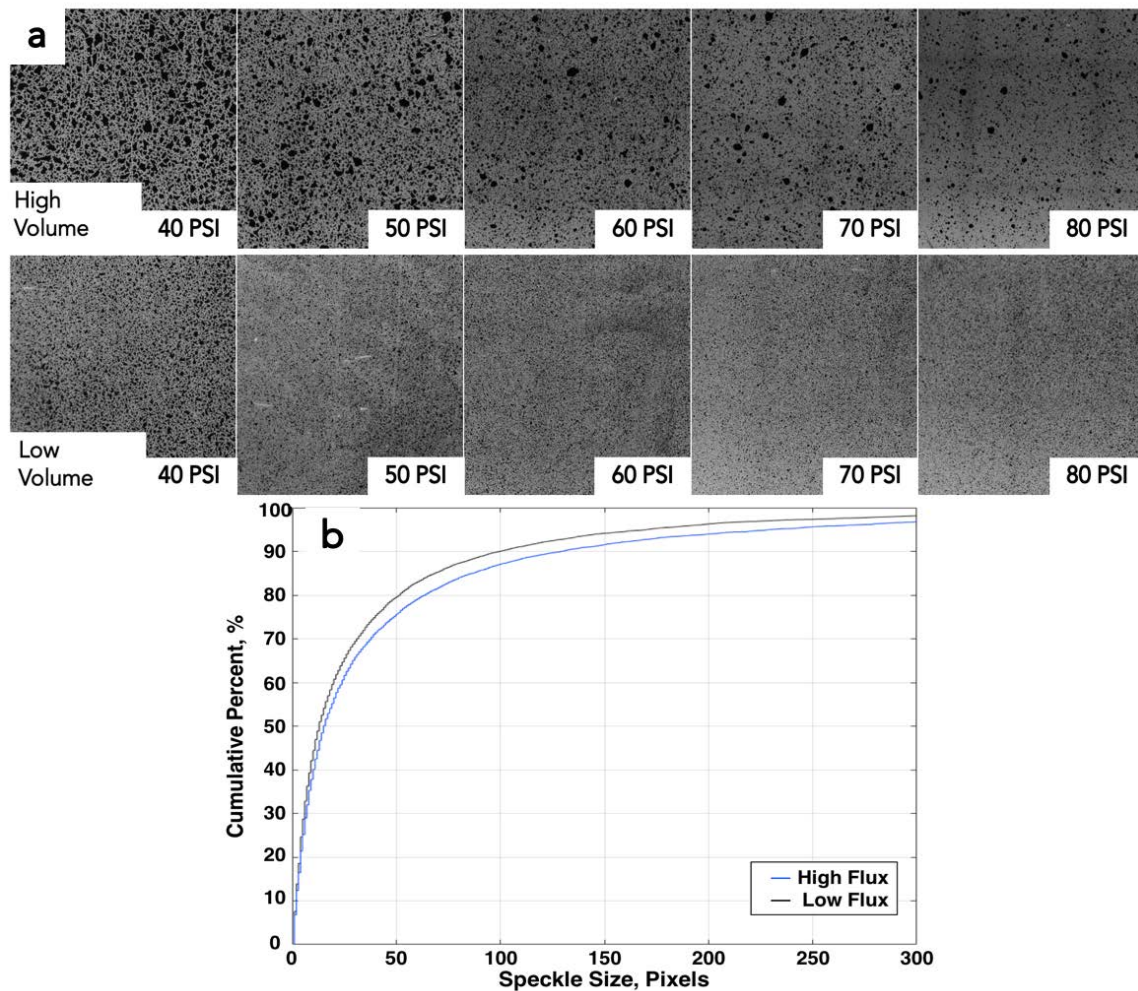


**Figure 2.** (a) Speckle Pattern Comparison of different air pressure rates at High vs. Low Ink Volume. (b) Cumulative Distribution of Speckle patterns of High and Low Ink Flow at the same PSI Rate (70 PSI).

**Flux Rates** After observing the images of the Speckle Patterns at different PSI rates (Fig. 1c), we visually noticed that at higher PSI, lower densities of speckles per area were found. This could result in large errors measured by DIC at small interrogation cells.

Because of this, we decided to perform tests of different PSI at low ink flow. By visually comparing the images of speckle patterns at different PSI of high vs low ink flow (Fig.2a) we can conclude that the patterns applied at low ink flow contain a low number of large particles. Such particles can render the DIC method inaccurate near regions of high strain gradient such as near a crack tip. A cumulative percentage chart (Fig.2b) reveals that the speckle distribution of the pattern of low vs. high ink flow is similar. We suggest that at a lower ink flow, the particle distribution is similar to that of patterns applied with high ink flow, but there are fewer large particles and higher densities of speckles can be observed.

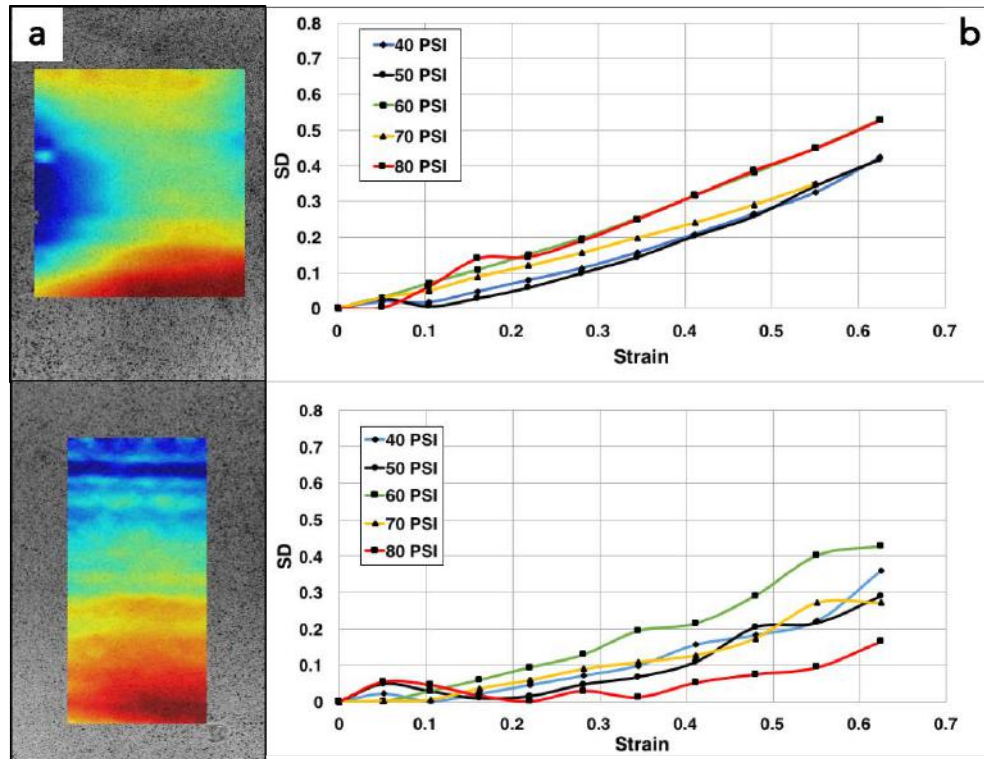


**Figure 3.** (a) Different Regions of Interest Images. (b) Error analysis of different Regions of interest (Subset Radius used: 40 pixels).

**Shannon Entropy and Mean Intensity Gradient** The Shannon Entropy and Mean Intensity Gradient were calculated for the airbrush ink after being implemented on the hydrogel. Minimal differences were found in both calculations for all the speckle patterns (Table.1a). Equally important, the results obtained from the calculations did not indicate large distinctions between the patterns at different PSI rates. This means that neither the calculations of Shannon entropy nor the mean intensity gradient provide useful measures the quality of a proper speckle pattern for Digital Image Correlation at large deformations. Moreover, the morphological assessment did show differences in the patterns, and as a result we conclude that speckle patterns with particles sizes ranging from 0 to 50 pixels averaging from 80 to 90% in the patterns result in more accurate DIC measurements.

**Region of Interest Test** After taking all the images, DIC experiments were performed using two different regions of interest of the same interrogation cell size (40 pixels). The first ROI was a square measuring approximately 10x10mm. The second ROI measured approximately 6mm wide and 12mm long (Fig.3a). After error analysis, the 6 by 12mm ROI resulted in lower standard deviations (Fig.3b). Consequently, that same region of interest was the one used for the subset size tests. Average strain values compared to the imposed strains of different ROIs are found in Supplementary Figure 3.

**Subset Size Error Analysis** Digital Image Correlation was performed using the same ink and same three patterns but changing the interrogation cell size. At different subset radii (10, 40, 120 pixels), the error analysis was performed by comparing the deviation of the imposed strain and the measured strains of the DIC tests. Different visual appearances are seen in the sample images of the what was

observed at the different subset radii (Fig.4a). We noticed that the Kohinoor ink at the highest air pressure (80 PSI) was the most accurate for all the different interrogation cells (Fig.4b). This could be because at larger interrogation cells, more particles can be observed if compared to the lower PSI patterns. Patterns at pressures in between 40 and 80 PSI (50,60,70 PSI) performed similarly at all the different interrogation cell sizes. Average strain values compared to the imposed strains of different subset sizes are found in Supplementary Figure 4.

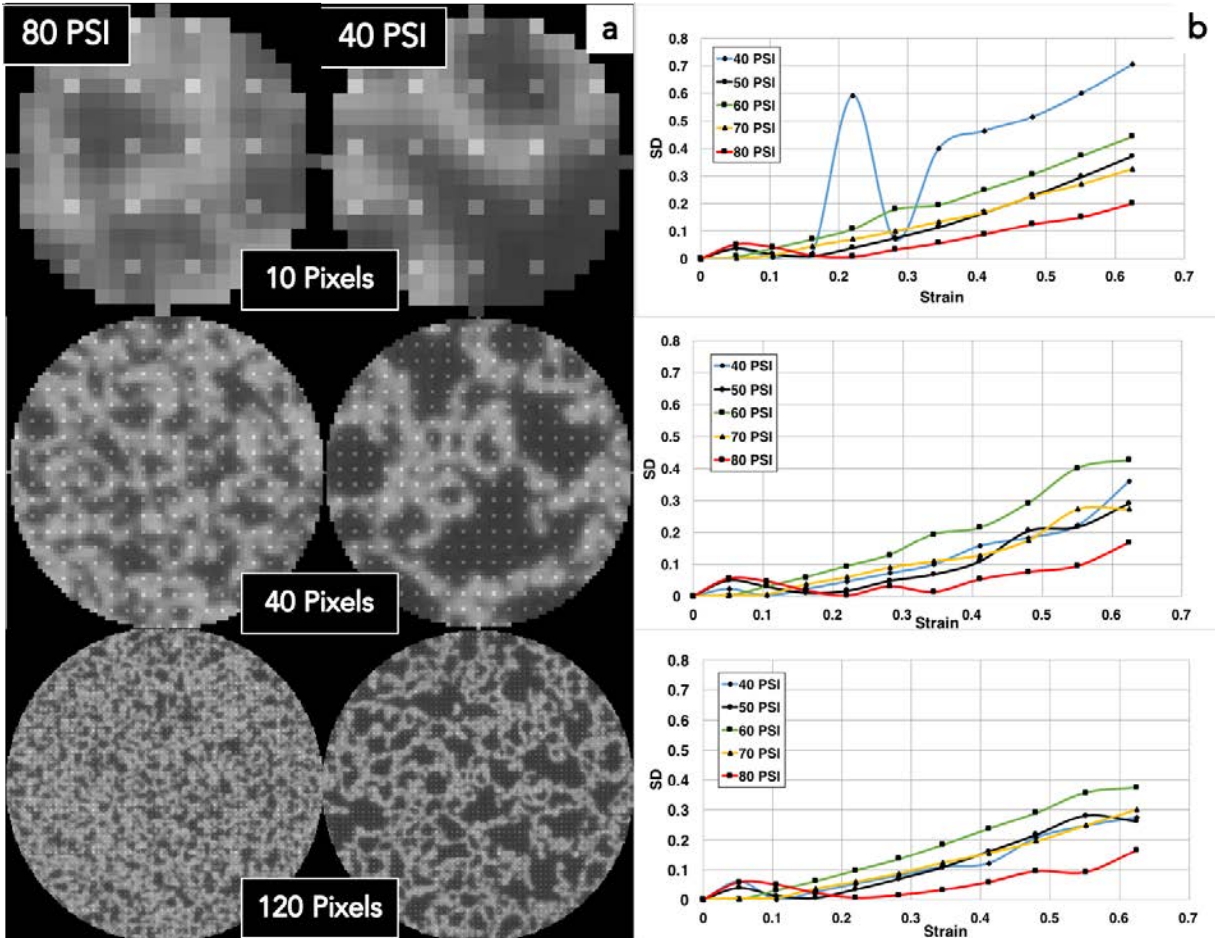


**Figure 4.** (a) Visual appearance of speckle patterns at different subset radii. (b) Error analysis at different subset radii.

**Discussion** Relationships between air pressure rates and speckle sizes in the patterns were found and demonstrated via the morphological assessment tests. At higher pressure rates, smaller speckle distributions were detected. Secondly, lower ink flow rates resulted in higher particle densities per area but similar particle distributions.

Comparison of the Shannon Entropies and the Mean Intensity Gradients of the patterns from different air pressures to the error analysis of the DIC, demonstrated no relation or tendency between these measures and the accuracy of the DIC measurements. Equally important, via morphological assessments we also did not find a relationship between the accuracy of a speckle pattern and the subset size selection. We conclude that even though the morphological assessments noticed

differences in all the patterns, it did not help us conclude a tendency between the accuracy of a pattern for DIC and the assessment.

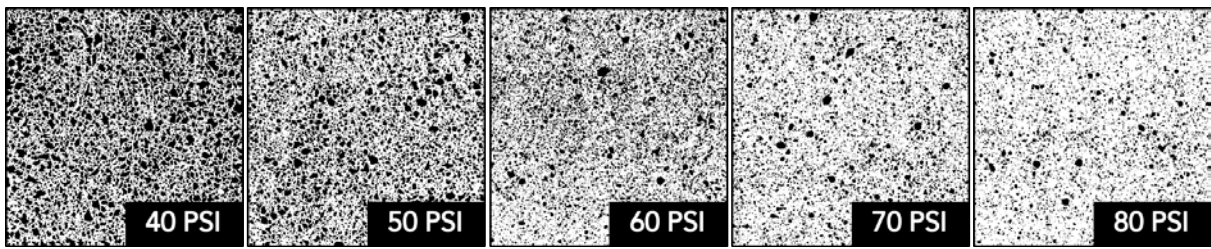
For Digital Image Correlation tests on hydrogels, we suggest that the Kohinor Ink or is an appropriate airbrush ink for Digital Image Correlation. Additionally, patterns sprayed at higher air pressures at low ink volumes proved to be more accurate at different interrogation cells. The average error of the speckle patterns implemented at 80 PSI analyzed using a 40-pixel subset was 5.8%.

**Acknowledgments** For the development of this project it is important to thank the Cornell Center of Materials Research REU Program. This work was primarily supported by the Cornell Center for Materials Research with funding from the NSF MRSEC program (DMR-1120296).

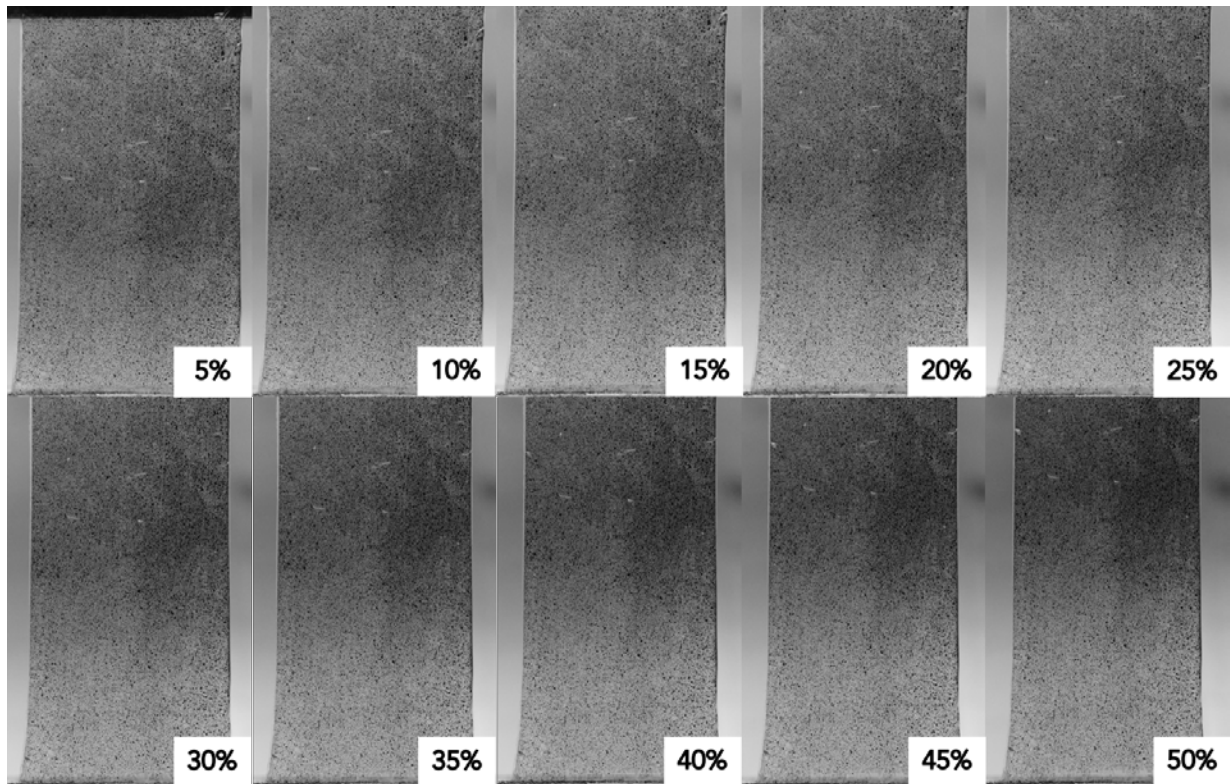
## References

1. Triconnet K, Derrien K, Hild F, Baptiste D. Parameter choice for optimized digital image correlation. *Opt Lasers Eng* 2009;47(6):728–37.
2. Yaofeng S, Pang J. Study of optimal subset size in digital image correlation of speckle pattern images. *Opt Lasers Eng* 2007;45(9):967–74.
3. Y.Q. Wang, M.A. Sutton, H.A. Bruck, H.W. Schreier Quantitative error assessment in pattern matching: effects of intensity pattern noise, interpolation, strain and image contrast on motion measurements, *Strain*, 45 (2009), pp. 160-178
4. Barranger Y, Doumalin P, Dupré JC, Germaneau A. Digital image correlation accuracy: influence of kind of speckle and recording setup. *EPJ Web Conf* 2010; 6:31002.
5. Crammond, G, Boyd, S.W., Dulieu-Barton, J.M. Speckle pattern quality assessment for digital image correlation. *Opt Lasers Eng* 2013; 51:1368–1378
6. Pan B, Lu Z, Xie H. Mean intensity gradient: an effective global parameter for quality assessment of the speckle patterns used in digital image correlation. *Opt Lasers Eng* 2010;48(4):469–77.
7. Hua T, Xie H, Wang S, Hu Z, Chen P, Zhang Q. Evaluation of the quality of a speckle pattern in the digital image correlation method by mean subset fluctuation. *Opt Lasers Eng* 2011;43(1):9–13.
8. [11] Lecompte D, Smits A, Bossuyt S, Sol H, Vantomme J, Van Hemelrijck D, et al. Quality assessment of speckle patterns for digital image correlation. *Opt Lasers Eng*. 2006;44(11):1132–45.
9. Mayumi, K., Marcellan, A., Ducouret, G., Creton, C., Narita, T. Stress–Strain Relationship of Highly Stretchable Dual Cross-Link Gels: Separability of Strain and Time Effect. *ACS Macro Letters* 2013; 2:1065-1068.

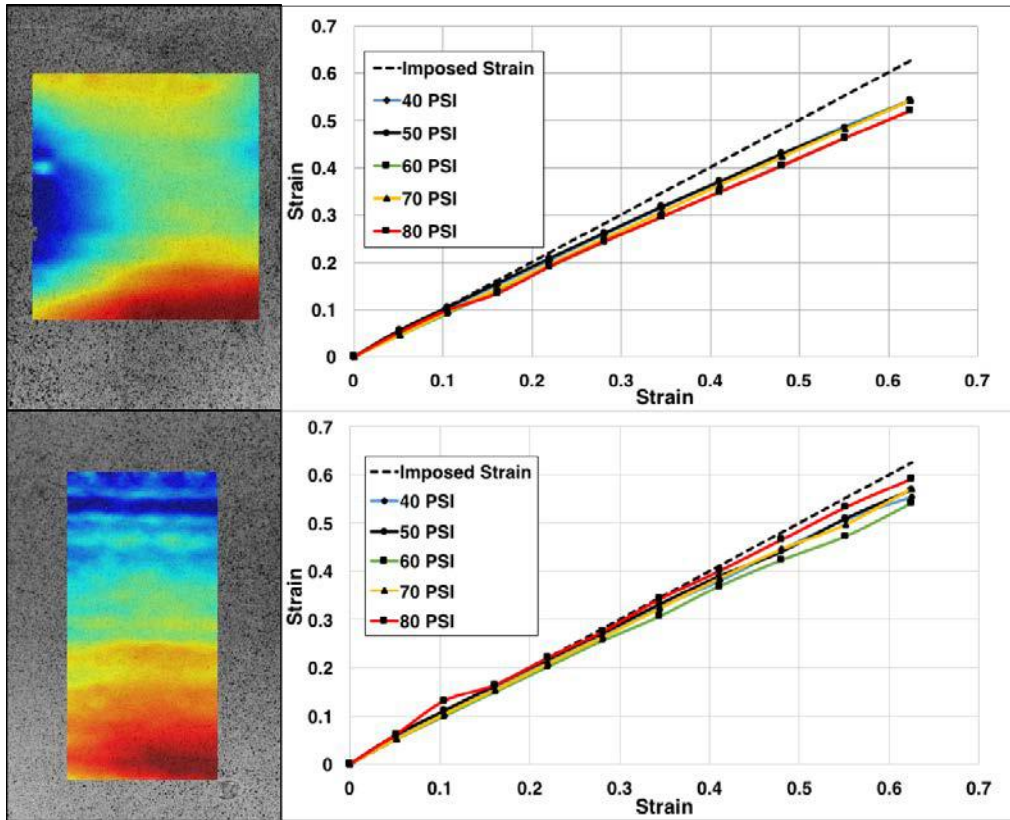
## Supplementary Figures



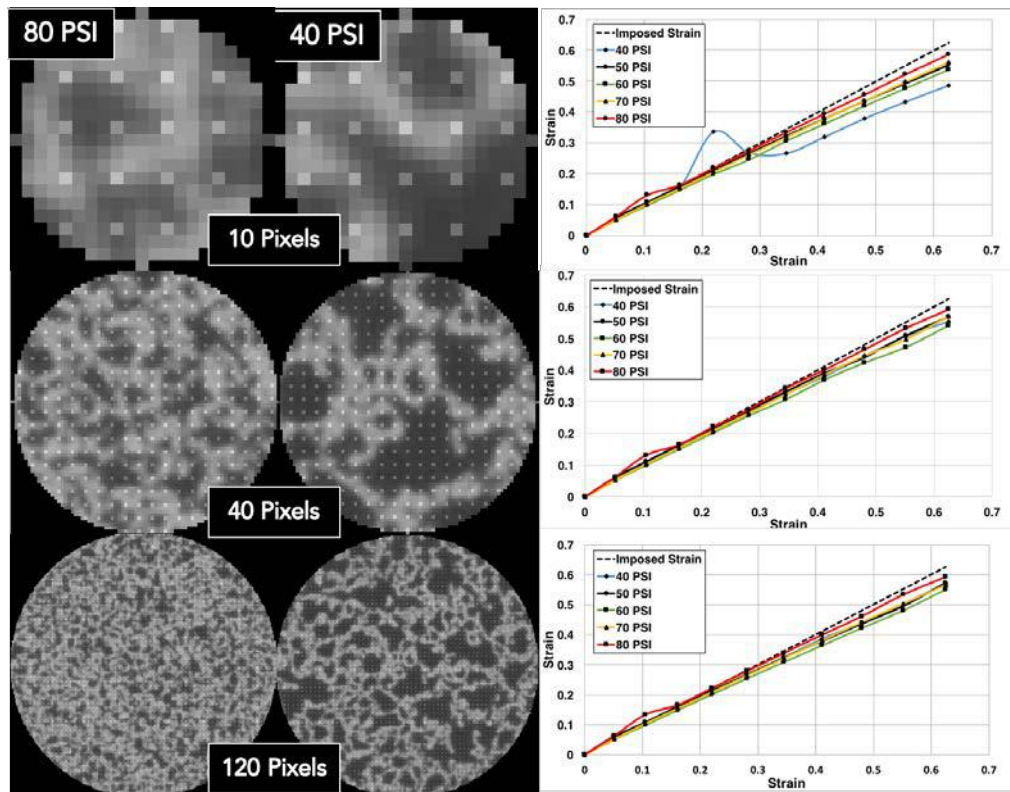
Supplementary Figure 1. Black and White Utilizing ImageJ's threshold for the Morphological Assessment Tests



Supplementary Figure 2. DIC Images taken every 5% strain.



Supplementary Figure 3. Average Strain vs. Imposed Strain of Speckle patterns with Different ROIs.

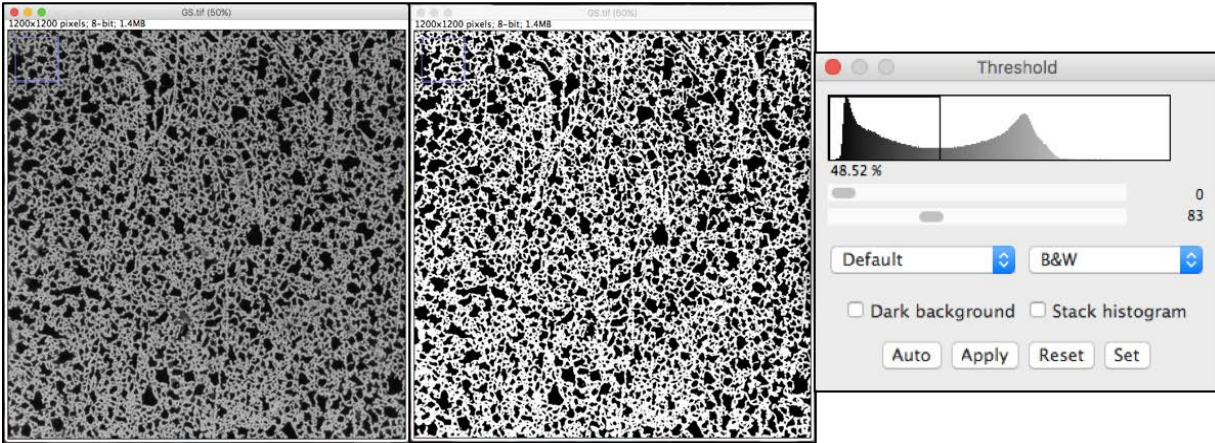


Supplementary Figure 4. Average Strain vs. Imposed Strain of Speckle patterns with Interrogation Cell Sizes.

Step 1. Open the image of interest. Crop the portion of the image as desired for analysis.

Step 2. Go to Image>Adjust>Threshold  
ImageJ will automatically turn the image into B&W.

If further adjustments need to be done, manually adjust the threshold on the window that will appear.



Supplementary Figure 5. Instructions on converting images into B&W utilizing ImageJ's Threshold.

# Computational optimization of PV materials

Scott A. Lopez, dept. of Chemistry, West Virginia University  
Eliad Peretz, Rees Chang, Hanrath Energy Lab, Cornell University

**Abstract- The morphology of amorphous silicon (a-Si) was computationally optimized to make a slimmer, more affordable, and efficient solar cell. A finite-difference-time-domain (FDTD) MEEP was used to model electromagnetic waves (EM) propagating through a a-Si media. Introducing a random-hole morphology into the simulation yielded an increase in absorption compared to a no-holed cell. A range of hole radii and hole quantity (filling fraction) of 100-175nm and 0.2-0.4ff respectively was optimized via genetic algorithm. The algorithm is not yet fully functional but has been integrated with MEEP.**

## I. Introduction

Alternative energy sources have become more prevalent due to sustainable economic and environmental advancements. Solar cell technology is a pre-existing area of alternative energy, however, interest in the field continues to expand. In recent years, a techno-economic analysis demonstrated that photovoltaic (PV) solar cells can maintain the standard 20% efficiency after a decrease in silicon thickness from 180um to 20nm. This enables the total cost of the solar cell to be 47% cheaper than the thicker device<sup>1-5</sup>. To make this more efficient a heterojunction solar cell with back side contact could be implemented as seen in figure 1.

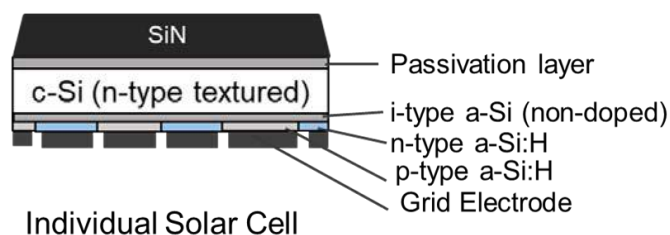


Figure 1: Above is a simplified diagram of a heterojunction PV solar cell with back side contact. Energy from a source in the form of a photon encounters the textured solar cell. Photon energy is converted into photocurrent in the form of excited electrons at the p-n

junction through the c-Si n-type layer. These electrons then migrate into a load.

This type of solar cell has many benefits such as alternating n-type and p-type a-Si at the bottom enables the photons to be readily absorbed. The fabrication process allows the c-Si to be easily textured while being supported by the backside grid electrode. It has been previously reported that this setup with a c-Si n-type layer of ~150nm can output more than 25% solar cell efficiency<sup>6</sup>. Because of the heterojunction solar cell design its stabilization makes it possible to combine the two previously stated theories of to make a thin silicon layer for economic and solar cell efficiency.

The project of ‘Computer Optimization and 3D Printing of Quantum Dot’ in the Hanrath Energy Lab combines the key aspects PV solar cells in three sub projects: computational optimization, material synthesis, and structural fabrication. These methods could be applied to the previously stated techniques. Computational optimization holds a unique advantage in that it enables the researcher to get into the correct range of parameters to test before obtaining real-world data.

Altering the morphology of thin c-Si could increase photon absorption and thus solar cell efficiency while maintaining and or improving material absorption and spectral accuracy. The morphology of thin a-Si films was computationally optimized in order to determine the maximum absorption of a material or obtain a specific spectra based on morphology.

To simulate the environment and solar cell interactions a free finite-difference time-domain (FDTD) called MEEP was used. MEEP can efficiently simulate electromagnetic (EM) waves interacting with a media of specific shapes and properties. A study testing various morphologies of a-Si in MEEP demonstrated that a disordered hole pattern increases in absorption by a factor of 4.3

compared to a flat, no holed a-Si slab<sup>7,8</sup>. Influential parameters of this study included the quantity of holes (filling fraction), hole radii, and the corresponding x/y location on the media (figure 2). The project of computational optimization of PV materials was geared towards the implementation of genetic algorithms (GA) that utilize the previously made MEEP program for modeling a-Si. Focusing on similar parameters the GA would optimize the absorption and residual matching of a spectra based on morphological structure.

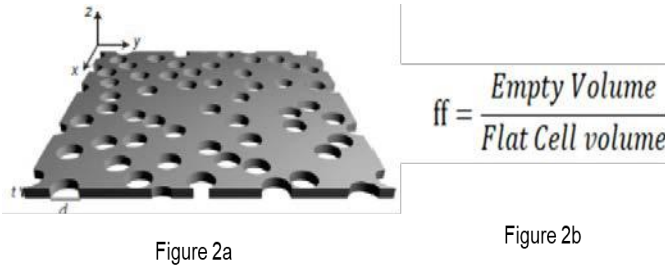


Figure 2: The image to the left is a model describing the various parameters of introducing a hole morphology into the MEEP simulation. X/Y coordinates of the holes are seen in the upper left corner axis while the thickness and hole radii are at the bottom left. Figure 2b shows how the ‘quantity of holes’ or ‘filling fraction’ are calculated.

## II. Methodology of Genetic Algorithm

### A. Setting the framework

MEEP was installed on Bash on Ubuntu on Windows with an earlier framework pulled from a previous contributor’s github. Parallel MEEP was used and supports distributed-memory parallelism using MPI (message passing interface) which enables the MEEP package to run efficiently.

An empty cell of  $0.1\mu\text{m} \times 2.6\mu\text{m} \times 2.6\mu\text{m}$  was first simulated in MEEP to act as a transmission and reflection reference. Later these values will be divided into the transmissions and reflections of the a-Si cell to get the true transmission and reflection of the a-Si cell for specific wavelengths and frequencies.

A literature review was conducted to discover how common a 100nm thick a-Si slab was experimentally and or computationally characterized. A MEEP simulation of a a-Si slab of  $0.1\mu\text{m} \times 2.6\mu\text{m} \times 2.6\mu\text{m}$  was ran with no holes to verify the accuracy of MEEP and determine the trend of photon absorption as the material thickened from 100-600nm for wavelengths 280 – 1300 nm. The meep-openmpi was used to call MEEP to run a

simulation calling on the absorption\_random\_2D\_photonic.ctd directory. This directory contains the contents MEEP needs to run a simulation on a-Si with the basic material characteristics outlined. The fluxes, reflectance, and transmission values are then used for the ‘find absorption’ python file which calculates the absorbance and average absorbance of the material based on the empty fluxes.

A 3D plot (F(ff,radius)) was also plotted for radii from 25-200nm (every 25 nm) and an ff range of 0.2 – 0.5 (every 0.1 ff). The same procedure as before was ran except the radii and ff range was inputted.

### B. Generating the morphologies

Randomly generated holes are put into the a-Si media via a python script. The lateral size of the a-Si cell is defined as the empty cell was. Holes are defined by their x, y locations and their associated radii. Together the x, y, radii defines each holes characteristic and ultimately the overall morphology of the cell. Collectively these parameters are saved in a txt files called ‘rodpos.txt’ for each morphology. The rodpos.txt files are interchangeably referenced as DNA since an evolutionary algorithm is used as the optimization tool.

One boundary of the hole generator is that the hole must stay within the filling fraction set from 0.2-0.4. The other boundary is that the hole radii should be between 100 and 200nm. Once the radii are made the x and y locations are set to not overlap. If the radii, x, and y parameters are within the overlap boundary limits then the hole is made and the entire holeset it saved it the ropdpos.txt as ‘parent’ DNA. As of now the algorithm is designed to output 4 parent DNA rodpos.txt files. These 4 parent DNA are saved, but copied twice; once for crossover and once for mutation.

### C. Crossover and Mutation

The crossover and mutation scripts are both python files. Crossing over of DNA enables the rodpos.txt parameters to approach a local min or max.. The process of the crossover takes information one DNA and randomly gives it to another DNA. While another DNA strand randomly will fill the vacancy in the DNA strand that just donated. For this algorithm the crossovers are made by splitting the DNA into two lists down the middle. The list of the 4 parent DNA are now 8 ‘half’ lists of the original DNA and then randomly combined with a

unique pairings. The new crossover DNA is then checked if it is the filling fraction 0.2-0.4 range. If below the 0.2 range a non-mutate random hole is added through the same process in the random hole generator. The DNA is checked again and if the filling fraction is above 0.4 then a random hole in the DNA is removed. The final crossover DNA saved as a new crossover rodpos.txt file while the original is saved still as the parent DNA.

Getting out of a local max or min mutations can introduce variability into the DNA. Five random holes and its parameters from the parent DNA are picked to be mutated within  $\pm 10\%$  of its original value. If the new mutant DNA overlaps another hole than the mutant hole is removed and another hole is randomly mutated. Once a mutated hole does not overlap, the filling fraction is checked and edited as the crossover was. The mutated lists are saved as mutated DNA while the parents are unchanged.

#### D. MEEP on textured material

The MEEP simulation runs once again with meep-openmpi but now it calls from the 4 parent, 4 crossover, and 4 mutant DNA on findAbsorption.ctf to get the each DNA's material parameters that defines the a-Si cell. The outputting h5 file contains the tfluxes and r fluxes needed to calculate the absorption of the associated DNA. From here the information of the DNA can go to find the absorption spectra of each DNA candidate, or, if the residual absorption can be found to who how closely it matches a pre-determined spectra.

#### E. Absorption fitness, selection and generation cycle

Find absorption is a python file that obtains the freqs and the fluxes from the empty and the DNA file being evaluated. The absorption and average absorption is found by  $a = 1 - t + r$  and average absorptions = absorptions sum / absorption count where  $t = tflux(DNA)/emptytflux$  and  $r = rflux(DNA)/emptyrflux$ . This is done for all 12 DNA files and the previous information of the rodpos.txt files for each DNA is saved. Optimization of the structures is performed by the selectNextParent python file that selects the best 4 DNA. The best 4 have the highest average absorption value. Next, these 4 DNA are now marked (and saved) as the most-fit of this generation and are parents of the following optimization

algorithm. The process repeats for the desired generational count.

#### E. Residual fitness, selection and generation cycle

Find residuals obtains the freqs and the fluxes from the empty and the DNA file being evaluated. The absorption is found just as in the find absorption method above. Using the calculated absorptions the residual was found by  $R = |Abs_{observed}| - |Abs_{target}|$ . Selection of the best residuals was done by choosing the best 4 spectra, which was the DNA with the lowest residual value. Next, these 4 DNA are now marked (and saved) as the winners of this generation and are parents of the following optimization algorithm. The process repeats for the desired generational count.

### III. Results

#### A. MEEP material verification

A thickness plot to test the accuracy of the MEEP simulation was based on the MEEP spectra in comparison to previously done work. The MEEP simulation of a a-Si slab of  $0.1\mu\text{m} \times 2.6\mu\text{m} \times 2.6\mu\text{m}$  was ran with no holes to verify the accuracy of MEEP, and determine the trend of photon absorption as the material thickened from 100-600nm for wavelengths from  $\sim 280 - 1300$  nm seen in figure 3. The trend observed shows that as the thickness increases so does the frequency and energy.

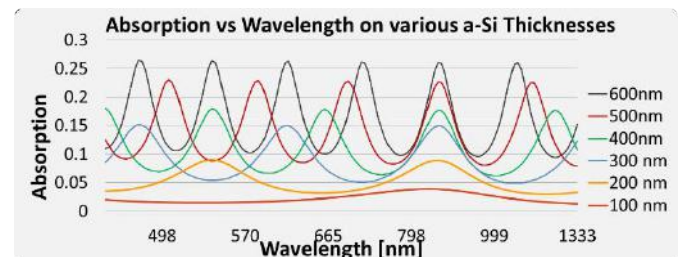


Figure 3: The above is a MEEP simulation of a a-Si slab of  $0.1\mu\text{m} \times 2.6\mu\text{m} \times 2.6\mu\text{m}$  with thicknesses from 100-600nm. The rough a-Si indirect bandgap is seen at  $\sim 820$ nm wavelength.

#### B. 3D plot ( $F(ff, radius)$ )

Trends of the filling fraction vs radius vs the corresponding F value when simulated in MEEP had to be efficiently mapped out before GA implementation. This was because the GA did not have a range of parameters to optimize yet. Mapping out the parameters and their associated F values also gave an idea of the type of output the GA should

have once it was made. The trends can be seen in figure 4.

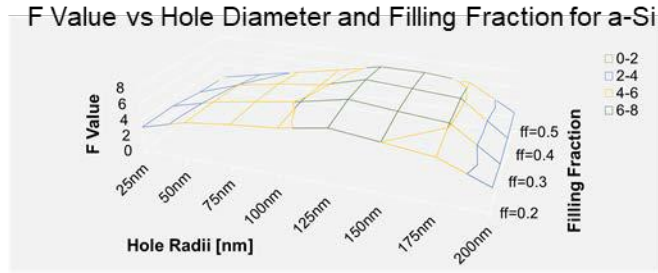


Figure 4 is a 3D plot of F value vs hole diameter and filling fraction for a-Si. The trend shows a peak range of F value between ~100-175nm and ff between 0.2-0.4.

### C. Genetic Algorithms

As described in the methods section two genetic algorithms were made, absorption and residual spectra. Each of the algorithms are designed to optimize morphology of the a-Si to either obtain the highest absorption or the lowest residual. The GA's were made in the language python and implemented into the linux system with MEEP. Both of the absorption and residual GA's were trouble shooted for bugs and script errors by running minor simulations in MEEP and on an IDE called pycharm. The absorption GA was ran on the desktop of Eliad Peretz in the Hanrath Group. One entire generation of the absorption GA was successfully executed. The selection process for the next generation was functioning properly until an error occurred; the residual spectra ran into a similar problem.

### IV. Discussion

The thickness model shows that if you take the average absorption as the material thickens, a trend arises that corresponds to the beginning portion of the beer-lamberts law curve. The a-Si indirect bandgap at around the wavelength of ~820nm agrees with literature computationally<sup>7</sup>. Experimental literature was extremely difficult to find for 100nm flat, a-Si. This was because of the fact that most solar cells use and characterize c-Si rather than a-Si. If a-Si was being observed it was never without layers, textures, and or nanoparticles.

The trends observed in the 3D (F(ff(radius))) plot demonstrates the trend of filling fraction and hole diameter in relation to the F value when being simulated in the MEEP environment. This gave general parameter ranges to optimize with the GA as well as the corresponding F values. To get accurate representation of the relationship a larger parameter area should be tested for a longer duration of time.

Only one generation of the absorption GA was successfully computed before the frequencies became irregular for the second generation. Similar results are occurring for the residual GA as well. The desktop that is having the simulation ran on it is having hardware issues with its core processors. This is still being troubleshot.

### VI. Conclusion

The implementation of genetic algorithms that are implemented with MEEP to optimize the absorption and residual matching of a spectra based on morphological structure was successfully done. The GA was made and it shows the optimized morphologies generated for the next generation. Only one generation was ran through its entirety, the other had its parents optimally selected. The trend and ultimate effectiveness of the algorithms are currently unclear as they are still undergoing its troubleshooting and data collection stage.

The MEEP package was verified to properly model EM waves by comparing its absorption output for various a-Si thickness to literature. Obtaining a range of parameters to input into the GA was performed. The optimal morphology outputted by the GA based on F values from this trend is still incomplete.

Future work regarding evolutionary algorithms to optimize material morphology is ongoing. In the upcoming weeks the GA will start to improve its crossover, mutation, and selection process. Having the current density of the material was investigated to not only help analyze data but also act as a spatial selection. New materials, layers, and nanoparticles are to be introduced to the simulation as well.

### Acknowledgements

-I would like to thank my fantastic project group of Rees Chang and Eliad Peretz.

-The Hanrath Group for being an amazing lab full of - even better researchers and people.

-NSF

-Direct CCMR Funding, primary support

-Direct CCMR Funding, partial support

-Use of the CCMR Facilities

-Support through other CCMR grants

-Acknowledging an IGERT Fellowship

-CRYO-FIB/SEM work

-Titan Themis TEM/STEM work

#### *REFERENCES*

- [1] Zhang, Y., Strokes, N., Jia, B., Fan, S., & Gu, M., Scientific reports, 4, 4939, 2014
- [2] Bakke, J. R., Pickrahn, K. L., Brennan, T. P., & Bent, S. F., Nanoscale, 3(9), 3482-35-08, 2011
- [3] Olson, C., Geerlings, B., Goris, M. J A. A., Bennett, I., & Clyncke, J., EU PVSEC, Vol. 30, 4629-33,2013
- [4] Goddrich, A., Woodhouse, M., etc., Solar Energy Materials and Solar Cells, 114, 110-125, 2013
- [5] Choi, S., Jang, B., Kim, J., Song, H., Baek, T., & Han, M, Solar Energy, 122, 1170-1179, 2015
- [6] Masuko, K., Shigematsu M., Hashiguchi D., etc., IEEE Journal of Photovoltaics, Vol 4. 2014
- [7] K. Vynck, M. Burrese, F. Riboli, D. Wiersma “photon management in two-dimensional disordered media” Nature Materials (2017).
- [8] F. Pratesi, M. Burrese, F. Riboli, K. Vynck, D. Wiersma. “Disordered photonic structures for light harvesting in solar cells.” OSA Publishing (2013).

# Shaking Things Up: Using Sound Waves to De-Thicken Colloidal Suspensions

Kemper Ludlow  
Cornell University  
9 August 2017

## Abstract

*A new method of using acoustic waves to reduce the viscosity of shear-thickening colloidal suspensions is presented. In the presence of an acoustic wave, a dense suspension of silica particles showed up to 17% reduction in pressure needed to drive the fluid at comparable flow rates. This method has applications in reducing energy cost for industries which require transport of dense suspensions at high flow rates.*

## Introduction

Shear thickening colloidal suspensions become increasingly viscous under increasing strain rates. This leads to a higher energy cost for applications requiring pipe flow of dense suspensions, as well as complications such as clogging. In order to de-thicken suspensions, most industrial applications rely on treating the surface of particles beforehand. A viable method for de-thickening untreated suspensions in pipe flow has yet to be presented.

Recent research has shown that particles come into contact and form "force chains" during shear thickening. These contact forces scale up with increasing shear rate. To break the force chains, an orthogonal flow perturbation could be applied. Although these experiments were conducted for shear flow, it has been theorized that a similar effect could be obtained in pipe flow by applying an acoustic wave.

In this experiment, the flow of a shear-thickening colloidal suspension in a capillary was observed. Flow was characterized by comparing the flow rate,  $Q$  to the change in pressure,  $\Delta P$  required to drive the fluid. An acoustic wave was then applied via a piezoelectric device attached to the capillary, and compared to the control data.

## Experiment

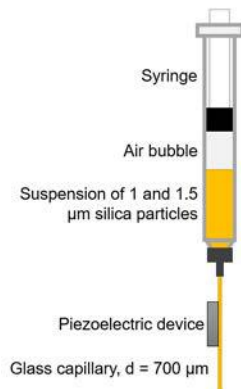


Figure 1: Diagram of experimental setup. The syringe was driven at a constant flow rate, and measurements of pressure and flow rate were taken by tracking the volume of the internal air bubble and position of fluid meniscus, respectively.

A bidisperse suspension of 1.0 and 1.5  $\mu\text{m}$  particles with volume fraction  $\phi \approx 0.5$  was flowed through a glass capillary via a 1 mL syringe. The syringe contained an air bubble between the plunger and the fluid meniscus, with an initial air bubble volume of approximately 0.5 mL. For each measurement, a video of the syringe was taken. Edge detection was used to identify the position of the fluid meniscus in each frame, and a Savitzky-Golay fit was used to obtain the flow rate of the fluid. To compute the instantaneous pressure within the syringe, the volume of the air bubble in each frame was measured by subtracting the position of the fluid meniscus from the position of the tip of the syringe plunger. The ideal gas law was then applied to find the corresponding change in pressure. The lab was assumed to have an ambient pressure of 1 atm.

To apply the acoustic wave, a piezoelectric device attached to the capillary was driven at its resonant frequency of 1.5 MHz and a peak-to-peak voltage of 12 V. The resonant frequency of the piezo is approximately equal to the resonant frequency of the capillary.

Experiments were also run using pure glycerol to confirm that the experimental setup gave the expected results for a Newtonian fluid.

## Results

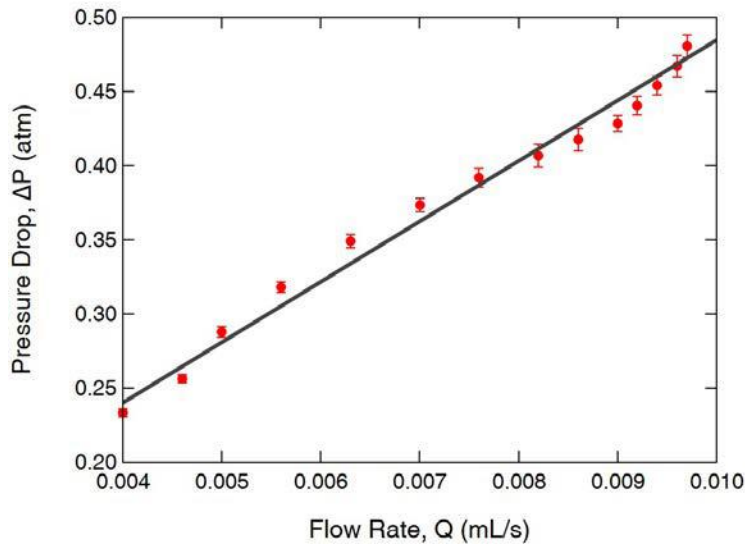


Figure 2: Pressure drop vs. flow rate of pure glycerol. The resulting linear fit is  $\Delta P = (0.077 \pm 0.004 \text{ atm}) + (40.8 \pm 0.6 \text{ atm} \cdot \text{s/mL})Q$ . This corresponds to a viscosity of  $\mu = 0.609 \pm 0.009 \text{ Pa} \cdot \text{s}$ .

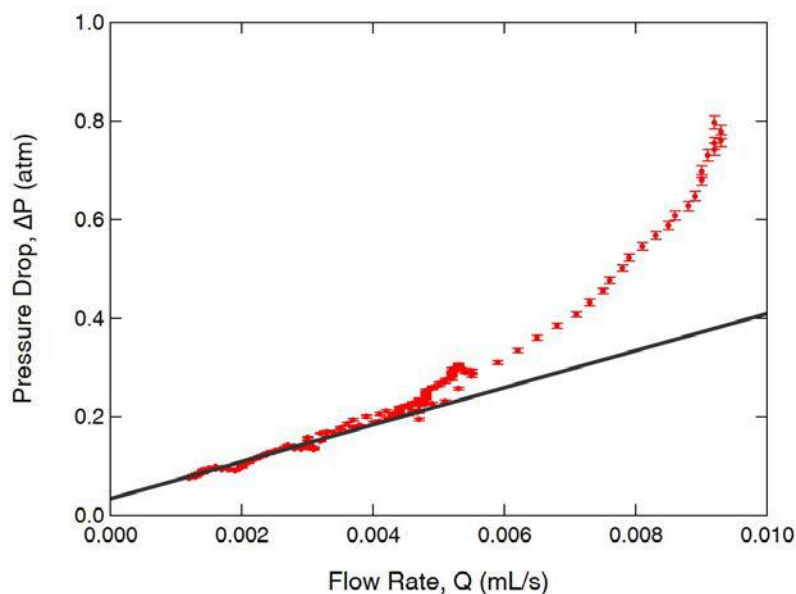


Figure 3: Pressure drop vs. flow rate for the silica suspension. A linear fit has been plotted to make the nonlinearity of the data more obvious.

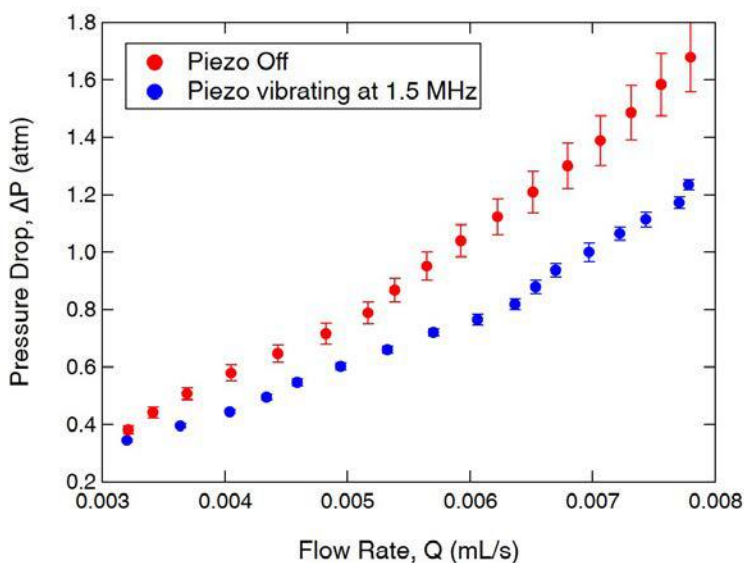


Figure 4: Pressure drop vs. flow rate for the silica suspension, comparing results with the piezoelectric device on and off at high flow rates. While the piezoelectric device is on, the fluid requires less pressure to drive at the same flow rates as the control data.

## Discussion

For a Newtonian fluid undergoing Poiseuille flow, we expect a linear relationship between  $\Delta P$  and  $Q$ , with a slope corresponding to the viscosity. The experimental results for pure

glycerol, show in fig 2, are consistent with this. The slope of the fit yields a viscosity of  $\mu = 0.609 \text{ Pa} \cdot \text{s}$ . This is lower than the expected viscosity, but the discrepancy is most likely due to the hygroscopic glycerol absorbing water from the air prior to and during the experiment.

For the colloidal suspension, the relationship between  $\Delta P$  and  $Q$  (shown in fig 3) is notably nonlinear. The upward curvature is characteristic of a shear thickening fluid, which has increasing viscosity at higher shear rates.

The effect of the acoustic wave is shown in fig 4. The fluid still shows some upward curvature and shear thickening in the presence of an acoustic wave; however, it requires less pressure to achieve the same flow rates, and the slope of the data is less steep, indicating a lower viscosity. This effect becomes larger at higher flow rates, with a pressure reduction of approximately 17% at the highest flow rate measured.

## Conclusion

A new method for reducing shear thickening in pressure-driven flow has been shown. By applying an acoustic wave to a colloidal suspension as it flowed through a capillary, the pressure needed to drive the fluid was reduced. This result could have applications within many industries which require the flow of dense suspensions, including concrete and 3D printing inks. Further investigation of the effect of varying frequency and voltage would be useful to fully characterize the technique.

# Synthesis and Analysis of Antibacterial Oligothioetheramides (AOTs)

Angela Pacherille

**Abstract** - Novel antibiotics are needed to combat the growing problem of antibiotic resistance. Previously, a library of antibacterial oligothioetheramides (AOTs) made with the guanidine monomer and propanedithiol has shown antibacterial activity. However, cytotoxicity has been an issue due to poor selectivity. It was hypothesized that incorporating dipicolyl groups onto the AOT structure with guanidine monomer and propanedithiol would make them more selective towards bacteria. Therefore, a library of AOTs with the amine monomer was synthesized. The AOT, PDT-4Am, was then conjugated with the dipicolyl groups, verifying that the reaction is successful. The AOTs were tested with a MIC assay before conjugation as a reference. PDT-3G and PDT-4Am showed the best activity against *Bacillus subtilis*. Future research will involve conjugating the remaining AOTs and testing their antibacterial activity and cytotoxicity. With more research, AOTs could become possible candidates for antibiotics.

## I. INTRODUCTION

Antibiotic resistance has become a growing threat and continues to worsen as the creation of novel antibiotics decreases and resistance increases. Overuse, inappropriate prescribing, and failure to comply with proper prescription instructions all contribute to antibiotic resistance<sup>1</sup>.

Antimicrobial peptides (AMPs), also called host defense peptides, are currently studied for their potential ability to be used as antibiotics. However, a major drawback of these peptides is their susceptibility to proteolysis which makes them ineffective *in vivo*<sup>2</sup>. A possible solution to this problem is the use of antibacterial oligothioetheramides (AOTs). These synthetic oligomers are designed to mimic the structure of AMPs and therefore have similar characteristics, such as a cationic and hydrophobic nature. These characteristics are believed to contribute to the antibacterial properties of AOTs. Modifying the dithiols and N-allyl acrylamide monomers used in these AOTs has been shown to change both the antibacterial activity and cytotoxicity. Previous research showed that AOTs synthesized with the guanidine monomer showed moderate antibacterial activity but also showed cytotoxicity<sup>3</sup>. Because of this, more selectivity was needed to decrease the cytotoxicity. It is well documented in literature that the dipicolyl functional group, when complexed with zinc, binds the pyrophosphate group of Lipid II on the bacterial cell membrane<sup>4</sup>. Lipid II is only found on the bacterial cell membrane. Adding this functional group to the structure of AOTs made with the guanidine monomer will hopefully increase the selectivity and decrease the cytotoxicity of these AOTs. A library of AOTs incorporating the dipicolyl functional group will be synthesized.

## II. METHODS

### *Synthesis of AOTs*

Synthesis of the AOTs consisted of repeated Thiol-ene and Michael addition reactions on a liquid phase fluororous support followed by a final cleavage reaction which removed the BOC protecting groups and fluororous support (Figure 1).

For the Thiol-ene reaction, fluororous-allylamine was solubilized in methanol for a reaction concentration of 150 mM. 5 equivalents of 1,3-propanedithiol and 0.25 equivalents of 2,2-dimethoxy-2-

phenylacetophenone (DMPA) were added to the solution. This solution was then exposed to three 90 second intervals of UV light. The reaction mixture was purified via fluorous purification<sup>3</sup>.

For the Michael Addition reaction, both 2 equivalents of monomer and 0.1 equivalents of dimethylphenylphosphine (Me<sub>2</sub>PhP) were added to the product solubilized in methanol for a reaction concentration of 100 mM. The reaction was monitored via DTDP assay (Figure S4). DTDP Assay measures the presence of primary thiols. When the curve disappears, that signifies the reaction is complete due to the loss of primary thiols. Once complete, the reaction was purified via fluorous purification.

For the cleavage reaction, the oligomer was solubilized in DCM for a reaction concentration of 5 mM. Trifluoroacetic acid (TFA) was added to the reaction mixture and stirred for 3 hours at room temperature. The product was purified via fluorous purification. HPLC was used to purify product. LC/MS was used to verify product and quantitative NMR was used to quantify the product.

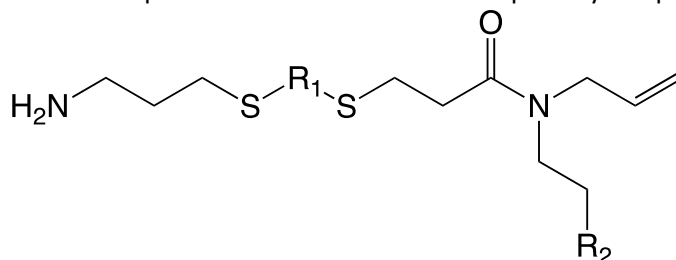


**Figure 1: Structure of AOT.**

#### *Fluorous Purification*

To purify the Thiol-ene product, Michael addition product, and fluorous-allylamine the following protocol was followed. A fluorous silica column was first washed with methanol/water (80:20). The product, which was suspended in methanol, was then pipetted into the column with methanol/water (product crashed out of solution). The vial was washed with a specified amount of methanol/water (80:20). The amount of methanol/water for Thiol-ene reaction washing was determined by 3ml/10mg of fluorous-allylamine used. The amount of methanol/water for Michael addition washing was determined by 5ml/10mg of fluorous-allylamine used. The column was then eluted with methanol to collect the fluorous tagged product. Similar protocol was followed to collect the cleavage product, except product was eluted with methanol/water (80:20).

#### *Synthesis of Fluorous-Allylamine*

To synthesis fluorous-allylamine, THF was added to fluorous BOC-ON for a reaction concentration of 14.74 mM. 1.75 equivalents of allylamine and 3 equivalents of triethylamine (TEA) was then added to solution. The reaction was stirred at room temperature for 3 hours. THF was dried off, and the product was resuspended in methanol. The product was then purified via fluorous purification and verified using NMR.

#### *Synthesis of Guanidine Monomer*

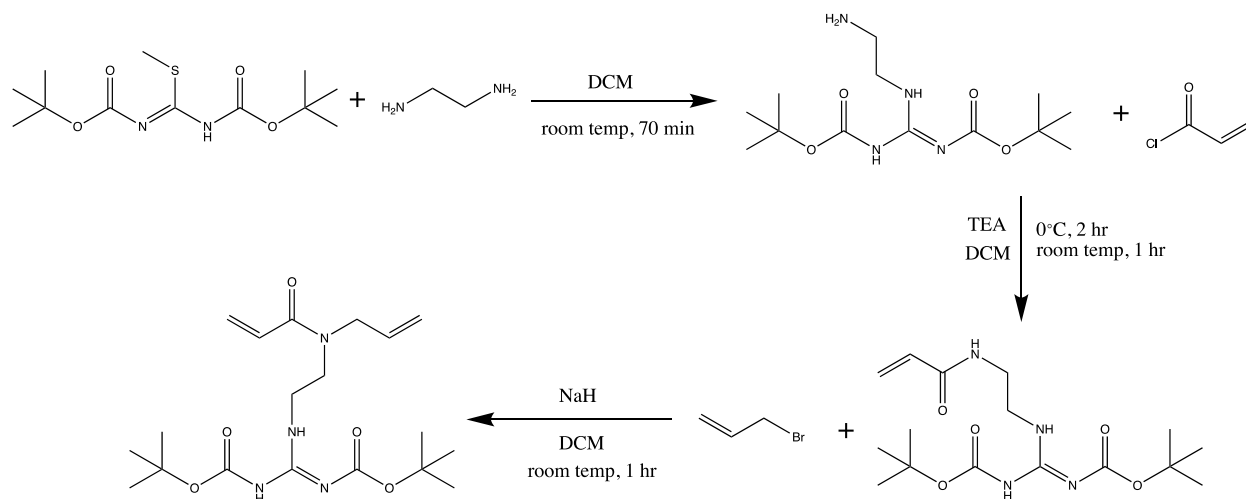


**Figure 2: Reaction scheme of guanidine monomer. There are three reactions to synthesize the guanidine monomer.**

Three reactions were performed to synthesize the guanidine monomer (Figure 2). For the first reaction, 1,3-Di-Boc-2-methylisothiourea was dissolved in dichloromethane (DCM) for a reaction concentration of 450 mM. 2.5 equivalents of ethylenediamine were then added and the reaction was stirred at room temperature for 70 minutes. The organic layer was washed 3x with water and 1x with brine. Excess water was dried with sodium sulfate anhydrous and DCM was removed using nitrogen.

For the second reaction, the product was solubilized in DCM and TEA. The reaction mixture was cooled to 0°C on ice for 15 minutes. Acryloyl chloride was diluted and added to reaction mixture drop wise for 20 minutes. The reaction was stirred on ice for one hour and then stirred for additional hour at room temperature. The reaction mixture was quenched with water and then extracted 3x with DCM. The organic layer was dried with sodium sulfate anhydrous and solvent was removed on the rotavap.

For the third reaction, sodium hydride and the product of the second reaction were solubilized in dry dimethylformamide (DMF) for a final reaction concentration of 200 mM. The product was then added to the sodium hydride and stirred at room temperature for 15 minutes. Allyl bromide was solubilized in dry DMF and added drop wise to the solution via syringe for 10 minutes. The reaction mixture was stirred at room temperature for 1 hour and quenched with water. The reaction mixture was then extracted 3x with DCM and 1x with brine. The organic layer was dried with sodium sulfate anhydrous and purified via silica column flash chromatography. The product was verified using NMR and LC/MS.

#### *Conjugation of Dipicolyl Group to OligoTEAs*

Acetic acid, 50 equivalents of 2-pyridinecarboxaldehyde, and 50 equivalents of sodium cyanoborohydride were added to the PDT-4Am, for a final reaction concentration of 5mM. The reaction was set for 24 hours. Product was verified using LC/MS.

#### *Minimum Inhibitory Concentration (MIC) Assay*

A culture of *B. subtilis* was grown overnight in LB media using a single colony. Bacteria were subcultured the following day and grown to mid-exponential phase. The absorbance at 600nm (OD600) of the subculture was calculated and the subculture was diluted in LB containing 12.5 mg/mL Mg<sup>2+</sup> and 25 mg/mL Ca<sup>2+</sup> to match physiological cation concentration. AOTs stocks were diluted to 1 mM in PBS then added to diluted subculture for a concentration of 50 μM and serially diluted in a 96 well plate. The

plate was incubated overnight at 37 °C and the OD600 was read using a TECAN Infinite M1000 PRO Microplate reader (Männendorf).

#### *Epifluorescence Imaging of B. subtilis*

200  $\mu$ L bacteria solutions were prepared with either 5  $\mu$ M SYTO-9, 25  $\mu$ M dipicolyl diamine with zinc, 25  $\mu$ M ethylenediamine, or 25  $\mu$ M guanidine amine, conjugated with fluorescein (Figure 3). The solutions were then centrifuged to remove excess fluorescein conjugate and washed 4x with HEPES buffer. The bacteria were resuspended in 10  $\mu$ L HEPES buffer/glycerol (1:1) and were then imaged using a Zeiss Upright Epifluorescent Microscope 20X Objective with the eGFP filter. The SYTO-9 sample was diluted by a factor of 2.

### III. RESULTS/DISCUSSION

Fluorescein conjugates were created to determine if certain monomer functional groups bind to the bacterial cell membrane (Figure 3). A total of four washings were completed to remove unbound fluorescein. Bacteria were imaged using a Zeiss Upright Epifluorescent microscope (Figure 3). SYTO-9 was used as a positive control due to its known fluorescence and bacteria without fluorescein was used as a negative control. Dipicolyl-Zn-fluorescein, ethylenediamine-fluorescein, and guanidine-fluorescein were tested. As expected, the dipicolyl-Zn-fluorescein showed a significant amount of fluorescence. This was expected, due to the binding of the dipicolyl-Zn<sup>2+</sup> complex with the pyrophosphate of Lipid II on the bacterial cell membrane.

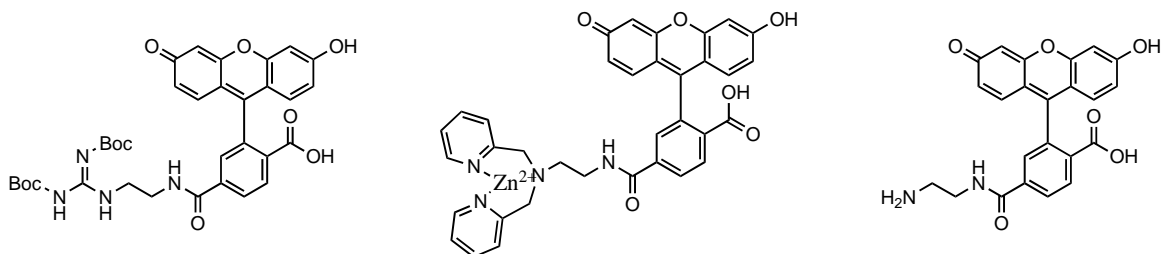


**Figure 3: (From left to right) Structure of guanidine-fluorescein, dipicolyl-Zn-fluorescein, and ethylenediamine-fluorescein.**

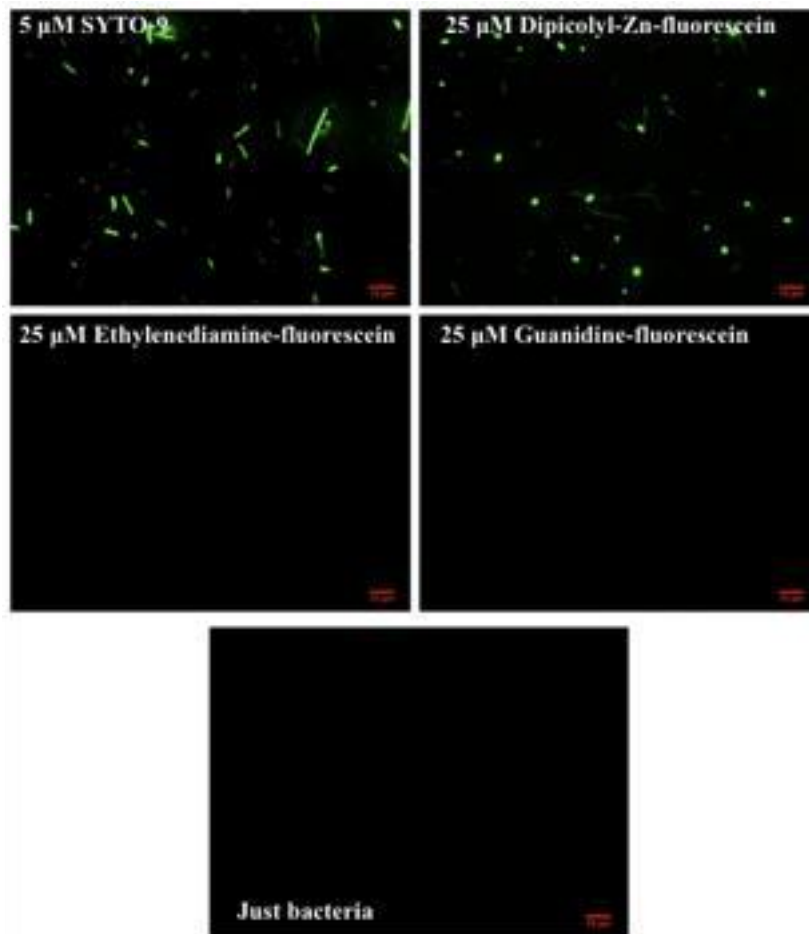


**Figure 4: Fluorescence imaging of monomers bound to bacterial cell membrane. SYTO-9 was used as positive control. Bacteria without fluorescein was used as negative control.**

Fluorous-allylamine was successfully synthesized, which is shown via NMR (Figure S1). The fluorous-allylamine synthesized was used for all of the first Thiol-ene reactions of the OligoTEAs.

The guanidine monomer was successfully synthesized (Figure 5). Both NMR (Figure S2) and LCMS (Figure S3) were used to verify the product. One large peak appeared on LCMS showing the mass, half-mass, and third-mass of the desired product. The first two reactions went to completion, however, excess allyl bromide in the third reaction caused formation of a side product which lowered the overall yield.

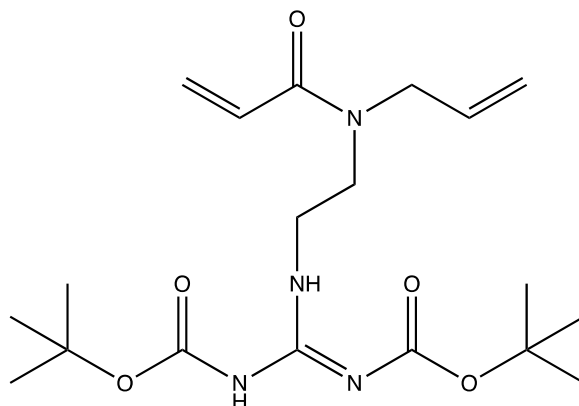


**Figure 5: The structure of guanidine monomer synthesized.**

AOTs with the amine and/or guanidine monomer were synthesized. The Michael addition reaction was monitored via DTDP assay (Figure S4). Both 3-mers and 4-mers were synthesized, including PDT-4Am, PDT-3Am, PDT-3G, and PDT-Am-2G (Figure 6). Final products were characterized with LC/MS (Figures S5-8). LC/MS of both PDT-4Am, PDT-3Am, and PDT-Am-2G showed the desired product mass and half-mass, while PDT-3G had the mass, half-mass, and third-mass. Due to small amounts, the mass of the product was determined via quantitative NMR (Figures S9-12). The integration of acetonitrile standard was used for comparison with the integration of a specific carbon on that AOT. Using these integrations, a ratio was calculated. This ratio was then used to find the mass of all four AOTs.

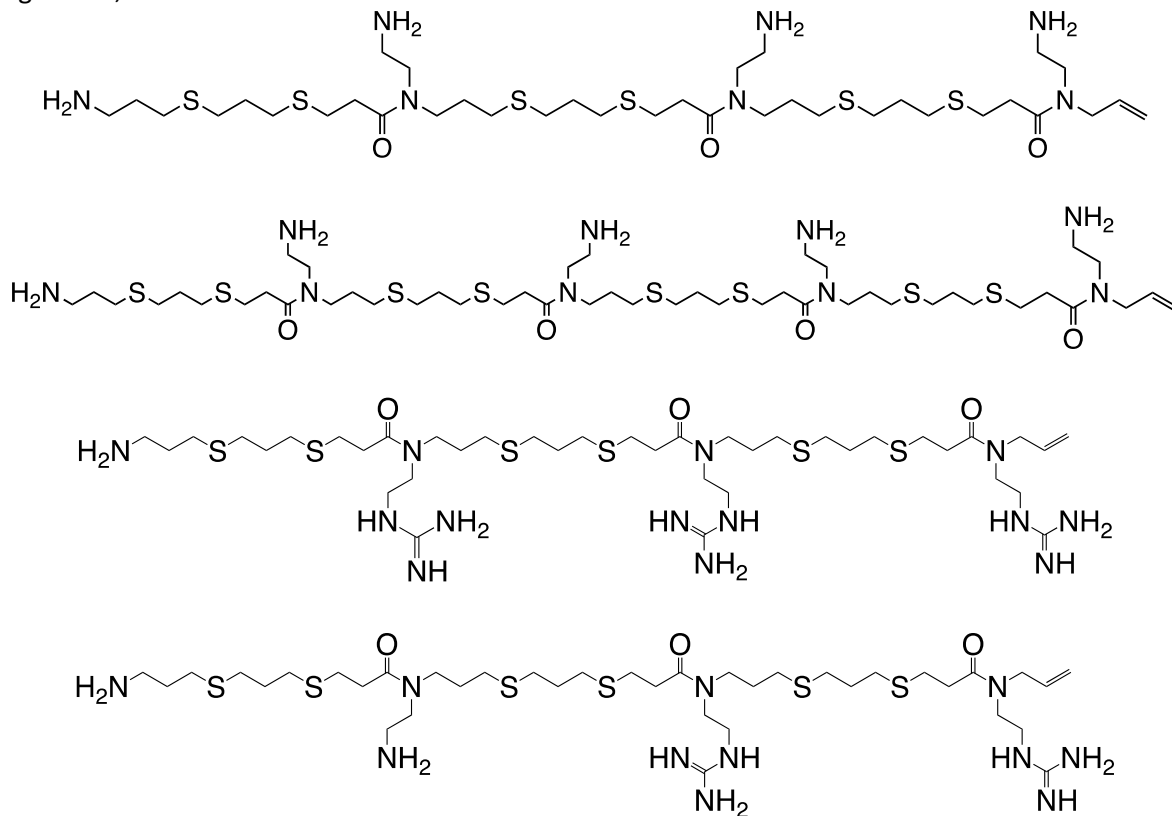


**Figure 6: Structures of AOTs synthesized. (From top to bottom) PDT-3Am, PDT-4Am, PDT-3G, PDT-Am-2G.**

The PDT-4Am AOT was then conjugated with dipicolyl groups in a separate reaction to obtain the desired product. PDT-4Am was successfully conjugated with the dipicolyl group (Figure 7). It was questionable whether all amine groups would become conjugated. However, LC/MS showed three distinct peaks (Figure S13). These peaks all obtained the half-mass and third-mass of the fully conjugated product. Mass corresponding to other partially complete conjugations did not appear, therefore showing that all five amine groups were conjugated to the dipicolyl groups. These conjugated compounds will form a complex with zinc due to the orientation of the three nitrogens in the dipicolyl monomer.

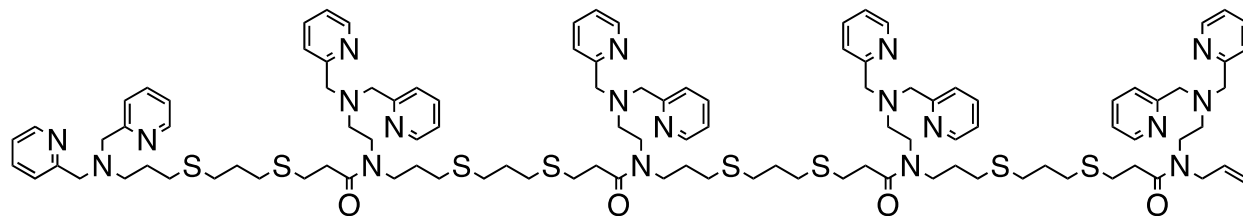


**Figure 7: Structure of PDT-4Am conjugated with dipicolyl groups.**

A MIC Assay was performed on the AOTs, PDT-4Am, PDT-3Am, PDT-3G, and PDT-Am-2G, as a reference for the conjugated AOTs (Figure S14). All four AOTs showed moderate antibacterial activity when compared to the control, vancomycin. PDT-4Am and PDT-3G showed lower MIC values than PDT-3Am and PDT-Am-2G (Figure 8).

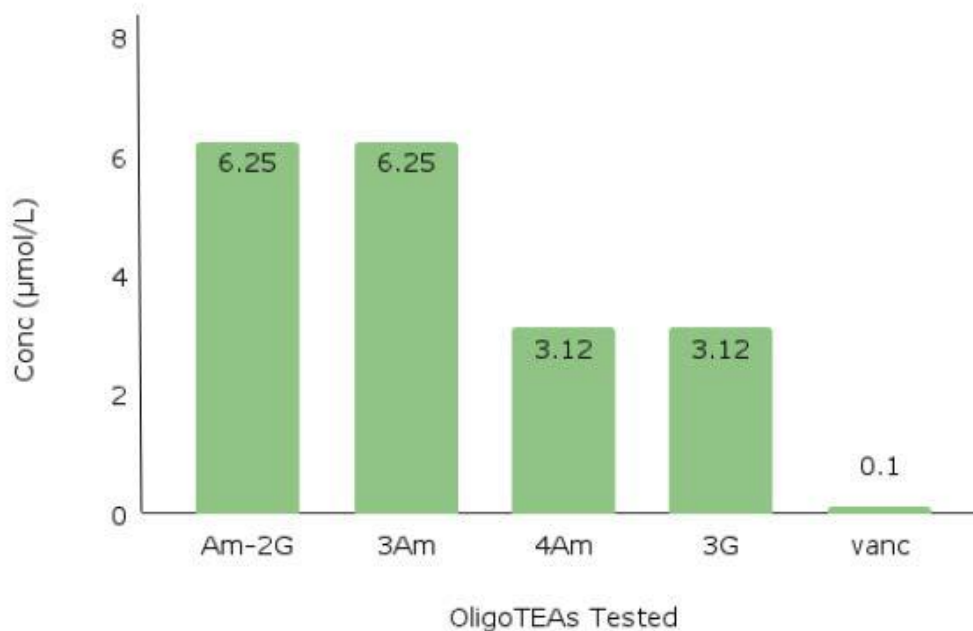


**Figure 8: MIC values for all four AOTs synthesized. Vancomycin was used as a control.**

#### IV. CONCLUSION/FUTURE RESEARCH

Overall, we successfully synthesized a range of AOTs. These AOTs have decent antibacterial activity, however, may also have significant cytotoxicity. We also found the dipicolyl-conjugation reaction with PDT-4Am was successful. Future research will involve testing the remaining AOTs with this conjugation reaction. These conjugates will then be tested with bacteria via MIC assay to determine antibacterial activity. The dipicolyl-conjugated AOTs will also be tested with mammalian cells for cytotoxicity in hopes that they are more selective and therefore, less toxic.

#### REFERENCES

1. National Antimicrobial Resistance Monitoring System for Enteric Bacteria (NARMS). (2016). Retrieved from <https://www.cdc.gov/narms/faq.html>
2. Rotem, S., & Mor, A. (2009). Antimicrobial peptide mimics for improved therapeutic properties.

*Biochimica et Biophysica Acta (BBA) - Biomembranes*, 1788(8), 1582–1592.  
<https://doi.org/10.1016/j.bbamem.2008.10.020>

3. Porel, M., Thornlow, D. N., Artim, C. M., & Alabi, C. A. (2017). Sequence-Defined Backbone Modifications Regulate Antibacterial Activity of OligoTEAs. *ACS Chemical Biology*, 12(3), 715–723. <https://doi.org/10.1021/acscchembio.6b00837>

4. Yarlagadda, V., Sarkar, P., Samaddar, S., & Haldar, J. (2016). A Vancomycin Derivative with a Pyrophosphate-Binding Group: A Strategy to Combat Vancomycin-Resistant Bacteria. *Angewandte Chemie (International Ed. in English)*, 55(27), 7836–7840. <https://doi.org/10.1002/anie.201601621>  
Supporting Information

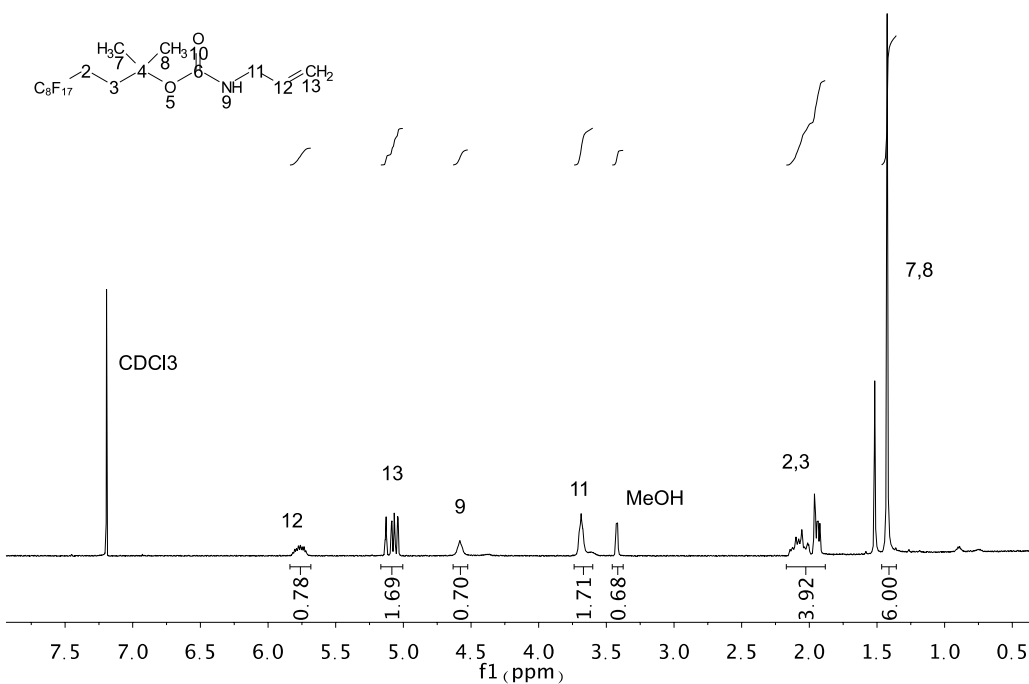


Figure 1: NMR of fluororous-allylamine

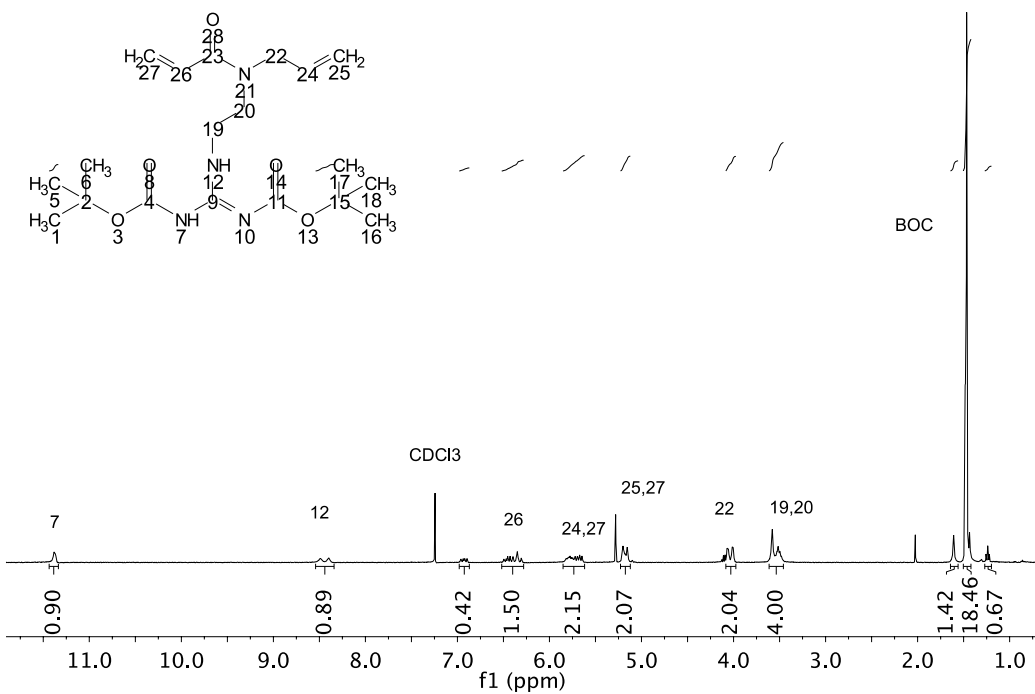


Figure 2: NMR of guanidine monomer

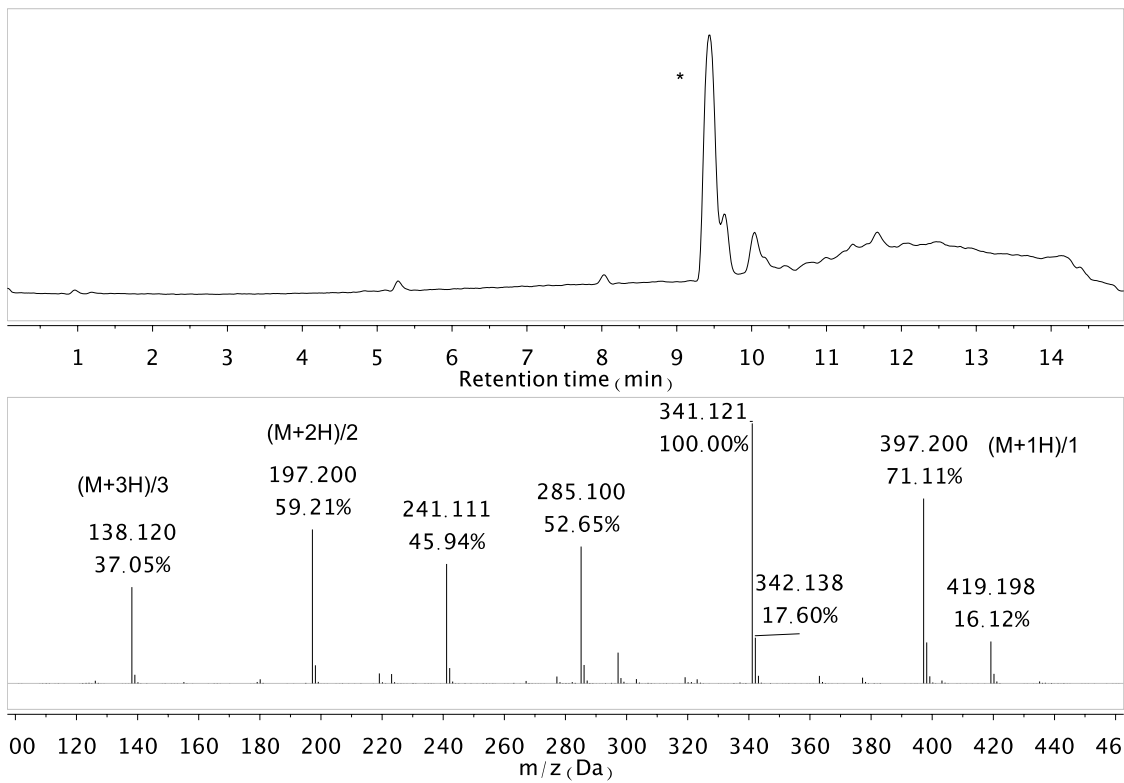


Figure 3: LC/MS of guanidine monomer. Mass, half-mass, and third-mass were identified.

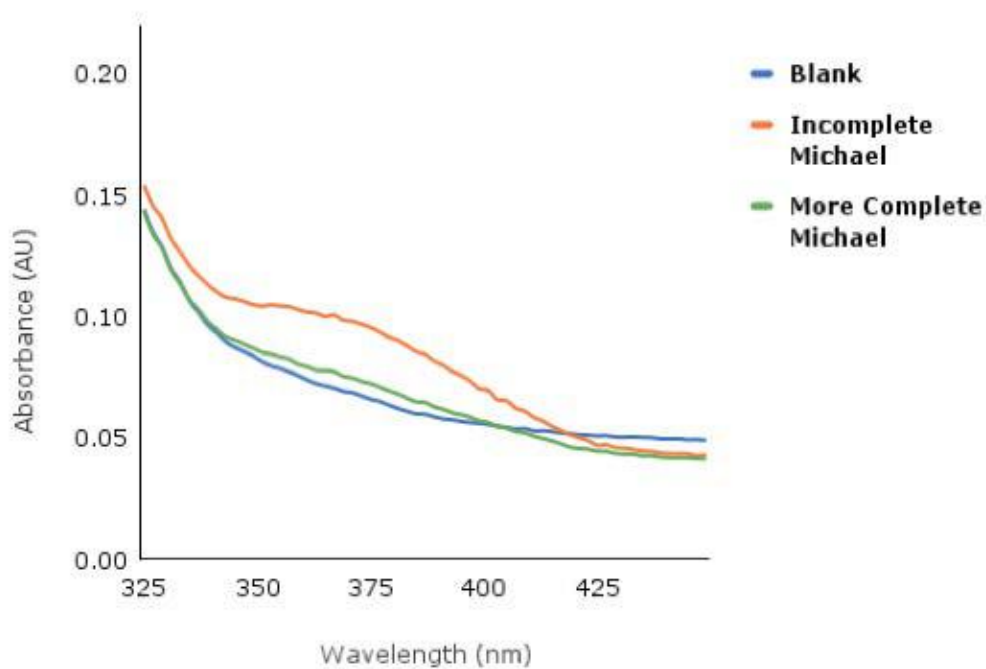


Figure 4: DTDP Assay of the Michael addition reaction. The orange line indicates the reaction is not complete, while the green line indicates it is more complete.

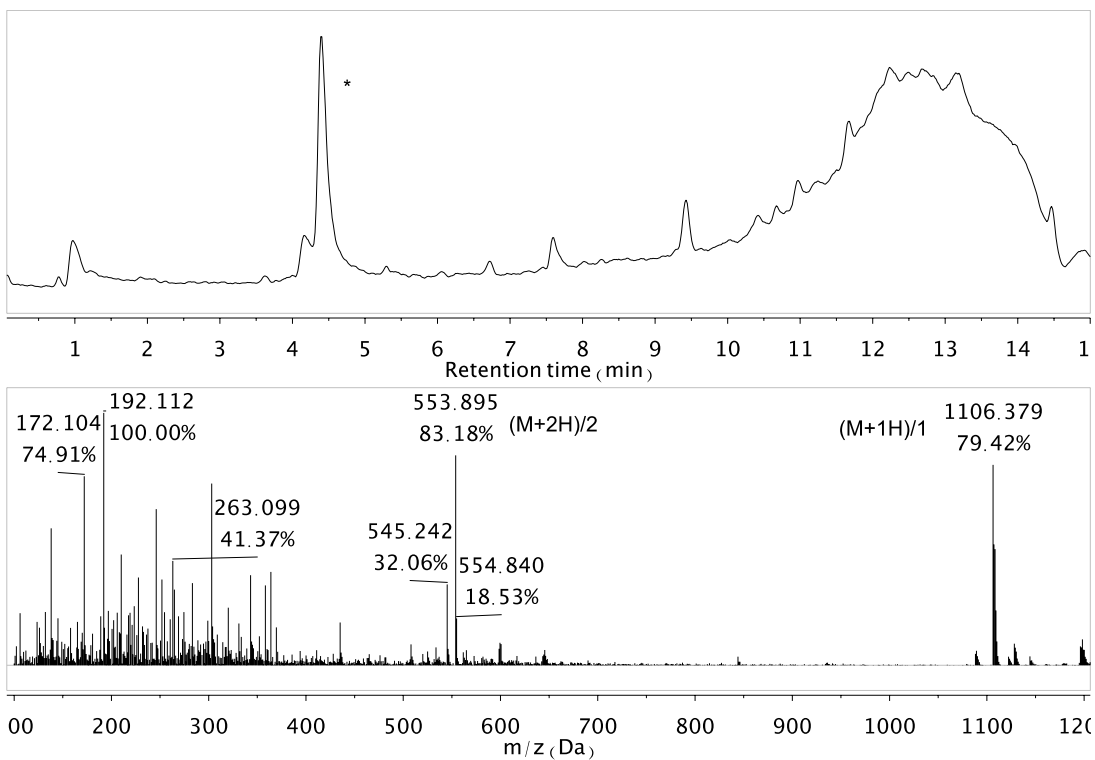


Figure 5: LC/MS of PDT-4Am. Mass and half-mass were identified.

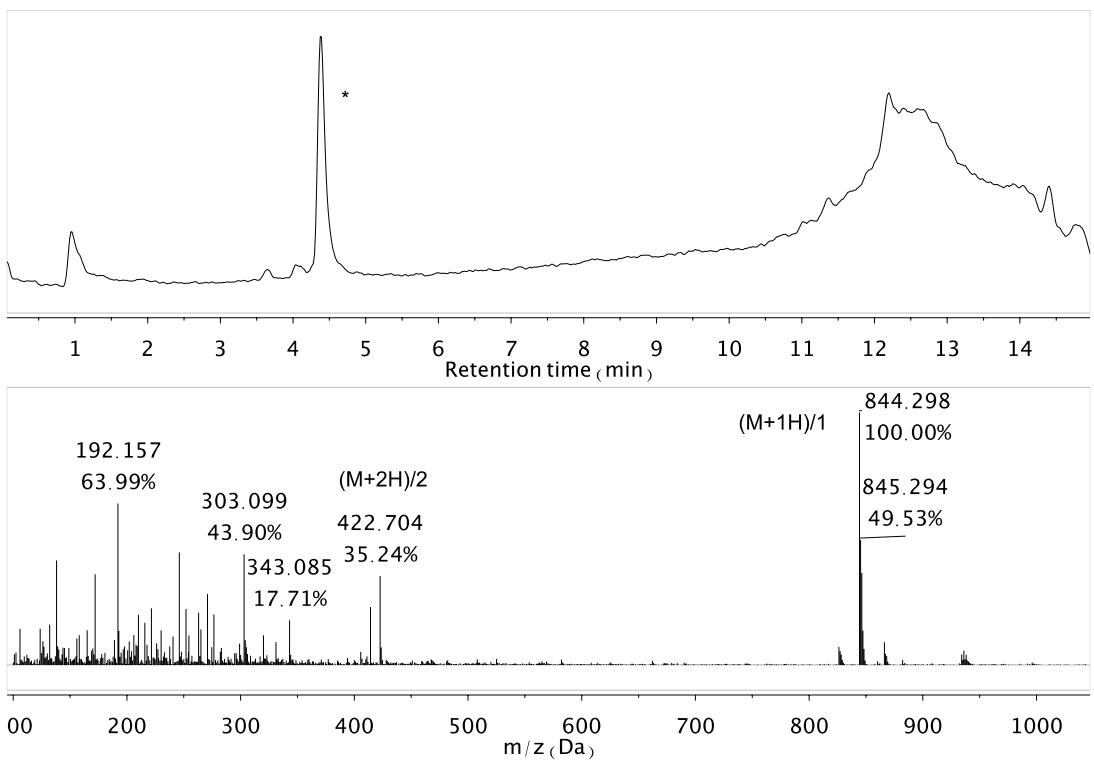


Figure 6: LC/MS of PDT-3Am. Mass and half-mass were identified.

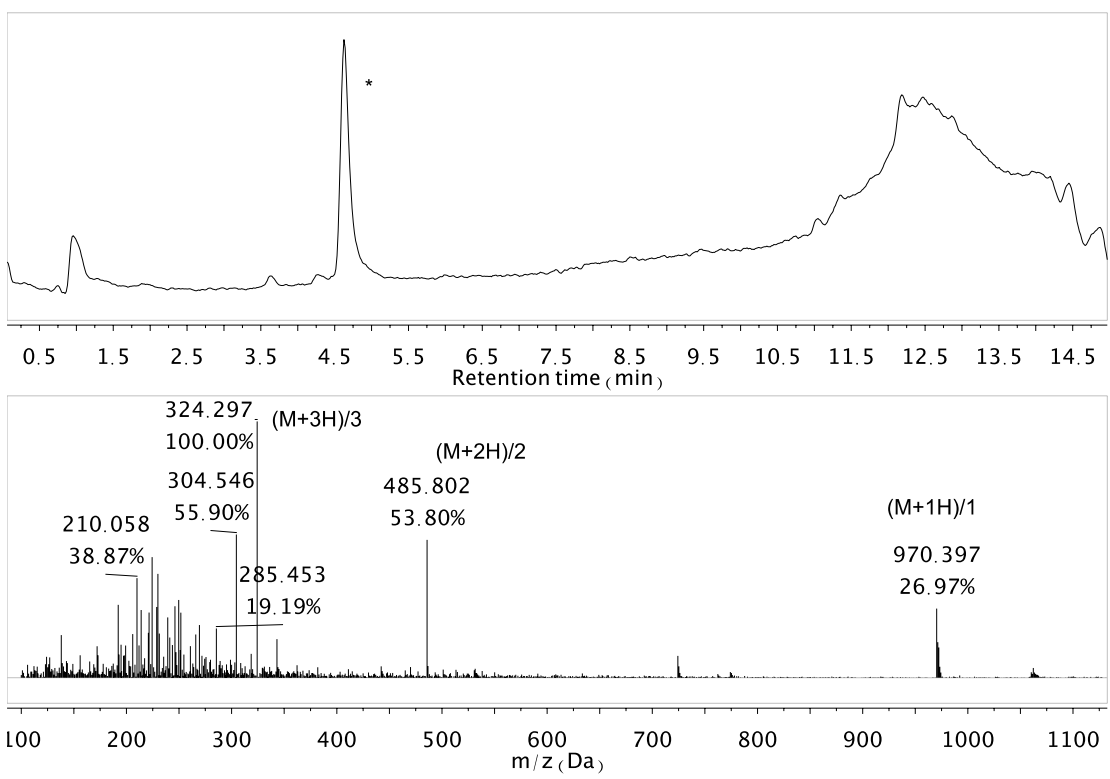


Figure 7: LC/MS of PDT-3G. Mass, half-mass, and third-mass were identified.

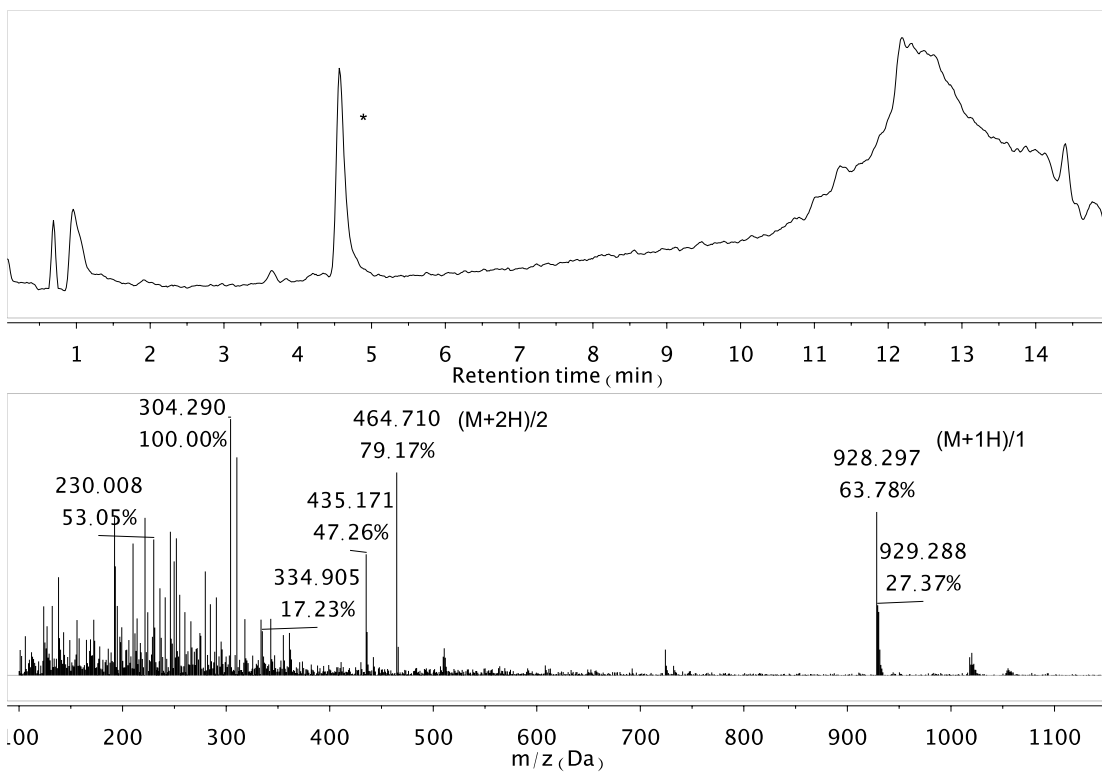


Figure 8: LC/MS of PDT-Am-2G. Mass and half-mass were identified.

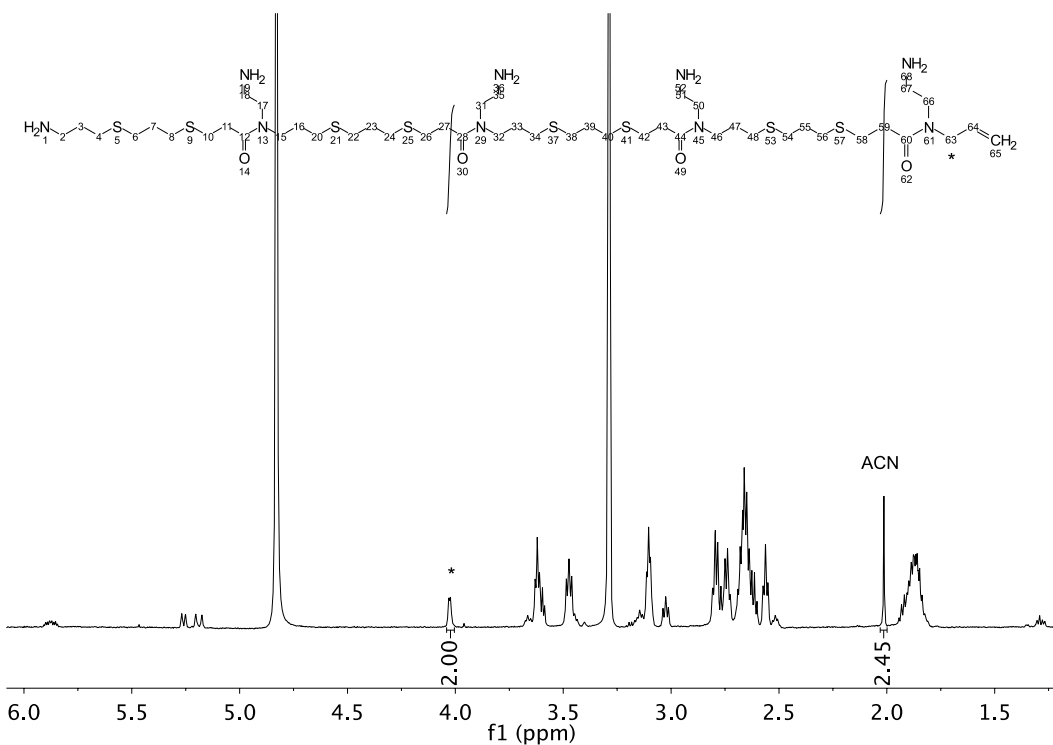


Figure 9: Quantitative NMR of PDT-4Am. Integration of acetonitrile standard was used for comparison with integration of carbon 63.

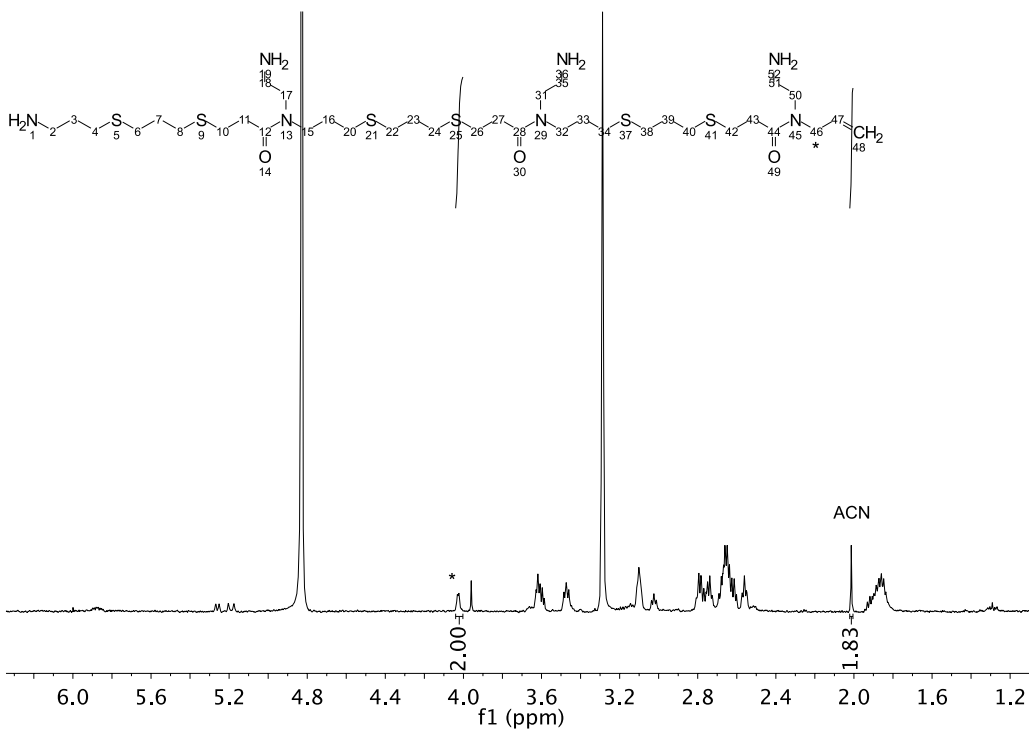


Figure 10: Quantitative NMR of PDT-3Am. Integration of acetonitrile standard was used for comparison with integration of carbon 46.

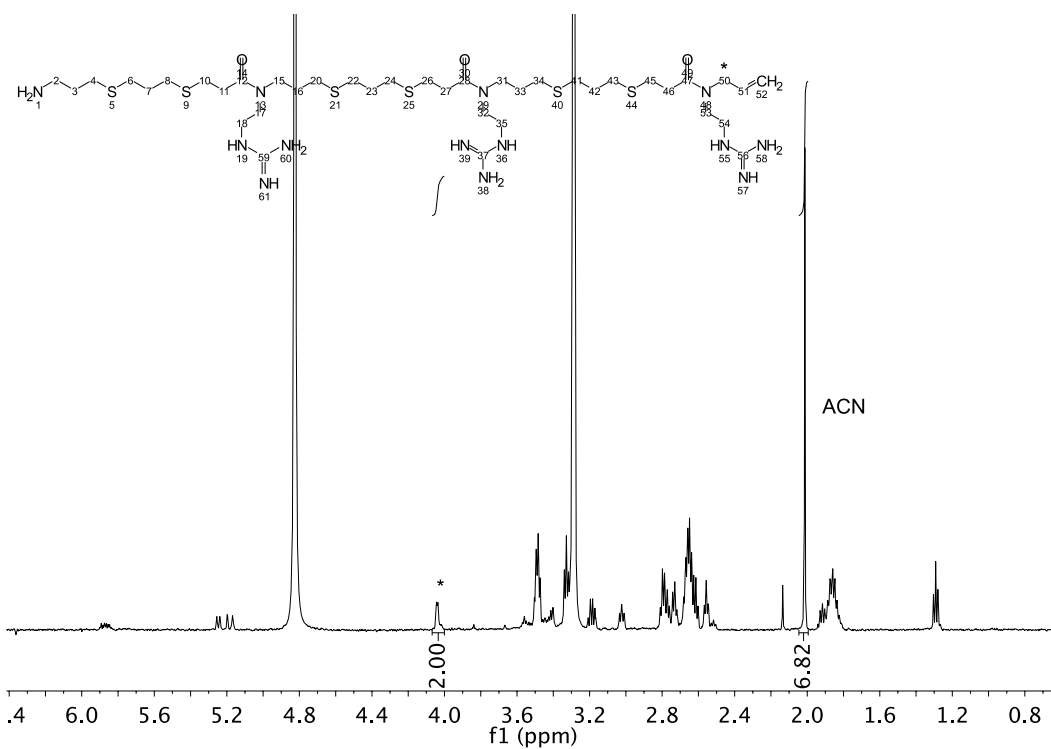


Figure 11: Quantitative NMR of PDT-3G. Integration of acetonitrile standard was used for comparison with integration of carbon 50.

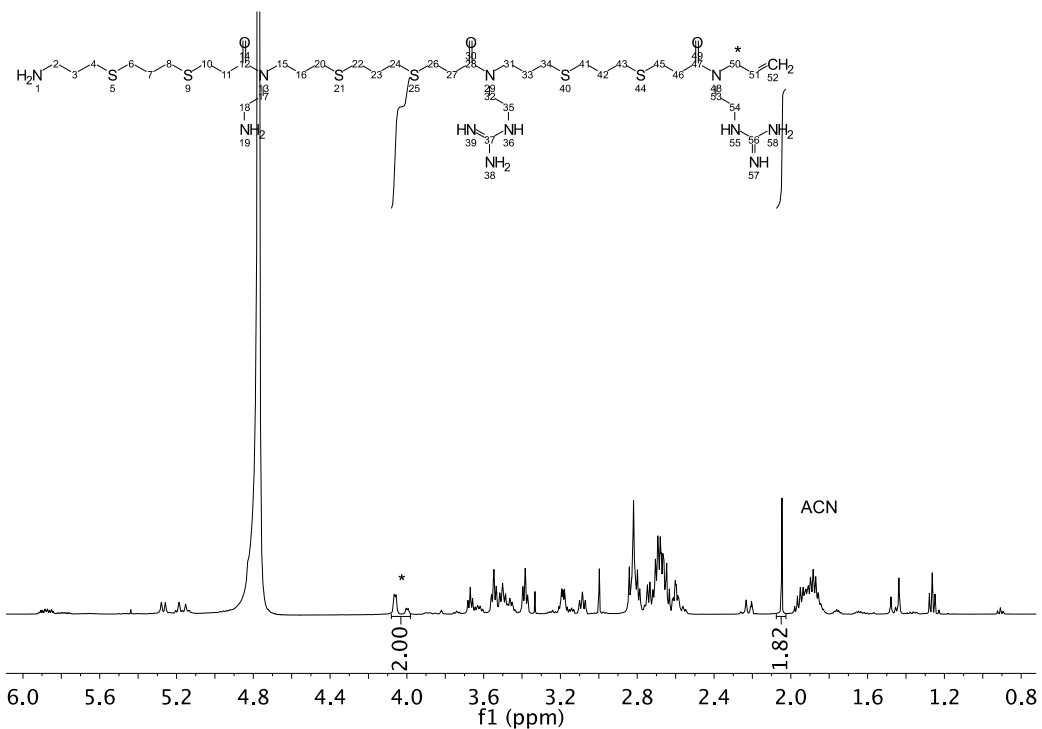


Figure 12: Quantitative NMR of PDT-Am-2G. Integration of acetonitrile standard was used for comparison with integration of carbon 50.

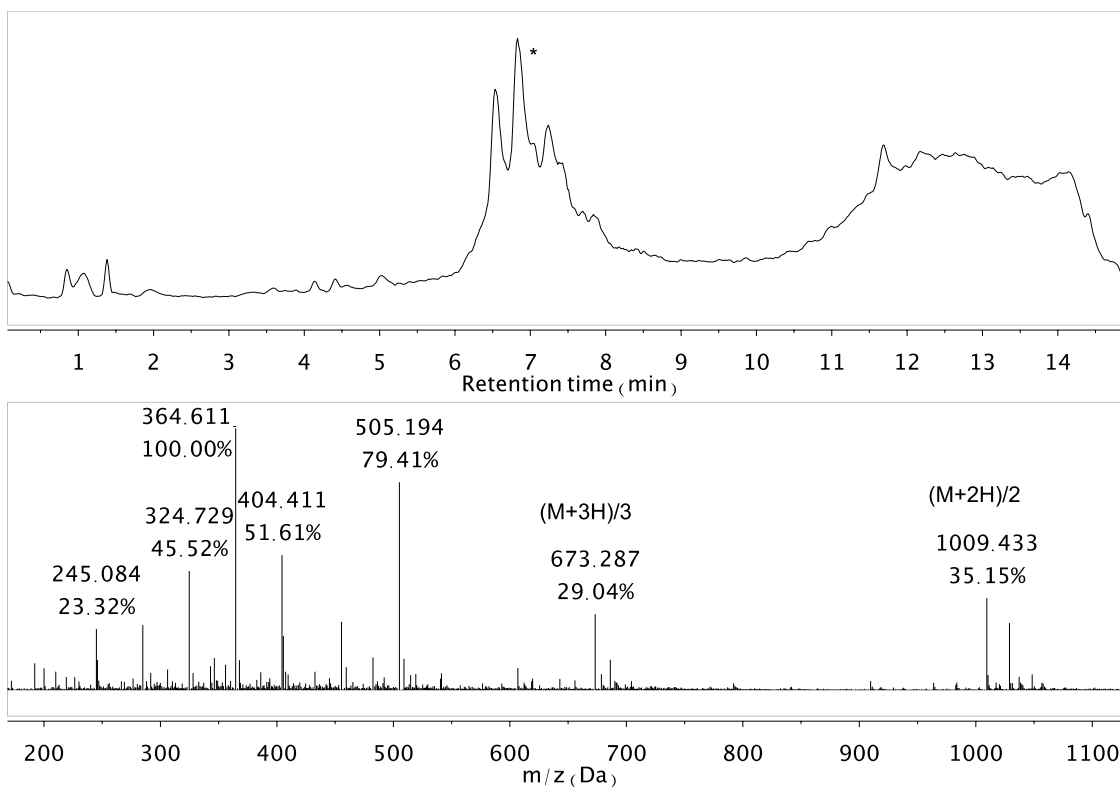


Figure 13: LC/MS of dipicolyl-conjugated PDT-4Am. Three distinct peaks were seen. Each peak contained the half-mass and third-mass.

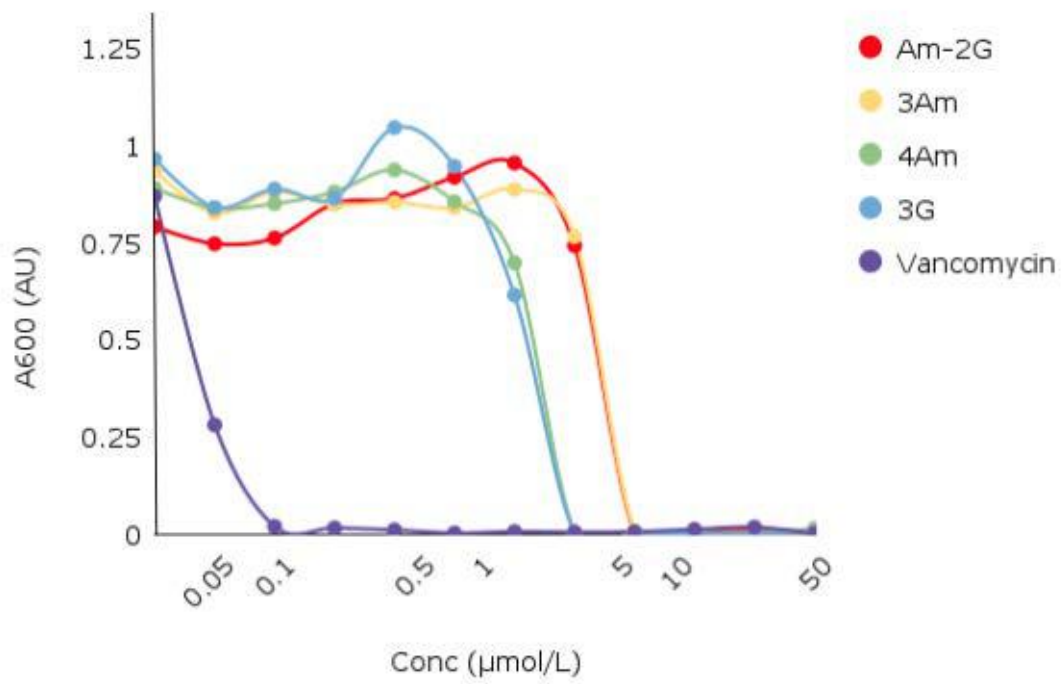


Figure 14: MIC Assay of all four AOTs. Vancomycin was used as a control.